Axion Miniclusters: Formation, Structure and Observational Signatures

Dissertation

for the award of the degree

"Doctor rerum naturalium"
of the Georg-August-Universität Göttingen

within the doctoral program Physik
of the Georg-August University School of Science (GAUSS)

submitted by

David Ellis

from Bedford, UK.
Göttingen (2021)

Thesis Committee

Prof. David Marsh, Department of Physics, King's College London

Prof. Jens Niemeyer, Institut für Astrophysik, Universität Göttingen

Prof. Laura Covi, Institut für Theoretische Physik, Universität Göttingen

Members of the Examination Board

Reviewer: Prof. David Marsh, Department of Physics, King's College London

Second Reviewer: Prof. Jens Niemeyer, Institut für Astrophysik, Universität Göttingen

Further members of the Examination Board:

Prof. Laura Covi, Institut für Theoretische Physik, Universität Göttingen

Prof. Steffen Schumann, Institut für Theoretische Physik, Universität Göttingen

Prof. Stan Lai, Physikalisches Institut, Universität Göttingen

Prof. Ansgar Reiners, Institut für Astrophysik, Universität Göttingen

Oral examination date: 13/12/2021

CONTENTS

ACKNOWLEDGEMENTS

Every single member of the Göttingen cosmology group has contributed to making my three years here great. The joy of working at Göttingen was, of course, particularly defined by those I had the privilege to share an office with.

I want to thank my supervisor, Doddy Marsh, who gave me the opportunity to move to Germany to work with him on this PhD. Throughout this PhD, Doddy has patiently guided me and always encouraged me to pursue avenues that I found most interesting.

I have also received invaluable guidance from many other people within the department. In particular, I also want to thank Benedikt Eggemeier whose work has often been the foundation of my own and who has always been my first point of call for many of my problems. I also want to mention Viraf Mehta whose essential guidance was rarely limited to just the realms of academia.

I also want to thank Viraf and Benedikt again as well as Mona Dentler for reading this thesis and giving me incredibly useful feedback.

Finally, as always, I am indebted to all of my friends and family that supported my journey to this point.

I. INTRODUCTION

The beginning of the history of dark matter (DM) is often attributed to Fritz Zwicky who, in 1933, noticed that the velocities of galaxies contained within the Coma cluster were inconsistent with the amount of visible matter [1, 2]. Zwicky estimated the total mass by carefully measuring the luminosity of the stars within the cluster. However, he noticed that the gravitational force exerted on the member galaxies by this matter alone was around 400 times smaller than the force required to hold the members of the Coma cluster together. He, therefore, inferred the existence of additional matter which he called "dunkle Materie" (dark matter). However, the history of dark matter predates this work by around 50 years.

As early as 1889, Lord Kelvin used the velocity dispersion of stars within the Milky Way (MW) to discover that "many of our stars, perhaps a great majority of them, may be dark bodies" [3]. The term "dark matter" was also used as early as 1906 by Henri Poincare when referring to Lord Kelvin's missing matter [4].

Later, in 1922, Jacobus Kapteyn measured the velocities of stars orbiting the MW and noted similarly that their speeds were too great to be held bound to the galaxy by the gravitational force of the visible matter alone [5]. This was also later found, more famously, by fellow Dutchman Jan Oort who instead measured the velocities of stars orbiting neighbouring galaxies [6].

Since then, the evidence supporting the existence of dark matter has only increased. Improved measurements of star velocities, as well as new methods for measuring the mass of otherwise invisible hydrogen gas, strengthened existing evidence [7–10]. However, new forms of evidence were also found.

Due to Einstein's theory of relativity, the path of light is bent in the presence of a gravitational field [11]. This can result in images of galaxies being distorted by the gravitational field of, foreground objects with large masses. This gives astronomers a way to determine the true mass of an object, even if most of its mass is invisible [12].

Perhaps the most rigorous evidence, however, comes from the cosmic microwave background (CMB) radiation. The CMB is an electromagnetic radiation relic from the early universe. When it was first discovered accidentally in 1965, it was found to be highly isotropic with a temperature of $\sim 3.5°$K [13, 14]. However, more recent experiments such as successive space telescopes COBE, WMAP and Planck have since measured small anisotropies in

this background radiation [15–17]. The scale of these anisotropies can be explained using the ΛCDM model. In this model, as well as ordinary (baryonic) matter, the universe is also composed of cold dark matter (CDM) and dark energy (denoted Λ). By fitting this model to the measured CMB anisotropies, we find that the universe is made of only around 5% ordinary matter. The rest is made up of 27% dark matter and 68% dark energy [17].

However, despite the overwhelming amount of evidence supporting the existence of DM, we are yet to detect it directly and therefore know remarkably little about it. We know that it must interact incredibly weakly with ordinary matter. For example, its cross-section with photons must be extremely small to explain why we haven't detected any radiation from DM yet [18–21]. Additionally, it must be stable on time scales of order the age of the universe since we know it must have already existed at $z \gtrsim 10^5$, much earlier than the production of the CMB [22, 23]. Furthermore must also continue to exist today in order to hold galaxies together given the high orbital velocities of their outer-stars discussed previously [3, 5, 6]. We also know from observations of small-scale structure formation as well as measurements of the anisotropies of the CMB that DM must also be pressureless, that is, it must have negligible self-interactions [24, 25]. Lastly, since most of the matter content of the Universe is composed of DM, it must also be cold. This means that the velocities of DM particles must be relatively small to allow for the observed structure formation. If DM was much hotter, objects such as galaxies would not have been able to form [26, 27].

To date, we have been unable to detect dark matter directly, however, we have some good ideas as to what it might look like [28]. Currently, three of these candidates stand out as being the most popular. These are, weakly interacting massive particles (WIMPs), primordial black holes (PBHs) and axions (See Refs [29], [30] and [31] respectively for reviews).

WIMPs are probably the most extensively researched of these candidates. They are a class of heavy particles with masses of the order the mass of the proton ($\mathcal{O}$(GeV)). Other than gravity, WIMPs have interaction strengths equal or weaker than that of the weak force. These particles are typically thought of as being produced thermally in the early universe through a process known as freeze-out. One popular WIMP candidate known as the neutralino is predicted by supersymmetry (SUSY) and, as the name suggests, is phenomenologically similar to neutrinos [32]. Since neutrinos are fermions, they are ruled out as a DM candidate since their masses are too small to be consistent with observed

galaxy formation[1]. However, the neutralino has a much larger mass making it a prime DM candidate [34].

The WIMP-proton cross-section is constrained primarily through direct detection experiments. The most sensitive of these, such as DEAP-3600 and Xenon1T are noble gas scintillators [35]. Additional constraints on the WIMP arise from measurements of the matter power spectrum and searches for gamma-rays produced by WIMP-WIMP annihilation [33, 36]. The remaining untested WIMP parameter space is rapidly shrinking. Additionally, in spite of the hopes of many, no evidence of WIMPs has been seen in the data from the Large Hadron Collider (LHC) [37].

Primordial black holes, as the name suggests, are black holes formed in the early universe. Unlike WIMPs and axions, PBHs do not require the existence of particles outside of the SM. Yakov Zel'dovich and Igor Novikov were the first to propose that black holes might form overdensities in the very early universe [38]. Later, their formation was studied further by Stephen Hawking [39]. However, recently there has been renewed interest in studying black holes as a DM candidate since the Laser Interferometer Gravitational-Wave Observatory (LIGO) have measured more black hole mergers than were previously expected [40].

Black holes emit Hawking radiation with a temperature that is inversely proportional to their mass. This means that very light black holes quickly evaporate [41]. This provides a lower limit on the mass a PBH can have. Additional constraints on the fraction of DM in the form of PBHs come from gravitational microlensing. Microlensing is essentially the same as ordinary gravitational lensing. However, the strength of this lensing is so small that both images of the source light are measured on the same pixel [42]. Therefore, microlensing events are seen as brief amplifications in the source light. Significant ranges of the possible PBH mass range has been ruled out by microlensing surveys [43, 44].

Another DM candidate which has been receiving increasing levels of interest, and the subject of this work, is the axion. The axion is a theoretical elementary particle that was first suggested by Roberto Peccei and Helen Quinn as a way of solving the strong charge-parity (CP) problem of quantum chromodynamics (QCD) [45].

It was later realised that the axion would be produced in large quantities in the early universe. Since it is stable and only interacts very weakly with standard model (SM) matter, it is, therefore, a prime dark matter (DM) candidate [46–48]. If f_a is restricted to be below

[1] This is known as the Tremaine-Gunn bound [33].

the Planck scale, the allowed range of masses is 10^{-11} eV $\lesssim m_a \lesssim 10^{-2}$ eV, where the lower bound arises due to black hole superradiance [49, 50] and the upper bound from the SN1987A neutrino burst [51, 52].

The axion possesses a $U(1)$ global symmetry. This symmetry is broken when the temperature of the universe falls below the axion decay constant f_a. At this time, the axion field takes on a random misalignment angle between zero and 2π on scales of order the size of the Hubble radius. The precise distribution of the axionic DM today depends critically on at which point during the cosmic history this symmetry is broken. We can define two distinct scenarios.

If PQ symmetry breaking occurs before or during inflation and is not restored again afterwards, regions of space containing a single value of the axion field get inflated. Therefore, within an area the size of the observable universe, the axion field will have a single uniform value. Axions are produced via the misalignment mechanism as this value oscillates and decays to zero. In this scenario, we can straightforwardly calculate the relic abundance as a function of m_a, f_a and the initial random field value θ_i.

This work, however, focuses on the second scenario. Here, the PQ symmetry breaking occurs after inflation. As a result, the current observable region would have initially contained many patches with different misalignment angles. This is important as topological defects such as cosmic strings and domain walls will form in regions where the field undergoes a complete circuit in field space. As in the other scenario, axions are produced via the misalignment mechanism. However, additional axions are produced via the decay of these topological defects. Due to this added complexity, there is no definite consensus on the value of m_a required to give the correct relic abundance. However, it is often assumed that a mass greater than around $20\,\mu$eV is required in order not to overproduce DM, with larger values preferred in the case with long-lived domain walls [53–63].

The decay of the defects also predicts large-amplitude, small scale density perturbations known as axion minicluster seeds[2]. These overdensities collapse very early and later merge to form gravitationally bound axion miniclusters which are expected to exist today as small dense objects [65–67].

If a significant fraction of the DM is bound in these miniclusters, it would significantly reduce the sensitivity of direct detection experiments attempting to detect the relic density

[2] In some scenarios, it is also possible that these overdensities instead collapse into black holes [64]

produced by the misalignment mechanism [68–73]. It has been estimated that impacts between miniclusters and the Earth could be rare as once every 10^5 years. However, tidal stripping of miniclusters in the Milky Way due to close encounters with stars could produce a diffuse background and hence the possibility to detect tidal streams [74–77].

However, all is not lost. For example, since miniclusters are small dense objects, it may be possible to detect them using gravitational microlensing just as is being attempted with PBHs [66, 78, 79]. It may also be possible to search for miniclusters using a similar process called gravitational femtolensing [80]. Additionally, if an axion minicluster collided with a neutron star, axions would be resonantly converted into radio waves due to the neutron star's strong magnetic field. We therefore might also be able to find miniclusters using radio astronomy [81, 82].

In order to estimate the signals we should expect to see using these methods, it is essential that we are able to accurately predict the mass function, dn/dM, and size distribution of miniclusters. One way of doing this is using the Press-Schechter (PS) model, a semi-analytic formalism to which predicts the halo mass function from the initial power-spectrum assuming Gaussianity. Another approach is the Peak-Patch (PP) algorithm. PP is based on an extended PS model that solves the excursion set in real space on a true realisation of the density field thus accounting for all non-Gaussianity [83–86].

Applying the PP algorithm to axion density fields computed from field theory solutions of topological defect decay [55], it is possible to accurately reproduce the results of recent high-resolution N-body simulations [87] at a fraction of the numerical cost [88]. Additionally, these N-body simulations have shown that axion miniclusters form Navarro-Frenk-White (NFW) profiles [89]. Using PP it is possible to build merger histories for each dark matter halo in the data set and hence estimate the full statistical spread of the halo concentrations. This extends and clarifies the successes of purely analytical models and enables us to make the most rigorous predictions of the ability of axion miniclusters to produce microlensing signals to date [79, 88, 90].

Furthermore, PP can be used as a tool for tracking objects in the N-Body data which are first to collapse. Some of these objects will become substructures within larger axion miniclusters. This substructure may have a significant contribution to the axion miniclusters ability to produce microlensing signals [91].

This thesis is structured as follows. Secs I to VI introduce the relevant background and

theory to this work and Secs VII & VIII present the results from Refs. [88] and [91]. I start, in Sec. II, by outlining the key pieces of evidence supporting the existence of DM. Then, in Sec. III I give an overview of the three most popular DM candidates including their formation mechanisms and primary constraints with a focus on axions. Then, in Sec. IV, I explore some important models for gravitational collapse. This includes purely theoretical models such as spherical collapse and linear perturbation theory, semi-analytical formalisms such as Press-Schechter and the Peak-Patch algorithm as well as the fundamentals of the purely numerical N-body simulations. After this, in Sec. V I introduce possible models for the density profiles of axion miniclusters and their theoretical motivation. I then outline, briefly, some of the key relations for axion stars and their predicted density profiles. In particular, I also outline how the concentration of NFW halos can be predicted from their collapse redshifts. In Sec. VI, I give an introduction to gravitational microlensing including the important considerations of extended lenses and wave effects. In Sec. VII, I present the results from Ref. [88]. This includes the reproduction of existing N-Body results using PP and its use to estimate the concentrations of axion miniclusters. After this, in Sec. VIII, I demonstrate how PP can be used to help identify early collapsing, and hence particularly interesting, objects in axion N-body simulation data. I also attempt to draw connections between the halo properties found using PP and the final density profiles of these objects. Finally, I conclude by summarising these results and try to provide a vision of what the future prospects of this field of research might be in Sec. IX.

In a number of places throughout this thesis, I have reused sections that I have written in Refs. [88] and [91]. I have made it clear where the text comes directly from these works. I played the leading role for both of these papers, performing the majority of the analysis, code development and graph production. However, it should be noted that a number of other people have contributed to these works beyond the useful discussion mentioned previously. Naturally, my primary supervisor, David Marsh, has contributed to both works by helping to define the scope and direction of these projects as well as editing both of these publications. Christoph Behrens developed the Peak Patch code which played a key role to both of these papers. Benedikt Eggemeier produced the N-body simulation data which was compared to in Ref. [88] and used directly in Ref. [91]. Christoph Behrens, Benedikt Eggemeier and Javier Redondo have all also contributed appendices for Ref.[91].

II. EVIDENCE FOR DARK MATTER

A. Virial Theorem

Consider a large number of particles with a phase-space distribution function $f(\mathbf{x}, \mathbf{v}, t)$ under the influence of a smooth potential $\Phi(\mathbf{x}, t)$. The density at each point in space is given by integrating over velocity

$$\rho(\mathbf{x}, t) = m \int f(\mathbf{x}, \mathbf{v}, t) \mathrm{d}^3\mathbf{v}, \tag{1}$$

where m is the particle mass.

If the particles are collisionless and cannot be created or destroyed, then the evolution of the phase-space must conserve mass. Therefore, we can describe the system using the collisionless Boltzmann equation

$$\frac{\mathrm{d}f}{\mathrm{d}t} = \frac{\partial f}{\partial t} + \sum_i v_i \frac{\partial f}{\partial x_i} - \sum_i \frac{\partial \Phi}{\partial x_i} \frac{\partial f}{\partial v_i}, \tag{2}$$

where subscripts $i =\in (1, 2, 3)$ denote the three spacial coordinates.

The average value of a quantity Q at position $\mathbf{x}$ is given by

$$\langle Q \rangle (\mathbf{x}, t) \equiv \frac{1}{n(\mathbf{x}, t)} \int Q f \mathrm{d}^3\mathbf{v}, \tag{3}$$

where $n(\mathbf{x}, t)$ is the number density given by

$$n(\mathbf{x}, t) \equiv \int f \mathrm{d}^3 v \equiv \frac{\rho(\mathbf{x}, t)}{m}, \tag{4}$$

and $\rho(\mathbf{x}, t)$ is the local density. For a stationary distribution, $\mathrm{d}f/\mathrm{d}t = 0$. Therefore, multiplying Eq. 2 by Q and integrating over velocity we obtain

$$\frac{\partial}{\partial t} \left[n \langle Q \rangle \right] + \sum_i \frac{\partial}{\partial x_i} \left[n \langle Q v_i \rangle \right] + n \sum_i \frac{\partial \Phi}{\partial x_i} \left\langle \frac{\partial Q}{\partial v_i} \right\rangle = 0. \tag{5}$$

We obtain the continuity equation by setting $Q = 1$ to give

$$\frac{\partial n}{\partial t} + \sum_i \frac{\partial}{\partial x_i} \left[n \langle v_i \rangle \right] = 0. \tag{6}$$

However, if instead, we set $Q = v_j$, we obtain momentum equations for each of the three physical dimensions

$$\frac{\partial}{\partial t} \left[n \langle v_j \rangle \right] + \sum_i \frac{\partial}{\partial x_i} \left[n \langle v_j v_i \rangle \right] + n \frac{\partial \Phi}{\partial x_i} = 0. \tag{7}$$

Multiplying this by mx_k, integrating and rearranging slightly we get

$$\int x_k \frac{\partial \rho \langle v_i \rangle}{\partial t} \mathrm{d}^3\mathbf{x} = -\sum_i \int x_k \frac{\partial [\rho \langle v_i v_j \rangle]}{\partial x_i} \mathrm{d}^3\mathbf{x} - \int \rho x_k \frac{\partial \Phi}{\partial x_j} \mathrm{d}^3\mathbf{x}. \tag{8}$$

Using the theorem of divergence, we can rewrite the first term on the right-hand side as

$$-\sum_i \int x_k \frac{\partial [\rho \langle v_i v_j \rangle]}{\partial x_i} \mathrm{d}^3\mathbf{x} = 2K_{kj} + \Sigma_{kj}, \tag{9}$$

where the K_{jk} is the kinetic energy tensor given by

$$K_{jk} = \frac{1}{2} \int \rho \langle v_j v_k \rangle \mathrm{d}^3\mathbf{x}, \tag{10}$$

and Σ_{jk} is the surface energy tensor given by

$$\Sigma_{jk} = \sum_i \int x_k \rho \langle v_j v_k \rangle \mathrm{d}^3\mathbf{x}. \tag{11}$$

The last term is equal to the Chandrasekhar potential energy tensor W_{jk}. We can therefore write Eq. 8 simply as

$$\int x_k \frac{\partial \rho \langle v_i \rangle}{\partial t} \mathrm{d}^3\mathbf{x} = 2K_{jk} + W_{jk} + \Sigma_{jk}. \tag{12}$$

The kinetic energy tensor can be written as

$$K_{jk} = T_{jk} + \frac{\Pi_{jk}}{2}, \tag{13}$$

where T_{jk} and $\Pi_{jk}/2$ are the contributions from coherent streaming and random motion respectively.

Since the spacial part has already been integrated out, we can pull the partial derivative in Eq. 12 outside the integral and turn it into a full derivative. Additionally, since the tensors T_{jk}, W_{jk} and Σ_{jk} are diagonally symmetric, we can write Eq. 12 as

$$\frac{1}{2} \frac{\mathrm{d}}{\mathrm{d}t} \int \rho \left[x_k \langle v_j \rangle + x_j \langle v_k \rangle \right] = 2T_{jk} + \Pi_{jk} + W_{jk} + \Sigma_{jk}. \tag{14}$$

The momentum inertia tensor is given by

$$I_{jk} = \int \rho x_j x_k \mathrm{d}^3\mathbf{x}, \tag{15}$$

and its time derivative is given by

$$\frac{\mathrm{d}I_{jk}}{\mathrm{d}t} = \int \frac{\partial \rho}{\partial t} x_j x_k \mathrm{d}^3\mathbf{x}, \tag{16}$$

$$= \int \frac{\partial(\rho\langle v_i\rangle)}{\partial x_i} x_j x_k \mathrm{d}^3\mathbf{x}, \tag{17}$$

$$= \int \rho \left[x_k\langle v_j\rangle + x_j\langle v_k\rangle\right], \tag{18}$$

where we have made use of the continuity equation. We see that this is equal to the left-hand side of Eq. 14. Therefore, we can write down the *tensor virial theorem* as

$$\frac{1}{2}\frac{\mathrm{d}^2 I_{jk}}{\mathrm{d}t^2} = 2T_{jk} + \Pi_{jk} + W_{jk} + \Sigma_{jk}. \tag{19}$$

Taking the trace of both sides and using the fact that Π_{jk} is trace-less gives us the *scalar virial theorem*

$$\frac{1}{2}\frac{\mathrm{d}^2 I}{\mathrm{d}t^2} = 2K + W + \Sigma. \tag{20}$$

Here, I is the moment of inertia, K is the kinetic energy, W is the potential energy and Σ is the work done on the system by external pressure.

For a static system ($\mathrm{d}^2 I/\mathrm{d}t^2 = 0$) with no external pressure ($\Sigma = 0$), we can finally write down that

$$W - 2K = 0. \tag{21}$$

This is what is often simply referred to as *the virial theorem* [92].

1. The Coma cluster

One of the most famous early pieces of evidence of the existence of DM came from Fritz Zwicky's 1933 observation of the Coma galaxy cluster. The Coma cluster is a collection of around 800 galaxies that are bound together in a region approximately 10^6 light-years across. By measuring the light from these galaxies, their mass can be estimated to be around $10^{12} M_\odot$ [1, 2].

The average potential energy within a radius R from the centre of an object with an internal mass profile $M(r)$ is given by

$$W = -\int_0^R \frac{GM(r)}{r} \mathrm{d}m. \tag{22}$$

For simplicity, we will assume that the mass within the cluster is uniformly distributed. The mass profile is therefore given by

$$M(r) = \frac{4}{3}\pi r^3 \rho \Rightarrow \mathrm{d}m = 4\pi r^2 \rho \mathrm{d}r\,, \tag{23}$$

where ρ is the average density of the cluster [3]. Substituting into Eq. (22) we find

$$\begin{aligned} W &= -\int_0^R G\frac{16\pi^3}{3}\rho^2 r^4 \mathrm{d}r, \\ &= -\frac{3}{5}\frac{GM_{\mathrm{TOT}}^2}{R}, \end{aligned} \tag{24}$$

where we have defined the total cluster mass M_{TOT} to be

$$M_{\mathrm{TOT}} = \frac{4\pi}{3}\rho R^3. \tag{25}$$

We can estimate the average kinetic energy by using the measured Doppler velocity dispersion and the equation

$$K = \frac{1}{2}M_{\mathrm{TOT}}\sigma_v^2. \tag{26}$$

Now, using the virial theorem with our estimated value for the mass of the 800 galaxies we can see what we would expect the velocity dispersion to be:

$$\begin{aligned} \sqrt{\frac{3}{5}\frac{GM_{\mathrm{TOT}}}{R}} &= \sigma_v, \\ &= 80\mathrm{km\ s}^{-1}. \end{aligned} \tag{27}$$

However, the value that Zwicky observed was instead around 1000 km s^{-1}. This discrepancy led Zwicky to conclude that the true mass of the cluster must be much higher than M_{TOT}.

Rearranging Eq. 27, we can use the observed velocity dispersion to calculate the "real" cluster mass

$$\begin{aligned} M_{\mathrm{TOT}} &= \frac{5}{3}\frac{R}{G}\sigma_v^2, \\ &= 1.25 \times 10^{14} M_\odot. \end{aligned} \tag{28}$$

This value for the cluster mass is around 200 times greater than that predicted from the visible mass alone. Therefore, based on Zwicky's measurements, only around 1% of the matter within the Coma cluster is visible. The remaining 99% is unseen dark matter.

[3] This is often called a "tophat" density profile.

B. Rotation Curves

Many were not convinced of the existence of dark matter, however, until Rubin and Ford measured the rotation curve of the Andromeda Galaxy in the 1970's [7]. Using the Doppler effect, they measured the velocity of both stars and gas at orbital radii much larger than previously possible.

To calculate the predicted velocity curve, we will assume that particles, whether they are stars, gas or DM, follow circular orbits. Consider a particle of mass m travelling at an orbital radius r. The mass enclosed within the particle's orbital sphere M, exerts a gravitational force on the particle given by

$$F_g = \frac{GMm}{r^2}, \tag{29}$$

where G is the gravitational constant. The particle has a centripetal acceleration

$$a = \frac{v_{\text{circ}}}{r}, \tag{30}$$

where v_{circ} is the circular velocity of the particle. This is related to the gravitational force via Newton's second law ($F = ma$). Therefore, we can write the circular velocity as

$$v_{\text{circ}} = \frac{GM(< r)}{r}. \tag{31}$$

We see from this equation, that by measuring the velocity of an object with some orbital radius, we can determine the mass contained within that radius.

The majority of the stars, which account for most of the visible mass, are contained within a central bulk. Therefore, as a first approximation, we can model the density of the visible mass component as a top-hat overdensity

$$\rho(r) = \begin{cases} \rho_0 & \text{for } r < r_*, \\ 0 & \text{for } r > r_*. \end{cases} \tag{32}$$

where r_* is the radius of the central star containing region. The mass profile of a general density profile $\rho(r)$ is given by

$$M(r) = 4\pi \int_0^r \rho(r') r'^2 \mathrm{d}r'. \tag{33}$$

Therefore, for our top-hat overdensity, we obtain an internal mass profile given by

$$M(r) = \frac{4\pi\rho_0}{3} \begin{cases} r & \text{for } r < r_*, \\ r_* & \text{for } r > r_*. \end{cases} \tag{34}$$

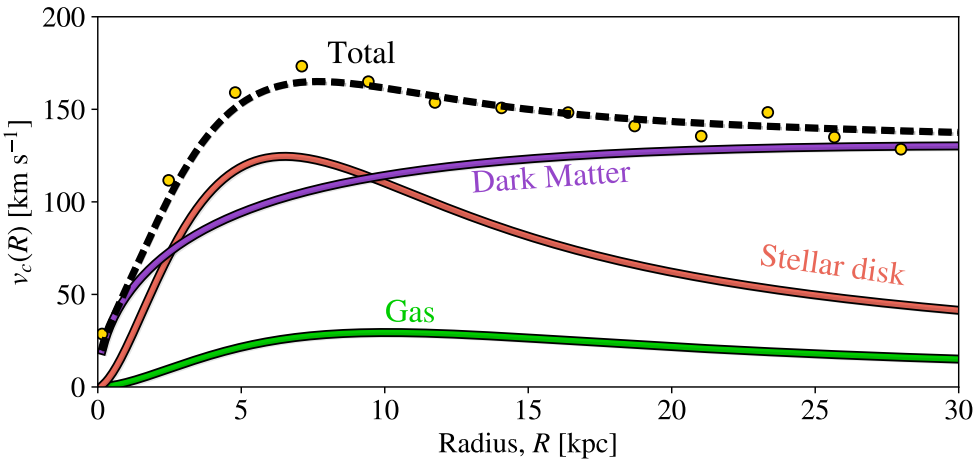

FIG. 1. *Velocity curve contributions.* Cartoon of typical contributions to a galaxy's velocity curve from stars (stellar disk), gas and DM [93].

Therefore, our predicted velocity curve increases with radius for $r < r_*0$ and then decreases for larger radii

$$v_c(r) \sim \begin{cases} r & \text{for } r < r_*, \\ R^{-1/2} & \text{for } r > r_*. \end{cases} \tag{35}$$

However, as shown in Fig. 1, the observed velocity curve tends instead to flatten out at large radii. Looking at Eqs. 31 and 33, we see that this can be achieved by having a density profile $\rho(r) \sim r^{-2}$.

One way of achieving this is by assuming that there is an additional component contributing to the velocity curve at much larger radii. Since gas plays a sub-dominant role, we will neglect it and assume that there is only stars and DM. Since we know the combined mass profile from the galaxy rotation curve, we can calculate the radial density of DM by subtracting from this the visible component

$$M_{\rm DM}(r) = \frac{r}{G}(v_{\rm tot}^2 - v_{\rm vis}^2) \tag{36}$$

There are a number of models for DM density profiles including the isothermal sphere, Einasto and Burkert profiles [94, 95]. However, the most popular is Navarro-Frenk-White (NFW) profile given by

$$\rho_{\rm NFW}(r) = \frac{\rho_0}{\left(\frac{r}{r_s}\right)\left(1+\frac{r}{r_s}\right)^2}, \tag{37}$$

where ρ_0 and r_s are the scale radius and density respectively [89]. We see that this has a slope of r^{-1} at small radii and a steeper slope of r^{-3} at larger radii. Importantly, at the scale radius, the NFW profile also gives the previously predicted slope of $\rho \sim r^{-2}$.

C. The Bullet Cluster

The visible mass of galaxy clusters tends to be dominated by hot intracluster gas. When two such clusters collide, the galaxies act like collisionless particles and pass through each other largely undisturbed. However, the intracluster gas experiences ram pressure. Therefore, much of this gas gets "stuck" in the middle of the collision. This means that if there was no dark matter, we would expect the majority of the mass to be located between the two colliding clusters. However, if most of the matter was composed of a collisionless dark matter, we would instead expect most of the mass to be contained in two distinct separate bulges.

The famous "Bullet cluster" gives us the opportunity to test exactly this scenario. However, first, we need a way to determine where most of the mass is located.

1. X-ray emission

Much like before, we can equate the outward force, this time due to the pressure $F = \nabla P$, to the inward force due to gravity. Doing so gives

$$\frac{\mathrm{d}P}{\mathrm{d}r} = -\rho_{\mathrm{gas}} a(r). \tag{38}$$

If we model the gas using the ideal gas law we have

$$PV = nRT \tag{39}$$

where V is the gas volume, n is the number of moles and $R = 8.31$ is the ideal gas constant. This can be rewritten as

$$P = k_{\mathrm{B}} T \frac{\rho_{\mathrm{gas}}}{\mu} \tag{40}$$

where k_{B} is the Boltzmann constant and μ is the molecular weight. Differentiating with respect to the radius we obtain

$$\frac{\mathrm{d}P}{\mathrm{d}r} = \frac{k_{\mathrm{B}}}{\mu}\left(T\frac{\mathrm{d}\rho_{\mathrm{gas}}}{\mathrm{d}r} + \rho_{\mathrm{gas}}\frac{\mathrm{d}T}{\mathrm{d}r}\right) \tag{41}$$

If T is roughly constant and $\rho \sim r^{-p}$ with $1.5 < p < 2$, we can estimate the temperature of an region of gas by

$$k_{\rm B}T \approx (1.3 - 1.8)\text{keV} \left(\frac{M}{10^{14} M_\odot}\right) \left(\frac{1\text{Mpc}}{r}\right). \tag{42}$$

Therefore, if we are able to measure the temperature of a region of gas, we can estimate the *total* internal mass. Hot gas emits light with a frequency depending on the temperature. The Bullet Cluster has an intracluster gas temperature of around 17keV and therefore emits X-ray photons [96]. The gas distribution is shown in Fig 3. We see that, as predicted, the gas is contained largely between the two clusters as it has been slowed by ram pressure.

2. Gravitational lensing

Another method we can use to "weigh" a region of space is gravitational lensing. In the presence of a gravitational field, the path of light is bent, much like in a normal lens. Johann Georg von Soldner was one of the first to hypothesis the existence of this phenomenon in 1801 using Newtonian mechanics. However, the deflection of light by gravity could only be correctly calculated after Einstein published his theory of general relativity [11]. The effect was first observed by Arthur Eddington and Frank Watson Dyson during a total eclipse in 1919. The eclipse allowed Eddington and Dyson to measure the positions of stars close to the Sun on the sky. They found that their apparent positions had been shifted by the Sun's gravity, just as predicted by Einstein [97].

The effect of gravitational lensing is a Lagrangian mapping of the surface brightness pattern

$$f'(\theta) = f(\psi_{ij}\theta_j) \tag{43}$$

where θ_j is a position on the sky and ψ_{ij} is the *image shear tensor* as shown in Fig. 2. In the weak lensing regime, this is close to unity [98].

Since both the distance between the light source and lens $D_{\rm LS}$ and the distance between the observer and the gravitational lens $D_{\rm L}$ are so large, we can approximate the lens as being a two-dimensional object perpendicular to the line-of-sight. For planar lenses

$$\psi_{ij} = \delta_{ij} - \phi_{ij}, \tag{44}$$

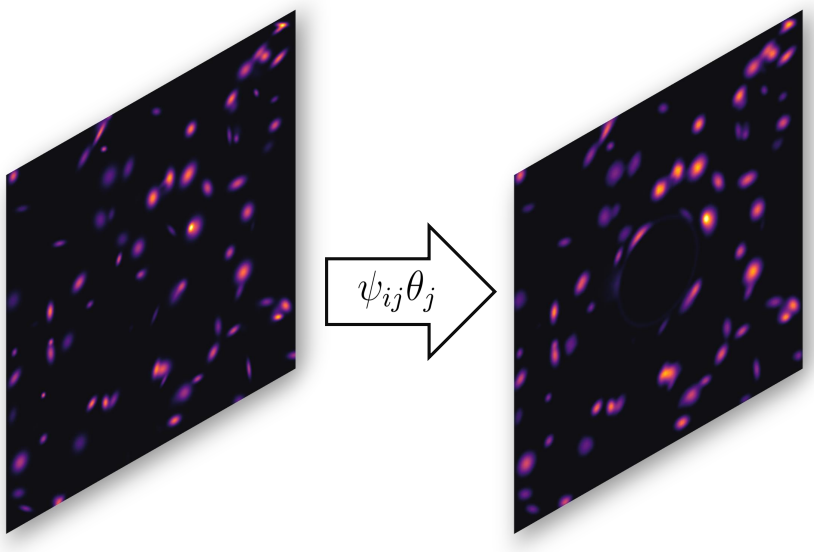

FIG. 2. *Weak lensing example.* Surface brightness pattern has been before (left) and after (right) gravitationally lensed by an unseen foreground point-mass object.

where ϕ is the dimensionless surface density. This surface density is given by

$$\nabla^2\phi = \frac{2\Sigma}{\Sigma_{\rm crit}}, \tag{45}$$

where Σ is the projected mass density given by

$$\Sigma(\theta_j) = \int_{\infty}^{\infty} \rho_{\rm los}(\theta_j)\mathrm{d}z, \tag{46}$$

in which $\rho_{\rm los}$ is the density along the line-of-sight, and where

$$\Sigma_{\rm crit} = \frac{1}{4\pi G}\frac{D_{\rm S}}{D_{\rm L}D_{\rm LS}} \tag{47}$$

is the critical surface mass density and $D_{\rm S} = D_{\rm L} + D_{\rm LS}$ is the distance from the observer to the source.

Most of the gravitational lensing images that we see, for example from the Hubble Space Telescope[4], are of strong gravitational lensing. In this regime, distortions are clearly visible with the formation of multiple images and sometimes Einstein rings.

However, in the weak lensing regime, the distortion of the background light sources is very small and hence difficult to detect. However, by making measurements of a large

[4] See here for an example image.

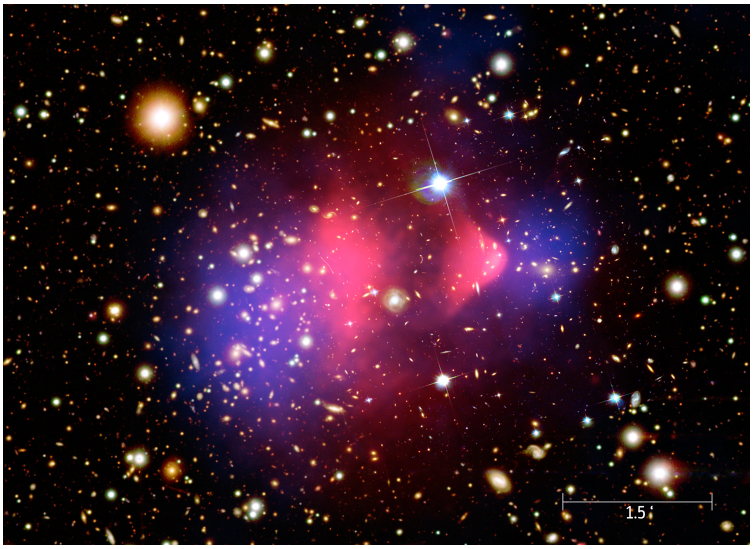

FIG. 3. *Bullet Cluster*. The gas distribution can be inferred from X-ray emissions seen in red, while the total mass distribution, calculated from gravitational lensing, is shown in blue. Public Domain image from NASA.

number of sources, it is possible to find small coherent distortions and hence reconstruct the gravitational potential and hence mass distribution.

The ellipticity of a galaxy is defined as

$$|\epsilon| = \frac{a-b}{a+b} \tag{48}$$

where a and b are the lengths of the semi-major and semi-minor axes. Under weak lensing, the galaxies will exhibit a small statistical preference for aligning perpendicular to the direction to the centre of the lens.

This is exactly what was done with the Bullet Cluster. By measuring the statistical distortion of background galaxies, researchers were able to reconstruct the total mass distribution for the cluster. This is shown in blue in Fig. 3. We see that most of the matter is contained in two, well defined, separate clumps that are *decoupled* from the gas distribution derived from X-ray emissions shown in red.

This tells us that the majority of the cluster's matter cannot be in the form of intracluster gas but must instead be some collisionless material that does not experience the same ram pressure as the gas.

This is one of the strongest pieces of evidence in support of DM. In particular, it supports the idea of DM over a modified theory of gravity as it is very difficult to construct a theory

of gravity that can explain this observation [99].

D. Cosmic Microwave Background

For around the first 370,000 years, the universe was filled with a hot "soup" of subatomic particles. When protons and electrons combined to form a neutral hydrogen atom, they would quickly absorb a high energy photon and be torn apart again. The mean free path of photons was extremely small as they were constantly scattering off of free electrons. As a result, the universe was opaque to electromagnetic radiation [100].

Like all electromagnetic radiation, the wavelength of the photons emitted grows due to the expansion of space. The extent to which these wavelengths grow is called redshift z and is defined by

$$1 + z = \frac{\lambda_{\text{obs}}}{\lambda_{\text{emit}}}, \tag{49}$$

where λ_{obs} and λ_{emit} are the observed and emitted wavelengths respectively. Since the Universe has always been expanding, we can also use redshift as a unit of time which extends from ∞ at the Big Bang to zero today.

The main reaction during this period

$$p + e^- \longleftrightarrow H + \gamma, \tag{50}$$

occurred rapidly enough to be in near thermal equilibrium. We can therefore model their relative abundances using the Saha equation

$$\frac{n_p n_e}{n_{\text{H}}} = c^3 \left(\frac{m_e k_{\text{B}} T}{2\pi\hbar^2}\right)^{3/2} \exp\left(-\frac{E_{\text{I}}}{k_{\text{B}} T}\right), \tag{51}$$

where n_p, n_e and n_{H} are the number densities of protons, electrons and hydrogen respectfully, m_e is the electron mass, T is the temperature of the universe and $E_{\text{I}} = 13.6\text{eV}$ is the ionisation energy of hydrogen.

Assuming the universe is neutral ($n_p = n_e$) the relative abundance of free electrons and ionised hydrogen is given by

$$x_e = x_p = \frac{n_e}{n_p + n_{\text{H}}}. \tag{52}$$

We can use this to rewrite Eq. 51 as

$$\frac{x_e^2}{1 - x_e} = \frac{c^3}{n_p + n_{\text{H}}} \left(\frac{m_e k_{\text{B}} T}{2\pi\hbar^2}\right)^{3/2} \exp\left(-\frac{E_{\text{I}}}{k_{\text{B}} T}\right). \tag{53}$$

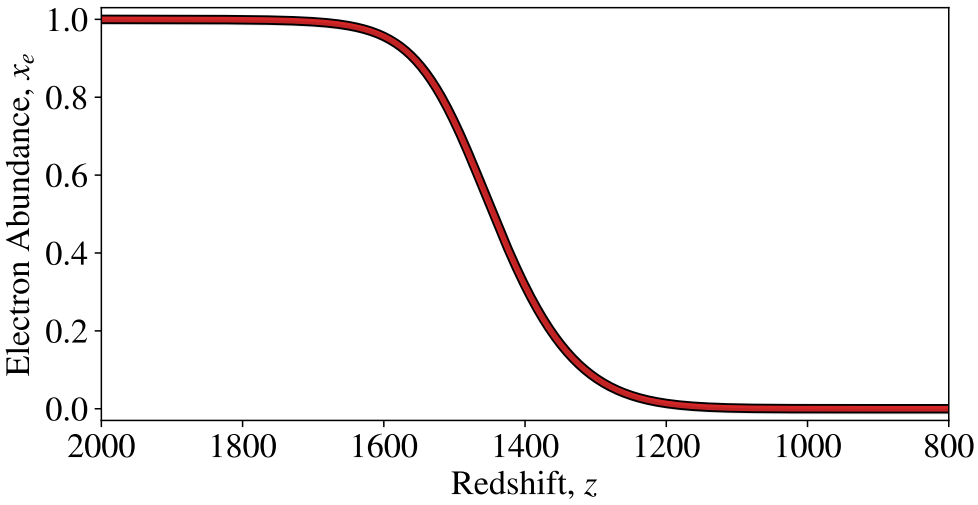

FIG. 4. *Relative Electron Abundance.* Rough estimate for the relative electron abundance calculated using the Saha equation.

The combined number density of protons and hydrogen today is around 1.6m^{-3}. Therefore, since the length scales of the universe grow as $(1+z)^{-1}$ we know that

$$n_p + n_{\text{H}} = 1.6(1+z)^3 \text{ m}^{-3}. \tag{54}$$

Additionally, we know that the temperature of the universe today is around 2.728K. During matter-domination, the temperature evolves as $\sim (1+z)$. Therefore, we can write that

$$T = 2.728(1+z) \text{ K}. \tag{55}$$

Using Eqs. 54 and 55 we can estimate the solve 53 for x_e over time as shown in Fig.4[5].

We see that the free-electron abundance (and hence ionisation fraction) is equal to one at early times. Then, at some later redshift, this fraction falls very quickly to zero as all of the protons and electrons combine to form neutral hydrogen. We call this *recombination*[6]. We can make a rough estimate for when this occurs by finding the point at which $x_e = 0.5$. Doing so we find that $z_{\text{re}} \approx 1450$ at a temperature $T \approx 3940$K. A more careful calculation finds that $z_{\text{re}} \approx 1100$ [17].

When this happens, the photon mean-free path suddenly becomes much larger and the universe quickly goes from being opaque to transparent. Photons then *free-stream* from

[5] This code can be found on my GitHub page here: https://github.com/David-Ellis/thesis-code/blob/main/recombination

[6] This name is a little misleading since the protons and electrons were never combined before. However, for historical reasons, the name has stuck.

their point of last scattering. Assuming a black-body spectrum, we can estimate the peak wavelength of this radiation using Wien's law:

$$\lambda_{\text{peak}} \approx \frac{2.898 \times 10^6 \text{nm K}}{T}. \tag{56}$$

Using our temperature estimate we find $\lambda_{\text{peak}} \approx 735$nm relating to the near-infrared.

Most of these photons, first produced nearly 14 billion years ago, are still travelling freely through space. However, as space has expanded, their wavelengths have also been lengthened proportionally and are now microwave photons. This means that we perceive microwave photons to be travelling towards us from all directions of space. This is exactly what we see! We call this the *cosmic microwave background* (CMB).

As mentioned previously, when the CMB was first detected in 1965, it was found to be completely homogeneous. However, as measurements have improved, astronomers began to notice small isotropies in the CMB temperature across the sky. We can decompose these temperature fluctuations as

$$\frac{\delta T}{T} = \sum_{\ell,m} a_{\ell,m} Y_{\ell,m}(\theta, \phi), \tag{57}$$

where $Y_{\ell,m}$ are the Legendre polynomials for coordinates on the sky (θ, ϕ). The observable C_ℓ, shown in Fig. 6, is a two point correlation function given by

$$\langle a_{\ell m} a_{\ell' m'} \rangle = \delta_{\ell\ell'} \delta_{mm'} C_\ell. \tag{58}$$

This is an expansion with multipole moment ℓ. The scale of these fluctuations on the sky is given by $\ell/180^{\text{o}}$.

We can see from Fig. 5 how successive space telescopes COBE, WIMP and Planck have improved measurements of the small scale anisotropies [15–17]

These isotropies reflect the initial distribution of baryons and DM in the universe. Importantly, baryons are tightly coupled to the photons which DM, by definition, is not. Without going through the derivation, we can relate the current CMB power spectrum to the matter-energy density of matter Ω_m, baryons Ω_b and dark energy Ω_Λ. We find that it is only possible to get the correct spectrum if most of the matter is non-baryonic. By fitting our model for the CMB to the observed data, as shown in Fig. 6, we find that $\Omega_b = 0.05$, $\Omega_{\text{dm}} = \Omega_m - \Omega_b = 0.26$ and $\Omega_\Lambda = 0.69$ [17].

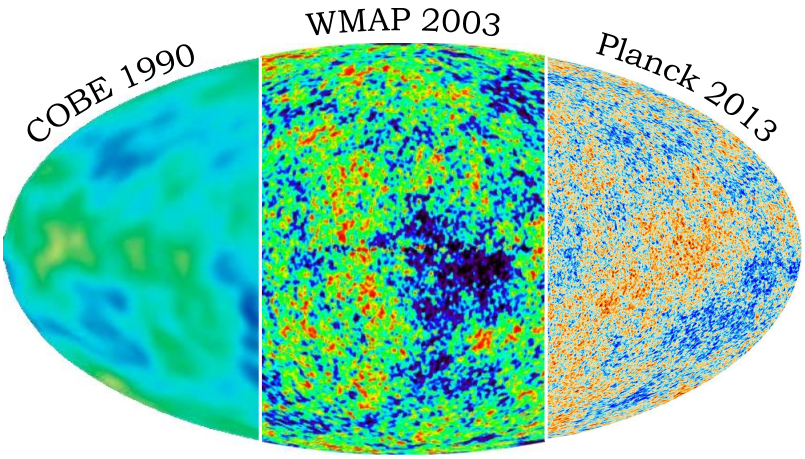

FIG. 5. *Cosmic Microwave Background.* Improvement in the CMB measurements from successive space telescopes COBE, WIMP and Planck. Modified from Refs. [15], [16] and [17] respectively.

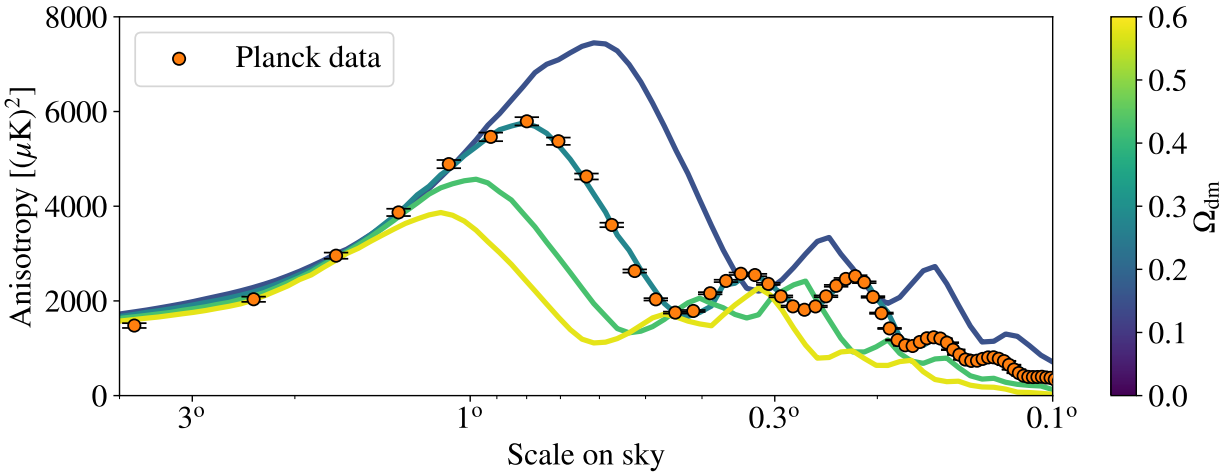

FIG. 6. *Fitting* $\Omega_{\rm dm}$ *to CMB data.* [17]. Reproduced using simulation data presented in Ref. [101].

III. DARK MATTER CANDIDATES

A. WIMPS

Weakly interacting massive particles (WIMPs) are one of the most popular DM candidates and are possibly the most extensively researched. Here "weakly interacting" can either refer to them interacting via the weak force, that is through the exchange of Z bosons, or simply to the fact that they interact with a very small coupling strength.

WIMPs are typically parameterised by their mass m_χ and their thermally averaged an-

nihilation cross-section $\langle\sigma v\rangle$. As mentioned before, these particles are normally assumed to be produced thermally in the early universe through a process known as freeze-out. In the next subsection we will determine the combinations of m_χ and $\langle\sigma v\rangle$ which give the observed relic density $\Omega_{\rm dm}h^2 = 0.12$.

1. Freeze-out and the WIMP miracle

There are two mechanisms in which WIMPs (denoted χ) can interact with SM particles:

- *Elastic scattering*: $\chi + \text{SM} \longleftrightarrow \chi + \text{SM}$. This is analogous to pool balls bouncing off of each other. This does not change the number of WIMPs.
- *Inelastic scattering*: $\chi + \chi \longleftrightarrow \text{SM} + \text{SM}$. This is the annihilation of a pair of WIMPs into SM particles (or the reverse) and therefore does change the number of WIMPs.

We see that both of these interactions can go backwards as well as forwards.

At high temperatures and pressures, the backwards processes occur at a rate equal to the forward processes. For elastic scattering, this maintains kinetic equilibrium while for inelastic scattering this maintains chemical equilibrium.

For a non-relativistic ($m \gg T$) a fermion is in chemical equilibrium, its number density is given by

$$n_{\rm eq} = g\left(\frac{mT}{2\pi}\right)^{3/2}\exp\left(-\frac{m}{T}\right), \tag{59}$$

where m is its mass and $g = 2$ for fermions. The radiation bath has an entropy density given by

$$s = \frac{2\pi}{45}g_{\star s}(T)T^3, \tag{60}$$

in which $g_{\star s}(T)$ is the number of entropic degrees of freedom of the thermal bath. We define the WIMP abundance to be $Y = n_\chi/s$. Starting from the collisional Boltzmann equation, it can be shown that abundance evolves as

$$\frac{x}{Y_{\rm eq}}\frac{dY}{dx} = \frac{-n_{\rm eq}(T)\langle\sigma v\rangle}{H(T)}\Big[\Big(\frac{Y}{Y_{\rm eq}}\Big)^2 - 1\Big]. \tag{61}$$

where $Y_{\rm eq} = n_{\rm eq}/s$. We see that $x = m_\chi/T$ acts as a time variable since T falls over time.

Solving this equation numerically with the initial condition $Y = Y_{\rm eq}$, as shown in Fig. 7, we see that the abundance tends to some constant value. This occurs at the point of chemical decoupling.

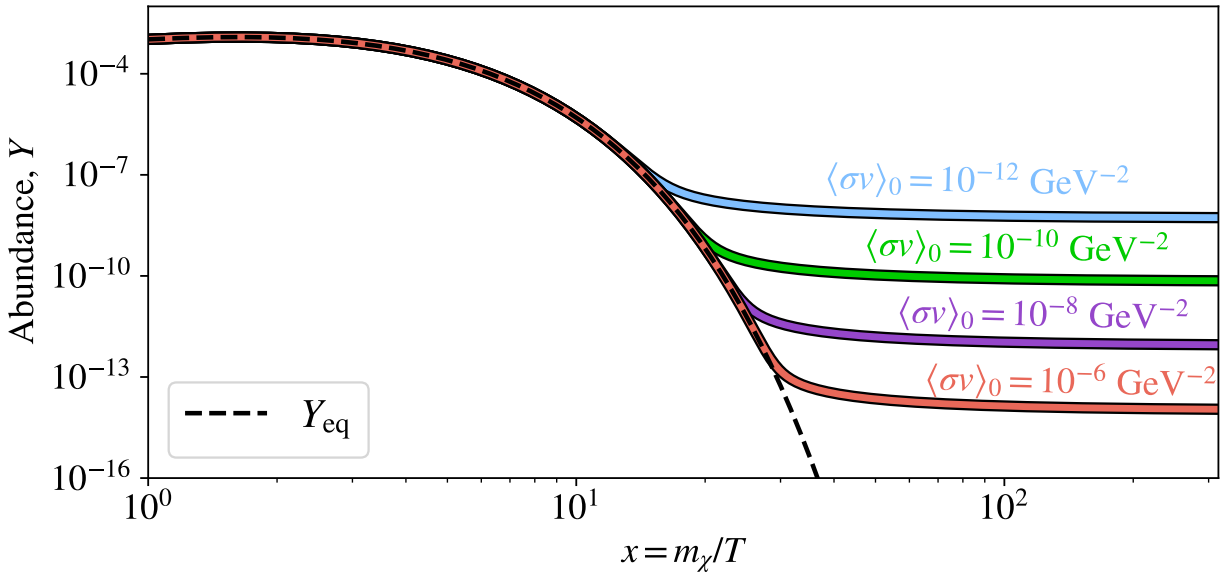

FIG. 7. *WIMP abundance.* Calculated for a WIMP with temperature independent annihilation cross section, for four different values of the cross section. The result is found by numerically solving the Boltzmann equation as given in Eq. 61 with equilibrium initial condition using numerical calculation of $g_\star(T)$ from Ref. [102].

Since the abundance tends towards a constant, we can use our solution of the Boltzmann equation to calculate the final value for the abundance Y_∞. We can use this to estimate the WIMP number density today as

$$n_{\chi 0} = Y_\infty s_0, \tag{62}$$

$$= \frac{2\pi^2}{45} g_{\star s}(T_0) T_0^3 Y_\infty, \tag{63}$$

where $T_0 = 2.728$K is the temperature of the universe today. The number density is, by definition, related to the relic density Ω_χ by

$$\rho_\chi = m_\chi n_\chi = 3 M_{\rm H}^2 M_{\rm pl}^2 \Omega_\chi h^2, \tag{64}$$

where $M_{\rm H} \equiv H/h$ and $M_{\rm pl} \equiv \sqrt{1/8\pi G}$ are the Hubble and reduced Planck masses respectively. We can then write down the relation between Y_∞ and the relic density as

$$Y_\infty = \frac{45}{2\pi^2} \frac{3 M_H^2 M_{pl}^2}{T_0^3} \frac{1}{g_{*s}(T_0)} \frac{\Omega_\chi h^2}{m_\chi}. \tag{65}$$

We can therefore solve Eq. 61 as function of m_χ and $\langle\sigma v\rangle$ and calculate the resulting relic

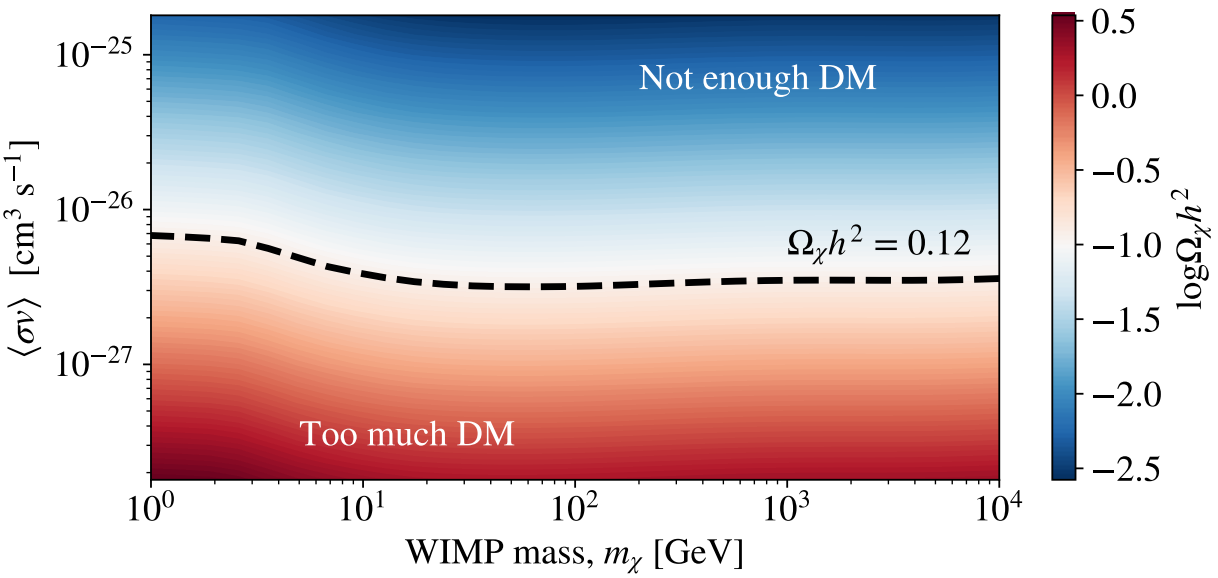

FIG. 8. *WIMP relic density.* Calculated for a WIMPs with temperature independent annihilation cross section,. The result is found by numerically solving the Boltzmann equation as given in Eq. 61 with equilibrium initial condition using numerical calculation of $g_\star(T)$ from Ref. [102].

density as shown in Fig. 8. We see that there's a single $(m_\chi, \langle\sigma v\rangle)$ curve which produces the observed relic density.

One particularly interesting WIMP mass is $m_\chi = 100$GeV as this is roughly equal to the electroweak scale given by the Higgs vacuum expectation value when electroweak symmetry breaking happens. It can be shown that if we set all of the appropriate constants to the weak scale we predict a cross-section $\langle\sigma v\rangle \approx 10^{-26}\text{cm}^3\text{s}^{-1}$ [93]. We see from Fig. 8 that this isn't too far from the cross-section required to give us the observed relic DM density. This is known as the *WIMP miracle*.

2. Constraints

There are a number of constraints on the WIMP parameter space. These include astrophysical considerations such as the sizes of galaxies [33], indirect detection such as the detection of γ-rays [36] and direct detection [103]. We will briefly outline the last of these.

When a WIMP collides with some SM nucleus N they interact via some "portal" boson (e.g. Z, W or H from the SM or possibly some yet undetected boson). This boson carries

momentum which elevates the nucleus to an excited state N^*. After some time, this excited nucleon will return to its original state by emitting some radiation such as a photon or phonon. Therefore, by detecting this radiation, it is possible to infer that this collision has taken place.

The differential rate of collision events per unit of detector mass is given by

$$\frac{\mathrm{d}R}{\mathrm{d}E_{\mathrm{nr}}} = \frac{1}{2m_{\mathrm{N}}}\frac{\rho_\chi}{m_\chi}\left\langle v\frac{\mathrm{d}\sigma}{\mathrm{d}E_{\mathrm{nr}}}\right\rangle. \tag{66}$$

where $\rho_\chi \approx 0.4$ GeV cm^{-3} is the local DM density, m_{N} is the mass of the target nucleon and the term in the angle brackets is the average differential cross-section over the local dark matter velocity distribution v_{dm} [104].

WIMP direct detection experiments often use liquid noble gas as their detector material [103]. The first WIMP direct detection experiment was the Homestake Mine Experiment which, in 1987, used 135 cm^3 of Germanium [105]. However, the three most sensitive WIMP direct detection experiments to date, Xenon1T, LUX and PandaX-II all use liquid xenon [106–108]. One of the first of these, Xenon1T, currently provides the strongest constraints on the spin-independent WIMP-proton cross-section $\sigma_{p,\mathrm{SI}}$ shown in Fig. 9.

As mentioned previously, one of the most well-motivated WIMP candidates comes from SUSY. One model, in particular, is the seven-dimensional Minimal Supersymmetric Standard Model (MSSM7). Using this model, it is possible to estimate where we are most likely to find the WIMP given the vast range of existing constraints. Fig. 9 shows the profile likelihood function for MSSM7 calculated by the GAMBIT collaboration [109][7].

One of the greatest challenges for these detectors is the elimination of background noise. A common strategy is to build such detectors deep underground to help block background sources such as solar rays. For example, Xenon1T was conducted below Gran Sasso mountain in Italy, covered by around 1400m of rock [110].

However, not all background sources can be eliminated. Like WIMPs, neutrinos interact only very weakly with other matter and therefore can not be shielded against. For sufficiently sensitive detectors, neutrinos will provide a background detection rate that looks very similar to the expected WIMP signal. This *Neutrino floor* has previously been thought of as a hard limit that prevents us from being able to detect the WIMP. However, it has been shown that, with enough statistics, it is possible to overcome this limit. For example, one could

[7] This calculation crossed the "current bounds" line since it does not include results from Xenon1T.

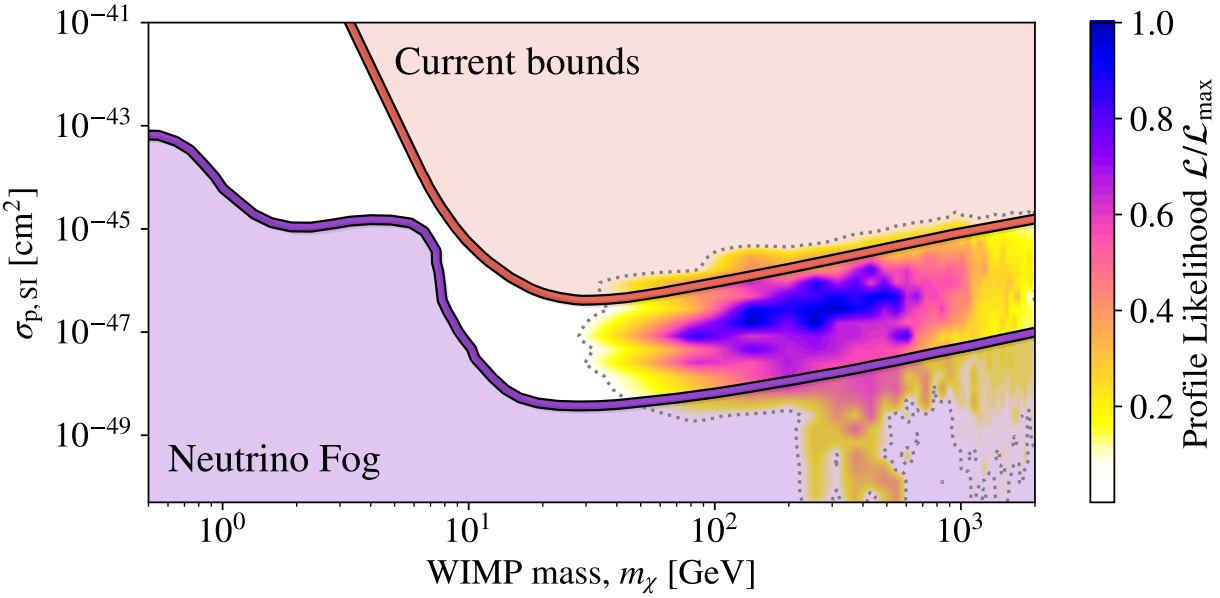

FIG. 9. *WIMP-proton cross-section.* Red shaded: Xenon1T constraints on the WIMP-proton cross-section [106]. Purple shaded: Edge of the "neutrino fog" beyond which neutrino detection complicates WIMP detection (For a xenon-based detector) [113]. We also show the profile likelihood function for MSSM7 found using the GAMBIT framework taking into considerations a wide range of existing constraints on the WIMP parameter space [109]. Dotted line indicates the 68% confidence interval.

look for periodic modulations in the direct detection signal that are expected for DM but not background neutrinos [111, 112]. It has therefore been suggested that we should instead consider a *neutrino fog*. The edge of this fog is shown in Fig. 9 [113].

We can see from Fig. 9 that there is very limited parameter space left above the edge of the neutrino log. We also see that the "most likely" region calculated by GAMBIT extends below this floor giving us the so-called "WIMP from hell" which would be particularly difficult to detect.

B. PBHs

We know that's there can't be many more baryons than we see because of their strong coupling with photons. We know that DM must be (at least almost) completely invisible. We also know that if too many baryons were present around recombination the spectrum of

anisotropies in the CMB would look much different to what we observe. However, we can get around this if the baryons are "locked up" in black holes.

The black holes we normally think of are formed from the death of stars. The first halos which are able to form stars are believed to first form at $z \lesssim 30$ [114]. Since this is much later than the recombination (and hence the emission of the CMB), if black holes do make up DM, they cannot form this way. Instead, for DM to be made of black holes, they would have to form via some exotic mechanism in the very early Universe. This is why they are known as *primordial* black holes (PBHs).

1. *Collapse of PBHs*

There are a number of different ways in which these early overdensities can form. Normally, we assume that PBHs are formed from the collapse of large density perturbations generated by inflation [30].

Consider a region of space with an overdensity $\delta \equiv \delta\rho/\bar{\rho}$. Using Newtonian gravity, it can be shown that, when the scale of this region enters the horizon, it will form a PBH if the overdensity exceeds some critical value δ_c. This value is found to be $\delta_c = c_s^2$ where c_s is the speed of sound. Since the collapse takes place during radiation domination, $c_s^2 = 1/3$. The mass of the PBH will have a mass of the order of the mass contained within the horizon when it collapsed

$$M_{\rm PBH} \sim M_{\rm H} \sim \frac{t}{G} \sim 10^{15}{\rm g}\left(\frac{t}{10^{-23}\ {\rm s}}\right), \tag{67}$$

where G is the gravitational constant and t is the age of the universe [30, 115].

The PBH collapse fraction β is given by

$$\beta \equiv \frac{\rho_{\rm PBH}}{\bar{\rho}}. \tag{68}$$

Using the Press-Schechter formalism (Explored further in Sec.IV C), we can estimate this collapse fraction from the initial matter power spectrum $P(\delta)$ as

$$\beta = \int_{\delta_c}^{\infty} P(\delta){\rm d}\delta, \tag{69}$$

$$\approx \frac{1}{\sqrt{2\pi}}\frac{\sigma(M_{\rm PBH})}{\delta_c}\exp\left(-\frac{\delta_c^2}{2\sigma(M_{\rm PBH})}\right), \tag{70}$$

where $\sigma(M)$ is the variance of the fluctuations on the mass scale $M_{\rm PBH}$. From this, it is possible to estimate the PBH relic density as

$$\Omega_{\rm PBH}h^2 = 0.12\left(\frac{\Omega_m}{0.3}\right)\left(\frac{h}{0.7}\right)^2\left(\frac{1+z_{\rm eq}}{3400}\right)^{-1}\left(\frac{T_{\rm col}}{1{\rm GeV}}\right)\left(\frac{2.725{\rm K}}{T_0}\right)\left(\frac{\beta}{6.5\times10^{-10}},\right), \quad (71)$$

where $z_{\rm eq}$ is the redshift of matter-radiation equality and $T_{\rm col}$ is the temperature of the Universe when the PBHs formed. We see that to predict the relic density from our model, we have to calculate β and $T_{\rm col}$ [93]. However, since this is heavily model-dependent, when calculating constraints on PBHs, we normally instead consider the fraction of DM constrained within PBHs of a particular mass $M_{\rm PBH}$ denoted by $f_{\rm PBH}$.

2. Constraints

The first constraint on PBHs does not require any experimentation of astronomical observation but instead comes purely from theoretical considerations. Despite their name, black holes are not perfectly "black". Pairs of virtual particles (one matter, one anti-matter) known as *vacuum fluctuations* can be produced by essentially "borrowing" energy from the universe. As shown in Fig. 10, when these fluctuations occur near the event horizon of a black hole, there are three possible outcomes:

1. The matter anti-matter pair immediately recombine and annihilate each other and the debt to the universe is repaid. This is the most common scenario.

2. Both particles fall into the black hole. The black hole "gains" the mass of the particles but "loses" the same amount of mass repaying the energy debt leading to no net change in the black hole mass.

3. One particle falls into the black hole and the other escapes. Now the black hole has gained the mass of one particle but must pay the debt for the creation of both.

This third scenario provides a way for black holes to *evaporate* over time [41]. The escaping particle is known as Hawking radiation. This emission of particles is thermal and gives the black hole a temperature

$$T_{\rm BH} = \frac{1}{8\pi GM} \approx 100\left(\frac{10^{14}{\rm g}}{M}\right)\ {\rm MeV}, \quad (72)$$

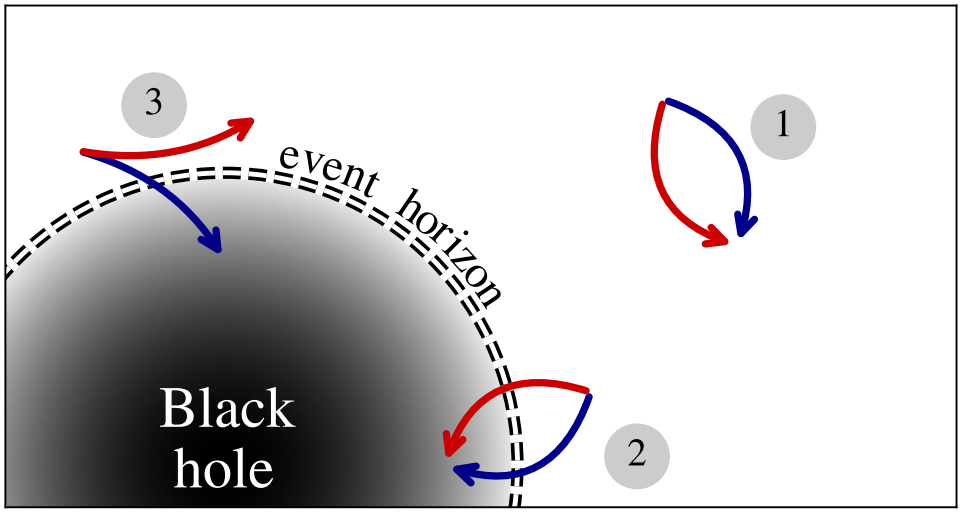

FIG. 10. *Vacuum fluctuations near a black hole.* Particle pairs formed near the edge of a black hole experience one of three fates: 1) annihilation, 2) Both fall into the black hole, 3) One particle escapes (Hawking radiation).

where $GM = R_{\rm Sch}$ is the *Schwarzchild radius*. We see that this temperature is inversely proportional to the mass so smaller black holes are much hotter than large ones. The existence of this Hawking radiation also means that, if the black hole isn't able to consume additional matter, its mass will decrease until it disappears.[8]

From this, it can be shown that the rate of mass change is

$$\frac{\mathrm{d}M}{\mathrm{d}t} \approx \frac{1}{15360\pi G^2}\frac{1}{M^2}. \tag{73}$$

This can then be integrated to find the lifetime of a black hole

$$t_{\rm BH} \approx 5120\pi G^2 M^3, \tag{74}$$

$$\approx 7\times 10^{74}\ \mathrm{s}\left(\frac{M}{M_\odot}\right)^3. \tag{75}$$

However, we know that the age of the Universe is around 14×10^9 years. This gives us a maximum allowed black holes lifetime since any black holes with lifetimes smaller than this will already have evaporated away. Substituting the age of the Universe into Eq. 75 therefore gives us the constraint $M_{\rm PBH} \gtrsim 10^{-19} M_\odot$ [118].

[8] Quantum effects might mean black holes lose mass until they reach some minimum mass. In the final stages of particle emission, the momentum gained from each emission becomes significant leaving behind a small fast-moving remnant that may behave like warm or hot dark matter [116, 117].

Hawking radiation also gives us a second constraint on PBHs as we expect very light black holes to emit a significant number of γ-ray and X-ray photons. Since this cannot exceed the observed background spectrum, we can use measurements of the background spectrum by a range of telescopes to place constraints on the PBH fraction [119–122]. This gives us a larger lower bound of $M_{\text{PBH}} \gtrsim 10^{-16} M_\odot$ as shown in Fig. 11.

On the other end of the spectrum, we can obtain an upper bound on the PBH mass by considering the survival of star clusters in ultra-faint dwarfs such as Eridanus II. PBHs cause a two-body relaxation which heats up the star cluster. This cluster is stable to heating only if the relaxation time is larger than the estimated age. This heating is greater for larger black hole masses. Therefore, without going through the derivation, this leads to an upper bound $M_{\text{PBH}} \lesssim 3 M_\odot$ shown in Fig. 11 [123].

One of the most important observational constraints on PBHs come from *gravitational microlensing*. The basic principle for microlensing is similar to "ordinary" gravitational lensing discussed in Sec. II C 2. The gravitational field of an object between a light source and an observer bends the path of light to produce multiple images of the source. However, in microlensing, the separate images cannot be resolved and are instead detected on a single pixel. This is seen as a brief magnification of the source light.

To date, the best microlensing constraints come from the Subaru-HSC and the EROS surveys. These surveys monitored the brightness of stars in the Andromeda galaxy and the Large Magellanic Cloud respectively [43, 44]. Combined, these surveys place heavy constraints on the PBH fraction in the mass range $10^{-12} M_\odot \lesssim M_{\text{PBH}} \lesssim 15 M_\odot$ as shown in Fig. 11.

We will explore the theory behind gravitational microlensing as well as the HSC and EROS surveys further in Sec. VI.

We see that there is only a rather small mass window remaining ($10^{-17} M_\odot \lesssim M_{\text{PBH}} \lesssim 10^{-12} M_\odot$) in which PBHs can make up all of the DM. One way this window may be closed in the future is by femtolensing surveys [80]. This is similar to microlensing but considers the wave effects imprinted on the source light by the lens.

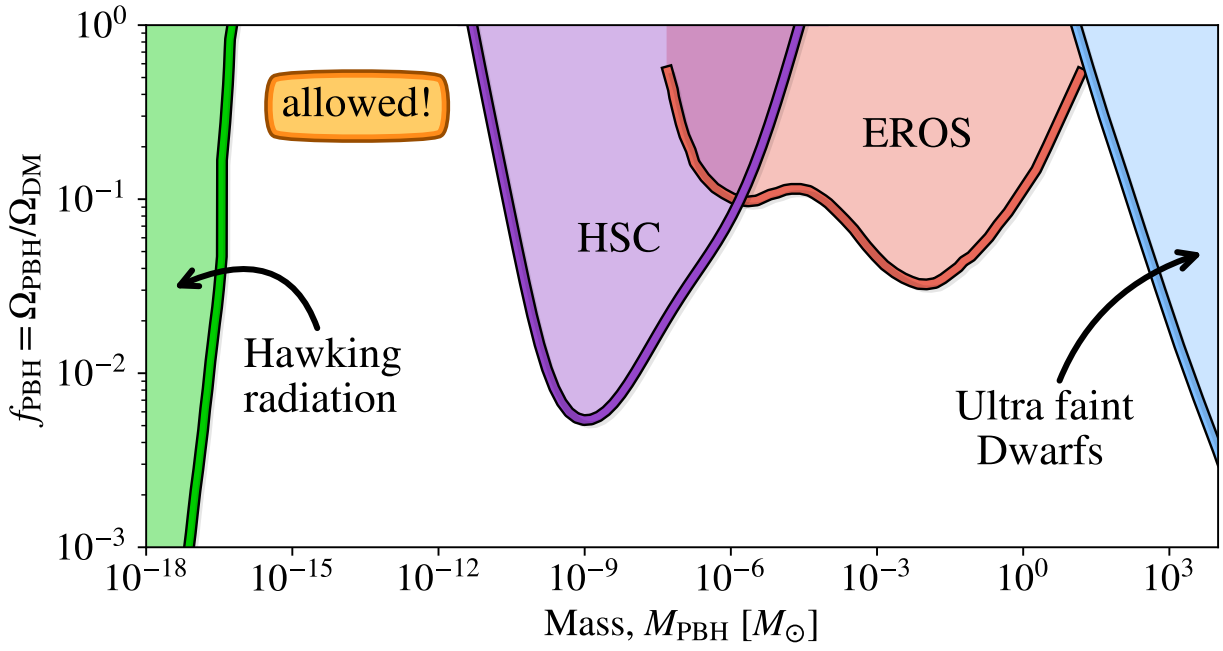

FIG. 11. *PBH Constraints.* Compilation of key constraints on the fraction of DM composed of PBHs including microlensing (HSC and EROS), and X-ray measurements and the survival of ultra faint dwarf galaxies. Data collated by B Kavanagh as part of PBHbounds [124]

C. Axions

The axion is a hypothetical elementary particle that appears in many extensions of the standard model of particle physics. They were first proposed in 1977 by Peccei and Quinn as a way to solve the CP problem of QCD [45]. A physical law has CP symmetry if, after interchanging each particle with its antiparticle and simultaneously inverting the spatial coordinates of the system, the law remains true. As early as 1964, physicists have observed CP symmetry violation in electroweak interactions [125]. However, there is no verified observation of CP violation in the strong sector. The QCD Lagrangian contains a CP violating term with a coefficient proportional to

$$\bar{\theta} = \theta_{\rm QCD} + \arg\det(M_{\rm quark}), \tag{76}$$

where $\theta_{\rm QCD}$ is the θ-vacuum and $M_{\rm quark}$ is the quark mass matrix [126]. A non-zero value for $\bar{\theta}$ would result in the neutrino having an electric dipole moment. However, the absence of such a dipole moment has been confirmed to a precision of $d_{\rm n} < 3.0 \times 10^{-26}$ e cm [127].

To solve this fine-tuning problem, Peccei and Quinn proposed altering the QCD La-

grangian by considering $\bar{\theta}$ as a dynamic field

$$\theta = \frac{\mathcal{C}\phi(x)}{f_a}, \tag{77}$$

where $\phi(\mathbf{x})$ is the axion field, $\mathcal{C}$ is the colour anomaly and f_a is the axion decay constant. This dynamic field is a pseudo-Goldstone boson field that arises from the breaking of a global U(1) symmetry (known as the PQ symmetry) caused by the vacuum expectation values of a scalar field.

Many other axion-like particles (ALPs) have also been predicted by Type IIB string theory as well as other branches of string theory and M-theory including both scalar and pseudoscalar variants [128] [129].

The $U(1)$ symmetry is broken when the temperature of the universe falls below the vacuum expectation value which is equal to the axion decay constant. When this happens, the axion field takes on a random "misalignment angle", $\theta_i(x)$, between zero and 2π. The non-linear realisation of the $U(1)$ symmetry as a shift symmetry for the axion field means that this value is only defined locally. Therefore, the precise distribution of axion DM today depends on when in cosmological history this symmetry is broken. As mentioned previously there are two distinct scenarios depending on whether the symmetry is broken before or after inflation.

After PQ-symmetry breaking, the axion acquires a mass from QCD instantons. Using chiral perturbation theory, this mass can be estimated to be

$$m_a \approx 6 \times 10^{-6} \left(\frac{10^{12}\ \text{GeV}}{f_a/\mathcal{C}} \right). \tag{78}$$

In the next two subsections, we will explore the two different scenarios for PQ symmetry breaking and its consequence for the abundance and distribution of DM today.

1. Pre-inflationary scenario

When PQ symmetry breaking occurs after inflation, the axion can be treated as a single minimally coupled scalar field. From general relativity, the action for such a field is given by

$$S_\phi = \int \mathrm{d}^4x \sqrt{-g}[-\frac{1}{2}(\partial\phi)^2 - V(\phi)] \tag{79}$$

where $g = \det g_{\mu\nu}$. Considering a small perturbation to the field $\phi \to \phi + \delta\phi$

$$S_\phi + \delta S_\phi = \int \mathrm{d}^4x\sqrt{-g}[-\frac{1}{2}(\partial(\phi+\delta\phi))^2 - V(\phi+\delta\phi)]. \tag{80}$$

Taylor expanding $V(\phi+\delta\phi) \approx V(\phi) + \partial\phi\frac{\partial V}{\partial\phi}$ and neglecting terms $\mathcal{O}(\delta\phi^2)$ we find that

$$S_\phi + \delta S_\phi = \int \mathrm{d}^4x\sqrt{-g}[-\frac{1}{2}(\partial\phi)^2 - V(\phi)] + \int \mathrm{d}^4x\sqrt{-g}[-\partial\phi\partial\delta\phi - \delta\phi\frac{\partial V}{\partial\phi}]. \tag{81}$$

Subtracting Eq. 79 we find that

$$\delta S_\phi = \int \mathrm{d}^4x\sqrt{g-}[-\partial\phi\partial\delta\phi - \delta\phi\frac{\partial V}{\partial\phi}]. \tag{82}$$

We then integrate by parts to find

$$\delta S_\phi = \left[\sqrt{-g}\partial\phi\delta\phi\right] + \int \mathrm{d}^4x[\partial(\sqrt{-g}\phi) - \sqrt{-g}\frac{\partial V}{\partial\phi}]\delta\phi, \tag{83}$$

where the first term is zero due to boundary conditions. Applying the chain rule we find

$$\delta S_\phi = \int \mathrm{d}^4x\sqrt{-g}[\partial^2\phi - \frac{\partial\phi\partial\sqrt{-g}}{\sqrt{-g}} - \frac{\partial V}{\partial\phi}]\delta\phi. \tag{84}$$

Therefore, for the action to be minimised for all $\delta\phi$ we require that

$$\partial^2\phi - \frac{\partial\phi\partial\sqrt{-g}}{\sqrt{-g}} - \frac{\partial V}{\partial\phi} = 0 \tag{85}$$

for a spatially flat, expanding universe

$$g_{\mu\nu} = \begin{pmatrix} -1 & 0 & 0 & 0 \\ 0 & a^2(t) & 0 & 0 \\ 0 & 0 & a^2(t) & 0 \\ 0 & 0 & 0 & a^2(t) \end{pmatrix}, \tag{86}$$

therefore

$$g = a^3(t) \implies \partial_i g = 3\dot{a}(t)a^2(t)\delta_{i,t}. \tag{87}$$

Since $H = \dot{a}/a$ we can then write

$$\partial^2\phi + 3H\dot{\phi} - \frac{\partial V}{\partial\phi} = 0. \tag{88}$$

This can be rewritten as

$$\ddot{\phi} + \nabla^2\phi + 3H\dot{\phi} - \frac{\partial V}{\partial\phi} = 0 \tag{89}$$

Finally, using Eq. 77 and taking $\mathcal{C} = 1$, we can rewrite this equation in terms of θ

$$\ddot{\theta} + \nabla^2\theta + 3H\dot{\theta} - \frac{1}{f_a^2}\frac{\partial V}{\partial \theta} = 0 \tag{90}$$

In the pre-inflationary scenario the initial axion field is homogeneous on the scale of the observable universe. Therefore, $\nabla^2\theta = 0$ giving the equation of motion

$$\ddot{\theta} + 3H(T)\dot{\theta} + \frac{1}{f_a^2}\frac{\partial V(\theta)}{\partial \theta} = 0. \tag{91}$$

Additionally, by varying the action with respect to the metric, we can obtain the energy-momentum tensor T^{μ}_{ν}. From this, we calculate the average density and pressure of the axion field to be

$$\bar{\rho}_a = \frac{f_a^2}{2}\dot{\theta}^2 + V(\theta), \tag{92}$$

and

$$\bar{P}_a = \frac{f_a^2}{2}\dot{\theta}^2 - V(\theta), \tag{93}$$

respectively. As given by the dilute instanton gas approximation, we consider a simple harmonic potential of the form

$$V(\theta) = m_a^2(T) f_a^2 (1 - \cos\theta) \tag{94}$$

$$= \chi(T)(1 - \cos\theta), \tag{95}$$

where $\chi(T)$ is the temperature dependent topological susceptibility which is calculated numerically using lattice QCD as shown in Fig. 12 [102, 130].
For small misalignment angles, this can be approximated as

$$V(\theta) = \frac{1}{2}\chi(T)\theta^2. \tag{96}$$

From the Friedmann equations, in a radiation dominated universe the Hubble parameter is given by

$$H^2 = \frac{8\pi}{3M_{\rm pl}^2}\rho, \tag{97}$$

where $M_{\rm pl}$ is the the Planck mass. The rate of change of the energy density is given by

$$\dot{\rho} = -3H(T)sT \tag{98}$$

where s is the with entropy density. The energy and entropy density are then given by

$$\rho = \frac{\pi^2}{30} g_\rho T^4, \tag{99}$$

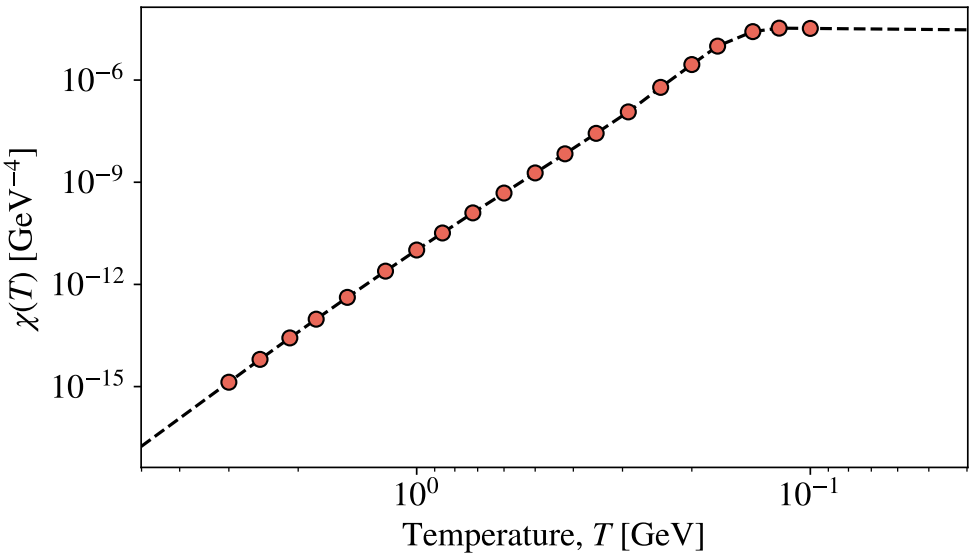

FIG. 12. *Topological susceptibility.* Calculated using lattice QCD data by Ref. [102].

and

$$s = \frac{2\pi^2}{45} g_s T^4, \tag{100}$$

respectively. Combining 98, 99 and 100 we can calculate the reciprocal rate of change of temperature to be

$$\frac{dt}{dT} = -M_{pl}\sqrt{\frac{45}{64\pi^3}}\frac{1}{g_s(T)\sqrt{g_\rho(T)}T^3}\Big[T\frac{dg_\rho}{dT} + 4g_\rho\Big]. \tag{101}$$

Using values of $g_\rho(T)$ and $g_s(T)$ calculated using lattice QCD data in Ref. [102], we can therefore calculate $\mathrm{d}t/\mathrm{d}T$.

We can rewrite our ODE in terms of derivatives in temperature instead of time as

$$\frac{d^2\theta}{dT^2} + \Big[3H(T)\frac{dt}{dT} - \frac{d^2t}{dT^2}\Big/\frac{dt}{dT}\Big]\frac{d\theta}{dT} + \frac{1}{f_a^2}\Big(\frac{dt}{dT}\Big)^2\frac{\partial V(\theta)}{\partial\theta} = 0. \tag{102}$$

With this, we can numerically solve the equation of motion for the homogeneous axion field as demonstrated in Fig. 13. We see from that after a few oscillations n_a/s tends to a constant. We can therefore estimate the axion number density today from our final value of n_a/s as

$$n_{a0} = s_0\left(\frac{n_a}{s}\right)_{\text{final}}, \tag{103}$$

where s_0 is today's entropy density is given by

$$s_0 = \frac{2\pi^2}{45}(2T_\gamma^3 + 6\frac{7}{8}T_\nu^3) = \frac{2\pi^2}{45}\frac{43}{11}T_\gamma^3. \tag{104}$$

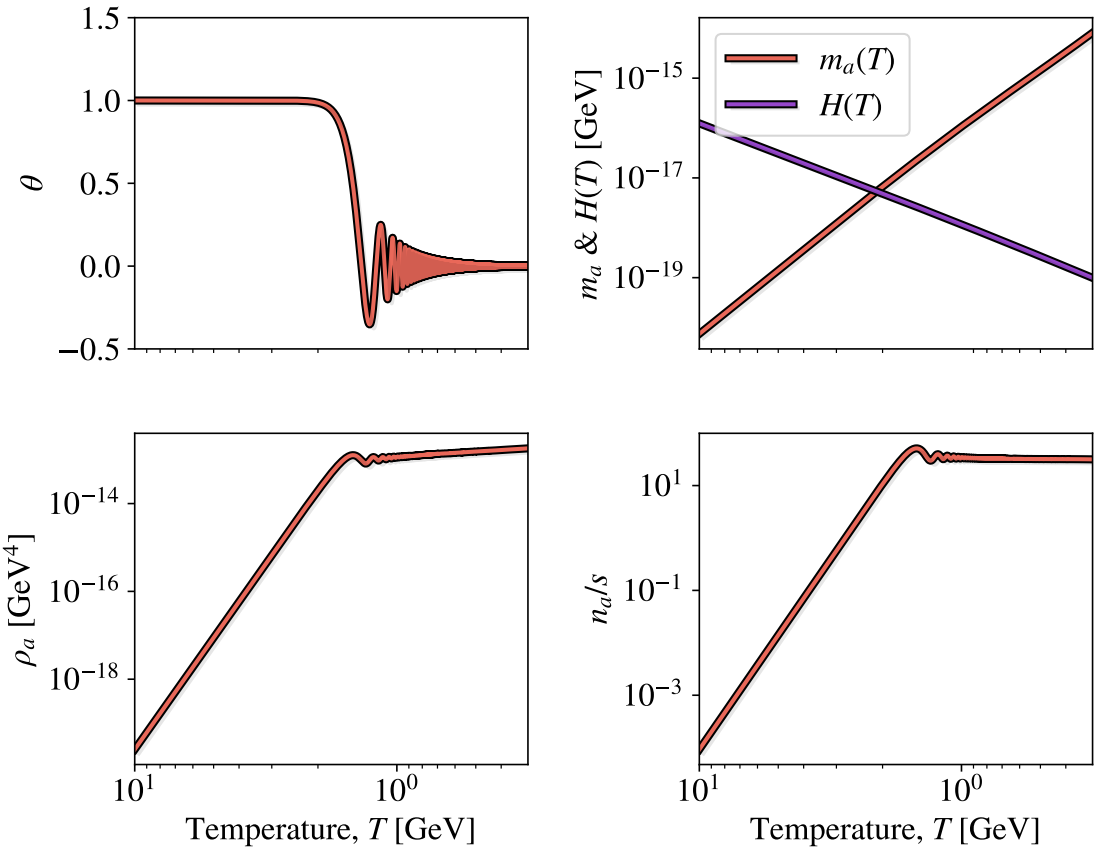

FIG. 13. *Axion field evolution.* Top Left: Evolution of the homogeneous axion field as it decays from $\theta = 1 \to 0$. Top right: Axion mass m_a and Hubble parameter H. Bottom left: Axion energy density ρ_a. Bottom right: Ratio of the axion number density to the entropy density.

We can therefore use our numerical solution of Eq. 102 to calculate some late value of n/s. Then, using Eq. 103, we can find the axion number density today and hence $\Omega_a h^2$ as a function of the decay constant f_a and initial misalignment angle θ_i as shown in Fig. 14.

We see that there exists a single (f_a, θ_i) curve which gives us the correct relic density. If the initial angle is too high, the field takes too long to decay and produces more axionic DM than we observe. However, if the initial angle is instead too small, not enough DM is produced [9]. We see that, for large f_a, in order to solve the strong CP fine-tuning problem, we have introduced a new, albeit less severe, fine-tuning problem.

[9] It is important to note that in this latter case, the axion can still exist, however, it cannot make up all of the dark matter and must coexist with something else

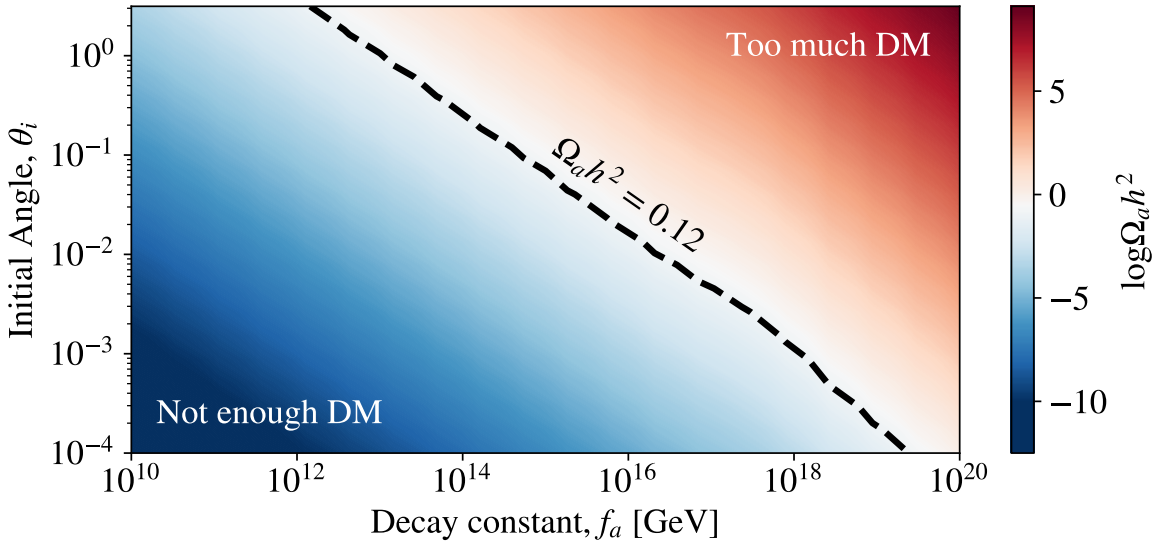

FIG. 14. *Axion relic density.* Calculated by numerically solving Eq. 102 using values for $g_s(T)$, $g_\rho(T)$ and $\chi(T)$ calulated using lattice QCD by Ref. [102].

2. *Post-inflationary scenario*

When PQ-symmetry breaking occurs after inflation, the initial phase of the field (i.e. the axion) will instead be drawn from a random distribution in causally disconnected regions. This consequently produces a network of cosmic strings and domain walls [131, 132]. The decay of these defects produces large amplitude $\mathcal{O}(1)$, small scale density perturbations, which are the seeds for axion miniclusters [55]. These seeds merge together to form axion miniclusters via hierarchical structure formation.

To regularise the core energy of the emergent strings and enable their dynamics requires a UV completion of the axion model. The simplest completion is a complex scalar field given by $\varphi = |\varphi|e^{i\theta}$. This has a Lagrangian density

$$\mathcal{L} = a^3(t)\Big[\frac{1}{2}|\dot{\varphi}|^2 - \frac{1}{2a^2(t)}|\nabla\varphi|^2 - V(\varphi)\Big]. \tag{105}$$

We can apply the Euler-Lagrange equation,

$$\frac{\partial}{\partial\mu}\Big(\frac{\partial\mathcal{L}}{\partial(\partial_\mu\varphi)}\Big) - \frac{\partial\mathcal{L}}{\partial\varphi} = 0 \tag{106}$$

to find the equation of motion

$$\ddot{\varphi} + 3H\dot{\varphi} - \frac{1}{a^2(t)}\nabla^2\varphi - \frac{\partial V(\varphi)}{\partial\varphi} = 0. \tag{107}$$

Differentiating the potential

$$\frac{\partial V(\varphi)}{\partial \varphi} = \frac{\partial}{\partial \varphi}\Big(\frac{\lambda_\varphi}{8}(|\varphi|^2 - f_a^2)^2 + \chi(T)\Big(1 - \frac{\mathrm{Re}(\varphi)}{f_a}\Big)\Big), \tag{108}$$

$$= \frac{\lambda_\varphi}{4}\varphi(|\varphi|^2 - f_a^2) + \chi(T)\sin(\theta). \tag{109}$$

We can therefore write the full equation

$$\ddot{\varphi} + 3H\dot{\varphi} - \frac{1}{a^2(t)}\nabla^2\varphi - \frac{\lambda_\varphi}{4}\varphi(|\varphi|^2 - f_a^2) - \chi(T)\sin(\theta) = 0. \tag{110}$$

This equation of motion can be solved numerically to calculate the evolution of the axion field including topological defects such as strings and domain walls.

We can estimate the characteristic mass of axion miniclusters by calculating the total mass in axions contained within the horizon of the universe when the axion field first began to oscillate at $T_1 \approx 1$ GeV. This point is given by

$$AH(T_1) \approx m_a(T_1). \tag{111}$$

where A is a somewhat arbitrarily factor normally chosen to be 1 or 3. We have seen already that the temperature dependence of the axion mass arises due to the susceptibility of the topological charge $\chi(T)$. From Fig. 12 we see that at early times (large temperatures) $\chi(T)$ can be approximated at a single power-law $\chi(T) \propto T^{-8.2}$.

The radius of the horizon at T_1 is given by

$$L_1 = \frac{1}{a_1 H(T_1)} \tag{112}$$

From this, the characteristic minicluster mass can be estimated using

$$M_{\rm MC} = \bar{\rho}_a(T_1) V_{\rm H} L_1^3, \tag{113}$$

where the value $V_{\rm H}$ varies between different definitions of the Hubble volume, with the definition of Ref. [66] corresponding to $V_{\rm H} = 1$[10]. The result is well fit by

$$M_{\rm MC} = 7.36 \times 10^{-12}\Big(\frac{T_1}{\rm GeV}\Big)^{-3}\mathcal{S}\left(\log_{10}\frac{T_1}{\rm GeV}\right) V_{\rm H} M_\odot, \tag{114}$$

where $\mathcal{S}(x)$, given by

$$\mathcal{S}(x) \equiv 0.5[1 + \tanh 4(x + 0.8)] + 1.3[1 + \tanh 4(-0.8 - x)], \tag{115}$$

[10] Some, e.g. Refs. [79, 133] use a larger value $V_{\rm H} \approx 130$.

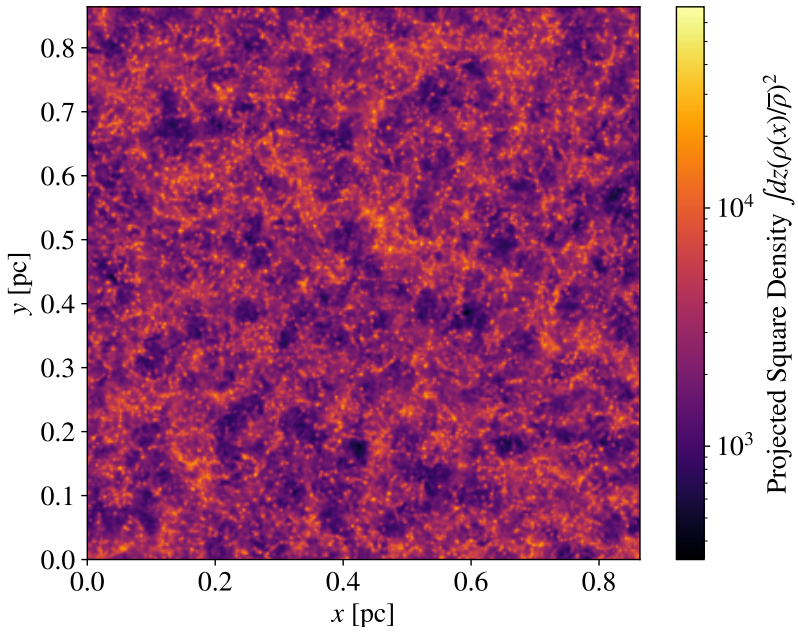

FIG. 15. *Projected Square Density of Axion DM Initial Conditions.* Field at $z = 10^6$, calculated using field theory simulations from Ref. [55]. The scale of the projected densities is set by the average square density along the line of sight.

is a fitting function that enforces the effect of the QCD phase transition impact on $g_*(T)$.

In this work, we make use of initial conditions taken from recent field theory simulations of Ref. [55]. These simulations evolve the PQ field through the QCD phase transition, using the Press-Ryden-Spergel method [134, 135]. They include the formation of axion strings and $N = 1$ domain walls.

These defects decay when the axion field begins to oscillate. At this point, the radial field is at the vacuum expectation value everywhere and therefore no longer needs to be simulated. The resulting distribution of the axion field at $z \approx 10^6$, shown in Fig. 15, is then found by performing a WKB approximation to evolve the axion field through its final oscillations. The projected square density allows us to see the large density perturbations throughout the entire box. These are the seeds of axion miniclusters. The power spectrum $P(k)$, where k is Fourier conjugate to x, of this field, linearly evolved to $z = 0$, is shown in Fig. 16.

The simulations are performed in code units that absorb the axion mass. This allows us to rescale the results to any axion mass. The characteristic time scale is defined as using

$H(T_1) = m_a(T_1)$ $(A = 1)$. The horizon size at this time, given by Eq. 112, is used to define a characteristic length scale given by

$$L_1 = 0.0362\left(\frac{50\mu\text{eV}}{m_a}\right)^{0.167}\text{pc}. \tag{116}$$

where the exponent of 0.167, valid in the 1 to 2 GeV temperature range of interest, is found by fitting using $\chi(T)$ [102, 130]. The total box size is then given by $L_{\text{box}} = L_{\text{adm}}L_1$ where L_{adm} is an integer which dictates the specific size of the box. In our case $L_{\text{adm}} = 24$ giving a comoving box length of 0.864 pc.[11]

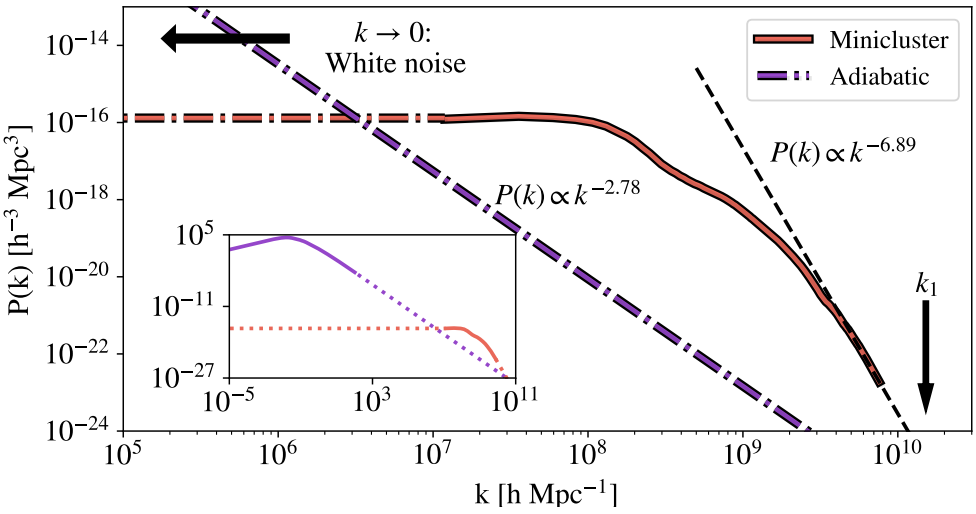

FIG. 16. *Power Spectrum of Initial Conditions.* Data from Ref. [55]. The extrapolated adiabatic power spectrum (purple dot-dashed) is included for comparison. The adiabatic power will also be cut-off below $k_1 = 2\pi/L_1$, since this is the axion Jeans scale. The inset graph shows the full extent of these two power spectra as well as the points at which their extrapolated curves meet. The adiabatic power spectrum is computed with CAMB and extrapolated with the given power law to large k [136].

3. Constraints

Since the axion mass is so small, it is not possible to detect them through recoil experiments as done for the WIMP. Instead, there are three main types of classes of experiments

[11] This box is somewhat larger than those studied originally in Ref. [55], and were provided to us privately. They are the same as used in the N-Body simulations of Ref. [87].

used to constrain the axion parameter space: Haloscopes, helioscopes and 'Light Shining through a Wall' (LSW) experiments [31, 137]. There are also strong constraints placed on the axion by astrophysical considerations.

Although there have been significant efforts to constrain the axions couplings to other SM particles [138], most tend to focus on the coupling with photons.

This coupling arises from the following term in the axion Lagrangian

$$\mathcal{L} \supset -\frac{1}{4}\phi g F_{\mu\nu}\tilde{F}^{\mu\nu} \tag{117}$$

where ϕ is the axion field, g is the coupling constant and where F and $\tilde{F}^{\mu\nu}$ are the electromagnetic field tensor and its dual respectively.

This term is made up of two components. The first, $\mathcal{L} \propto \phi\epsilon F_{\mu\nu}\tilde{F}^{\mu\nu}$, where ϵ is the electromagnetic anomaly, arises automatically for all axion-like-particles (ALPs). The second, $\mathcal{L} \propto \phi\mathcal{C} F_{\mu\nu}\tilde{F}^{\mu\nu}$, where $\mathcal{C}$ is the colour anomaly, is mediated by gluons and is required in order for the axion to solve the strong CP problem.

The total coupling constant is given by

$$g = \frac{\alpha}{2\pi f_a}\left[\epsilon - \mathcal{C}\frac{2}{3}\frac{4 + m_u/m_d}{1 + m_u/m_d}\right]. \tag{118}$$

where m_u and m_d are the masses of the up and down quark respectively [139]. We also know, from Eq. 78, that the QCD axion mass is dependent on the colour anomaly . We can therefore write the coupling constant between the QCD axion and photons as

$$g_{\text{QCD}} = 10^{-15}\left(\frac{m_a}{5 \times 10^{-6}\text{eV}}\right)\text{GeV}^{-1}\mathcal{C}_{\phi\gamma} \tag{119}$$

where $\mathcal{C}_{\phi\gamma}$ is an $\mathcal{O}(1)$ factor which depends on the specific axion model. For the two most popular axion models, the KSVZ and DFSZ models, this factor is given by $\mathcal{C}_{\phi\gamma} = -1.92$, 0.75 respectively [140–143]. The region of parameter space between these two models defines the region we normally think of as the QCD axion.[12]

The presence of this coupling modifies the classical Maxwell equations of electromagnetism. We find that the axion field behaves as a source of charge and current density. As a result, in the presence of a magnetic field, axions can be converted into photons and, equally, photons can be converted into axions. Experiments built to find the axion, therefore, attempt to detect these additional photons which would not be produced from the unmodified Maxwell equations alone.

[12] A wider distribution of $\epsilon/\mathcal{C}$ is also possible if we allow for the addition of more than one heavy, exotic quarks [144].

a. Haloscopes: If all of the dark matter is composed axions then we know that there is an average local density $\rho_a \approx 0.4$ GeV cm^{-3} with a dispersion $\sigma_v \approx 300$ km s^{-1} [104]. If the axion DM distribution is smooth (pre-inflationary scenario) then there will be a large flux of axions constantly passing through the Earth. Due to Eq. 117, in the presence of a strong magnetic field, these axions can be converted into photons which can then be detected. To date, the leading haloscope experiment is the Axion Dark Matter eXperiment (ADMX) [145]. Like many similar experiments, ADMX uses a tunable cavity to promote a resonant conversion of axions into photons increasing their sensitivity to a very narrow range of axion masses. As shown in Fig. 18, ADMX is the only haloscope to constrain the QCD axion. However, new experiments such as ALPHA, MADMAX, ORGAN, TOORAD as well as expansions by ADMX hope to constrain the axion-photon coupling for a range of axion masses [73, 146–149].

b. Helioscopes: It is also expected that axions should be produced in the Sun [150]. Helioscope experiments, therefore, attempt to detect these axions by aiming a dipole magnet towards the Sun to try to convert these axions into photons to be detected. Unlike cavity experiments, helioscopes are broadband experiments meaning they can constrain wide ranges of axion masses simultaneously. To date, the most sensitive helioscope is the CERN Axion Solar Telescope (CAST) collaboration shown in Fig. 18 [151]. The constraints by CAST will be surpassed by a range of International AXion Observatory (IAXO) experiments [152]. One advantage of helioscope experiments such as these is that, since they do not try to detect axion DM, their ability to detect the axion is independent of the total axion DM abundance or its distribution in the local area.

c. Light Shining through a Wall: For both haloscope and helioscope experiments, we have to assume the presence of some source of axions (or ALPs), either from the Sun or as background DM. LSW experiments, however, do not suffer from this problem. In these experiments, a laser beam is directed at a *classically* opaque wall in the presence of a strong magnetic field. However, due to Eq. 117 and its resultant modifications of Maxwell's equations, there is a small probability that some photons will convert into axions and pass through the wall. After passing through the wall, some of these axions may then be converted back to photons which can then be detected. Currently, the best limits produced by an LSW experiment set by the Any Light Particle Search (ALPS), do not exceed existing constraints from CAST [153]. However, these constraints will be greatly improved by its successor,

ALPS-II [154].

The most restrictive constraints on the axion-photon coupling come from astrophysical constraints. As mentioned previously, we expect that axions should be produced in stars. This gives stars another channel through which they can lose energy. Therefore, the existence of axions can alter a star's evolution. In particular, axion emission would alter the observed ratio of horizontal branch (HB) stars to red giant stars $R_{\rm HB}$ in globular clusters.

The impact of this axion-photon coupling has to be calculated numerically, however, these results are well described by the relation

$$R_{\rm HB} = 6.26Y - 0.41g_{10}^2 - 0.12 \tag{120}$$

where $Y_{\rm He}$ is the Helium abundance, $g_{10} \equiv g_{\phi\gamma}/10^{-10}$ GeV^{-1}. The Helium abundance and R-parameter are measured to be $Y_{\rm obs} = 0.2535 \pm 0.0036$ and $R_{\rm obs} = 1.39 \pm 0.04$ respectively [155].

As shown in Fig. 17, this gives us a preferred value for the coupling constant at $g_{\phi\gamma,{\rm HB}} = 4.3^{+1.3}_{-1.9} \times 10^{-11}$GeV. For $C_{a\gamma} = \mathcal{O}(1)$ this relates to an axion mass of $m_a = 0.2$ eV [155]. However, as we see from Fig. 17, while the observed helium value favours a non-zero coupling, is not far from being consistent with a coupling equal to zero. Therefore, this is often taken to be an upper limit on $g_{\phi\gamma}$.

We can also derive an upper limit on the QCD axion mass from the end of a star's life. Supernova 1987A (SN1987A) was observed in great detail as it occurred relatively close to Earth. This meant that, unlike other SN events, the neutrino burst was also observed by a number of detectors. Importantly, they found that the neutrinos arrived after the peak in the light from the SN. It is thought that this is because the star collapse creates a proto-neutron star which gravitationally traps the neutrinos, delaying their emission.

If axions couple to nucleons N then they are also produced in SN events via the process $N + N \longrightarrow N + N + a$. The production of these axions would cause the proto-neutron star to cool quicker than it otherwise would. This would mean that fewer neutrinos would be produced, shortening the observed length of the neutrino burst. This observation, therefore, provides a constraint on the axion-nucleon coupling and hence on the QCD axion mass. The resulting upper limit is $m_{\rm QCD} \lesssim 5 \times 10^{-2}$ eV [156].

Another key astronomical constraint on all ALPs comes from the observation of spinning black holes. The existence of ALPs can lead to a process known as black hole superradiance.

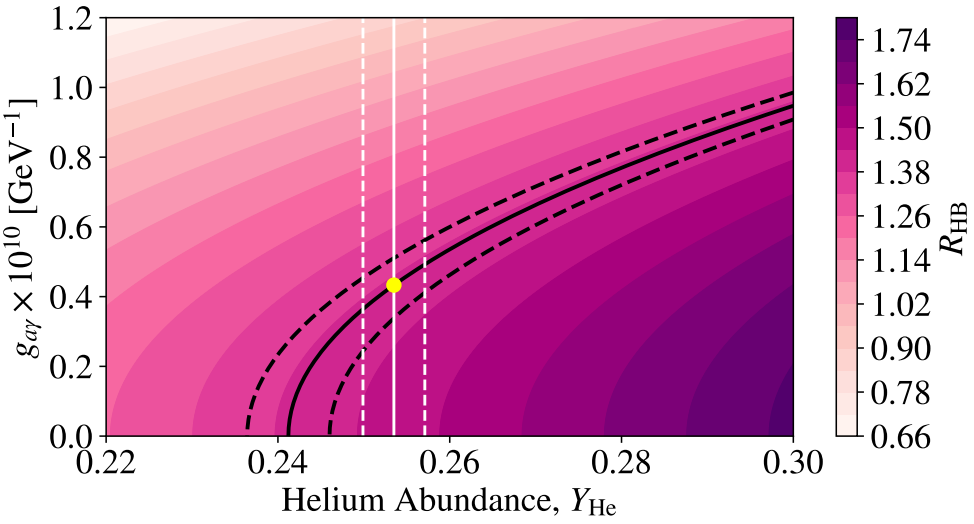

FIG. 17. *Horizontal branch star ratio.* HB ratio calculated from empirical formula given by Eq. 120 as function of helium abundance and axion-photon coupling. Black solid and dashed lines indicate the contour for which $R_{\rm HB}$ equals the observed value and it's 68% confidence intervals. Similarly, white solid and dashed lines indicate the observed value for $Y_{\rm He}$ and it's 68% confidence intervals. Reproduced from Ref. [155].

This causes the black holes to lose their spin over time. There are two classes of black hole that we have observed: stellar black holes which ($1M_\odot \lesssim M_{\rm BH} \lesssim 100M_\odot$) and supermassive black holes ($10^6 M_\odot \lesssim M_{\rm BH} < 10^9 M_\odot$). These relate to constraints on the axion mass in the regions $4 \times 10^{-12} \lesssim m_a \lesssim 2 \times 10^{-11}$ eV and $10^{-19} \lesssim m_a \lesssim 10^{-16}$ eV respectively [49]. This provides us with what is often considered a lower limit on the QCD axion mass: $m_{\rm QCD} \lesssim 2 \times 10^{-11}$ eV.

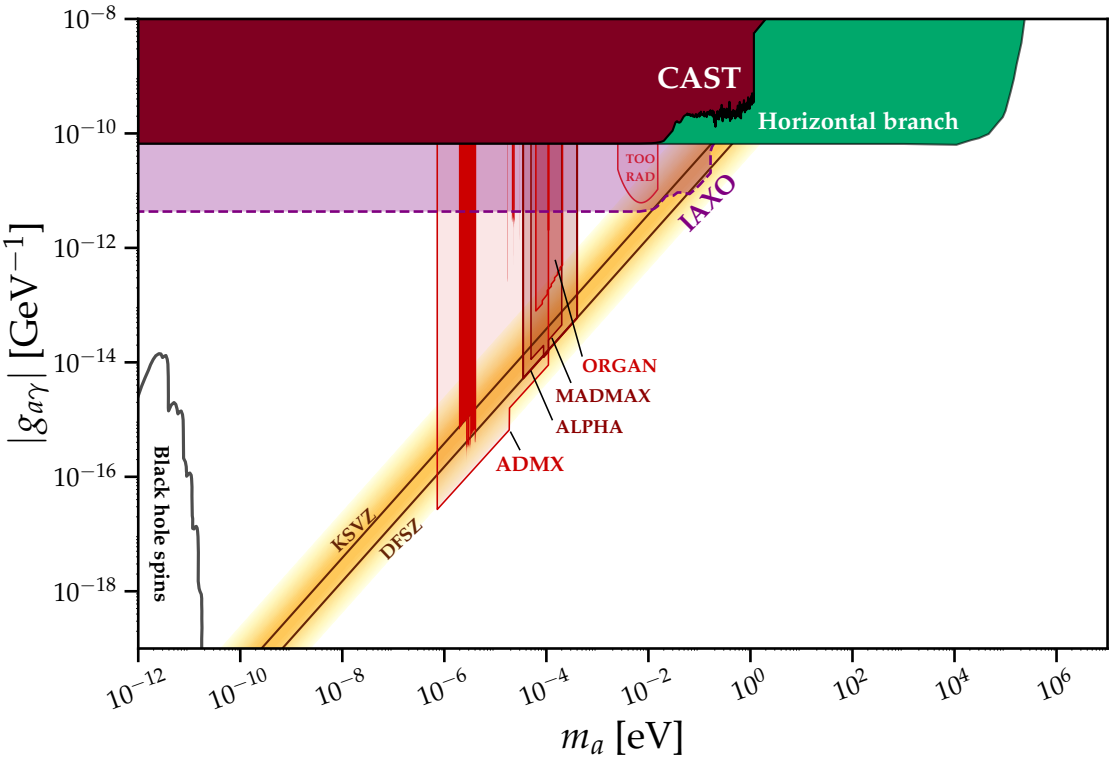

FIG. 18. *Sample of constraints on axion-photon coupling.* Including constraints from existing and upcoming haloscopes [73, 146–149], helioscopes CAST and IAXO [151, 152], horizontal branch stars [155] and BH superradiance [157]. Graph produced using AxionLimits code written by Ciaran O'Hare.

IV. MODELS FOR GRAVITATIONAL COLLAPSE

A. Spherical Collapse

As done in Ref. [67], we consider a spherical matter overdensity of radius r in a universe containing only matter and radiation. Much of this comes directly from the section of the same title that I wrote in Ref. [88]. The equation of motion for such a region can be written as

$$\ddot{r} = -\frac{8\pi G}{3}\rho_r - \frac{GM_{\rm TOT}}{r^2}, \tag{121}$$

where ρ_r is the homogeneous radiation density and $M_{\rm TOT}$ is the mass enclosed by the radius. We consider a comoving reference frame $r = a(\eta)R_\xi(\eta)\xi$ where R is the deviation from the Hubble flow and ξ is a label for the comoving shell. Then, in a flat $\Omega_0 = 1$ universe containing only radiation and pressureless matter it can be shown the equation of motion

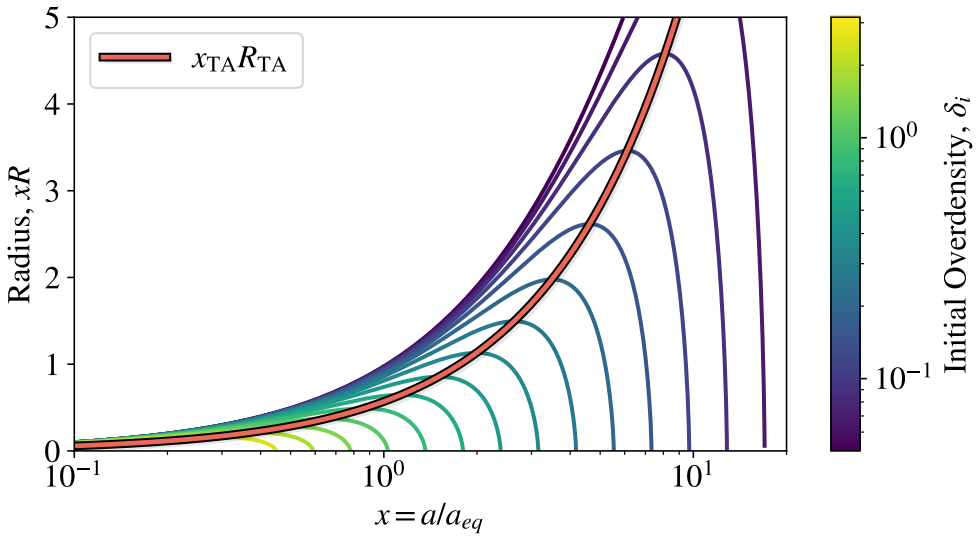

FIG. 19. *Spherical collapse during radiation domination.* Dimensionless radius of an overdensities of initial size δ_i. Orange line indicates the the point of turn-around radius as a function of this initial overdensity. The code used to calculate this can be found on my GitHub page here: https://github.com/David-Ellis/thesis-code/tree/main/KTode.

can be rewritten as

$$x(1+x)\frac{\mathrm{d}^2R}{\mathrm{d}x^2} + \left(1+\frac{3}{2}x\right) + \frac{1}{2}\left(\frac{1+\delta_{\rm i}}{R^2} - R\right) = 0, \tag{122}$$

where $x = a/a_{eq}$ is the normalised scale factor and $\delta_{\rm i} = \frac{\rho-\bar{\rho}}{\bar{\rho}}$ is the clump overdensity [67]. This can then be solved numerically, assuming $R_i = 1$ and $\left.\frac{dR}{dx}\right|_i = 0$.

The density of the matter perturbation at turn-around is given by

$$\langle\rho_{\rm TA}\rangle = \frac{1}{4\pi r^2}\frac{\mathrm{d}M}{\mathrm{d}r}. \tag{123}$$

We, therefore, represent the parameters at turn-around using

$$x_{\rm TA} = \frac{C_x}{\delta_{\rm i}}, \tag{124}$$

and

$$\langle\rho_{\rm TA}\rangle = C_\rho\rho_{eq}\frac{\delta_{\rm i}^3}{3\xi^2}\frac{d}{d\xi}(1+\delta_{\rm i})\xi^3, \tag{125}$$

where $C_\rho = 1/(R_{\rm TA}C_x)^3$ depends only weakly on δ_i. From the virial theorem, we can approximate that the virial radius is half the turn around radius. Therefore, for the core density $\delta_{\rm i,0} = \delta_{\rm i}(r=0)$ we have

$$\langle\rho_{\rm F}\rangle = 8C_\rho\rho_{\rm eq}\delta_{\rm i,0}^3(1+\delta_{\rm i,0}). \tag{126}$$

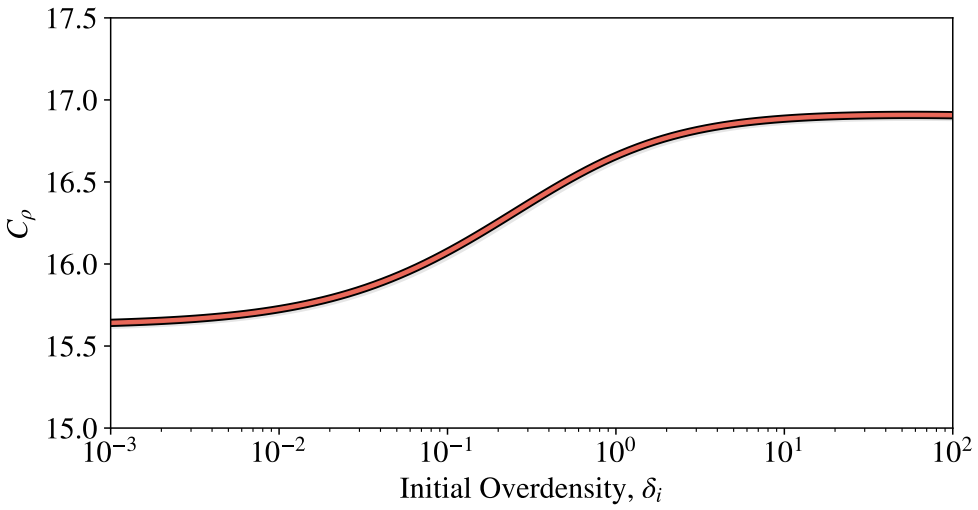

FIG. 20. *Spherical collapse turn-around parameter.* The code used to calculate this can be found on my GitHub page here: https://github.com/David-Ellis/thesis-code/tree/main/KTode

Therefore, by numerically solving the collapse of R we can calculate C_ρ and hence estimate the final density. We will see that, for large overdensities (large $\delta_{\rm i}$), the final overdensity is strongly sensitive to the redshift at which we consider the object to first start collapsing.

We have confirmed, as found in Ref. [67], that C_ρ depends only very weakly on $\delta_{\rm i,0}$ with a value of $C_\rho \sim 17$ thus giving

$$\langle \rho_{\rm F} \rangle = 136 \rho_{\rm eq} \delta_{\rm i,0}^3 (1 + \delta_{\rm i,0}). \tag{127}$$

B. Linear Perturbation Theory

Considering small perturbations in an expanding homogeneous and isotropic universe the equation of motion describing the linear growth of matter perturbations is given by

$$\frac{{\rm d}^2\delta}{{\rm d}t^2} + 2H\frac{{\rm d}\delta}{{\rm d}t} - \frac{c_s^2}{a^2}\Delta\delta - 4\pi G\epsilon_0\delta = 0, \tag{128}$$

where c_s is the speed of sound. For cold matter in the presence of radiation or dark energy, we can neglect the c_s^2 term since the pressure is negligible. It can then be shown that the equation of motion can be written as

$$x^2(1 + x^{-3w})\frac{{\rm d}^2\delta}{{\rm d}x^2} + \frac{3}{2}x(1 + (1-w)x^{-3w})\frac{{\rm d}\delta}{{\rm d}x} - \frac{3}{2}\delta = 0, \tag{129}$$

where w is the equation of state for the homogeneous relativistic background energy with x defined as before [100]. Hence, for dark matter in the presence of a radiation background

$$x(x+1)\frac{\mathrm{d}^2\delta}{\mathrm{d}x^2} + (1+\frac{3}{2}x)\frac{\mathrm{d}\delta}{\mathrm{d}x} - \frac{3}{2}\delta = 0. \tag{130}$$

This is known as the Meszaros equation, and is equivalent to Eq. 122 considering $R \equiv 1-\delta$ in the limit $\delta \ll 1$. For the case of interest, $w = 1/3$, the general solution is

$$\delta(x) = C_1\Big(1+\frac{3}{2}x\Big) + C_2\Big[\Big(1+\frac{3}{2}x\Big)\ln\frac{\sqrt{1+x}+1}{\sqrt{1+x}-1} - 3\sqrt{1+x}\Big], \tag{131}$$

where C_1 and C_2 are constants that are fixed by the initial conditions.

Since axion minicluster seeds are isocurvature perturbations, we consider a single isocurvature mode in the sub-horizon limit. The initial conditions are determined by

$$\delta(t=0) = 1, \tag{132}$$

$$\frac{d\delta}{dt}\Big|_{t=0} = 0. \tag{133}$$

However, since

$$\frac{d\delta}{dt} = \frac{d\delta}{dx}H(x)x = \frac{d\delta}{dx}\dot{x}, \tag{134}$$

and $H(x)$ and x are both nonzero, so we require

$$\frac{d\delta}{dx} = 0. \tag{135}$$

In the limit of small x

$$\delta(x) = (C_1 - 3C_2) - C_2\ln\Big(\frac{x}{4}\Big) + \mathcal{O}(x), \tag{136}$$

therefore $C_1 = \delta_i$, $C_2 = 0$ [100]. This allows us to write the growth factor simply as

$$D(x) = 1 + \frac{3}{2}x. \tag{137}$$

By calculating the linear overdensity at the time of collapse, as calculated using the non-linear equation of motion, we can calculate the size of regions that should collapse as a function of redshift.

Solving Eq 122 numerically we find, similarly to the turnaround parameter of Ref. [67], the collapse parameter $C_{\mathrm{col}}(\delta_i) \equiv \delta_i x_{\mathrm{col}}(\delta_i)$ is approximately constant as a function of the initial overdensity. We can therefore expect an overdensity to collapse once it has grown by some fixed amount $\delta_{\mathrm{c}}(\delta_i) = \delta_i + \varepsilon$.

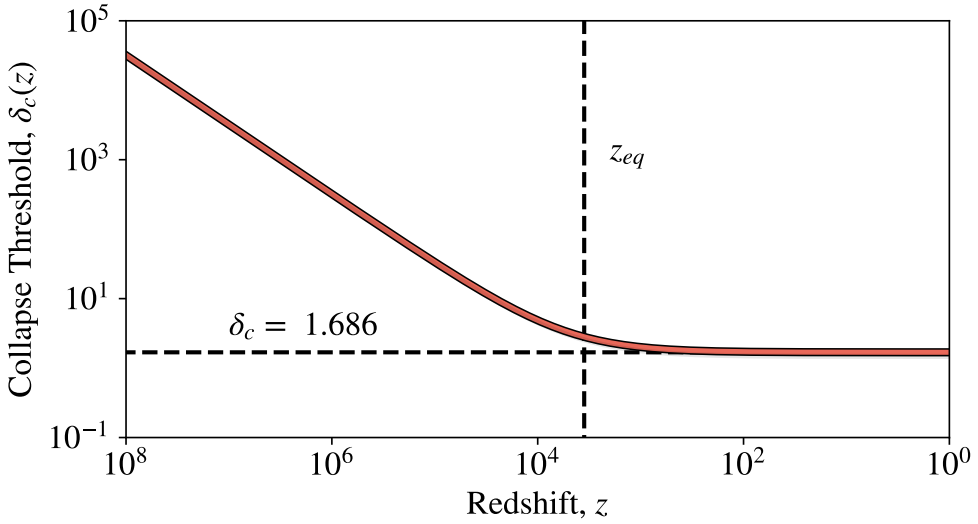

FIG. 21. *Modified critical overdensity.* Calculated by solving the spherical collapse as given by Eq. 122 to determine the point of non-linear collapse and relating this to density from linear growth using Eq. 137. Performing a least-squares fit, we find that The collapse threshold saturates to the Einstein-de Sitter value 1.686 at late times, and is larger during the radiation era.

To ensure that the δ_i dependence of $C_{\rm col}$ is correctly dealt with, we fit ε to our numerical solution using a least-squares fit and find the textbook value from spherical collapse in the matter dominated era, which can be found analytically and is given by $\varepsilon = 1.686$ [92].

Then, since $\delta_i = \delta_c(x)/D(x)$ the critical density can be calculated as a function of redshift. Hence, the critical overdensity above which structures will collapse at some redshift z is then given by

$$\delta_{\rm c}(x) = \frac{\varepsilon D(x)}{D(x) - 1}. \tag{138}$$

From Fig. 21 we see that prior to matter-radiation equality, overdensities need to be very large in order to collapse. We will see later that this is the case for the seeds of axion miniclusters. Ordinary WIMP CDM, in contrast, is sourced by adiabatic perturbations that are normalised to CMB. When this power spectrum is extrapolated to high k, we find that δ is small and therefore objects composed of CDM can only collapse after matter-radiation equality.

C. Press-Schechter

From the spherical collapse model, we expect that regions of a linearly evolved overdensity field above the critical overdensity will have collapsed to form virialised objects. This can be written as the criteria that $\delta(\mathbf{x}, t) > \delta_c(z)$. To assign masses to these regions, we consider a smoothed density field given by

$$\delta_s(\mathbf{x}; R) \equiv \int \delta(\mathbf{x}')W(\mathbf{x} + \mathbf{x}'; R)\mathrm{d}^3\mathbf{x}', \tag{139}$$

where $W(\mathbf{x}; R)$ is a window function of characteristic radius R. For the simplest case of a spherical tophat filter, this is related to a mass $M = \frac{4}{3}\pi\bar{\rho}R^3$. The Press-Schechter (PS) formalism works by assuming that the probability of $\delta_s > \delta_c(t)$ is equal to the fraction of mass contained within halos of mass greater than M [158]. Assuming a Gaussian density field (we address non-Gaussianities shortly), this probability is found to be

$$\mathscr{P}[> \delta_c(t)] = \frac{1}{2}\mathrm{erfc}\Big[\frac{\delta_c(t)}{\sqrt{2}\sigma(M)}\Big], \tag{140}$$

in which $\sigma(M)$ is the mass variance of the smoothed density field given by

$$\sigma^2(M) = \langle\delta_s^2(\mathbf{x}; R)\rangle = \frac{1}{2\pi^2}\int_0^\infty P(k)\tilde{W}^2(\mathbf{k}R)k^2\mathrm{d}k, \tag{141}$$

where $P(k)$ is the power spectrum of the density perturbations and $\tilde{W}(\mathbf{k}R)$ is the window function in Fourier space. For a tophat filter, the window function is given by

$$\tilde{W}_{\mathrm{th}}(\mathbf{k}R) = \frac{3(\sin kR - kR\cos kR)}{(kR)^3}. \tag{142}$$

However, underdense regions can be enclosed within a larger overdense region causing them to be included in the larger collapsed object. This cloud-in-cloud problem is accounted for by introducing a famous 'fudge factor' of 2 [159]. This modifies the original ansatz to give the following

$$F(> M) = 2\mathscr{P}[> \delta_c(t)]. \tag{143}$$

From this, this halo mass function (HMF) can be estimated by

$$\frac{\mathrm{d}n}{\mathrm{d}\ln M} = M\frac{\rho_0}{M^2}f(\sigma)\Big|\frac{\mathrm{d}\sigma}{\mathrm{d}\ln M}\Big|, \tag{144}$$

where ρ_0 is the mean DM density and $f(\sigma)$ is the multiplicity function.

In standard PS, this multiplicity function is given by

$$f_{\rm PS}(\sigma) = \sqrt{\frac{2}{\pi}}\frac{\delta_c}{\sigma}\exp\left(\frac{-\delta_c^2}{2\sigma^2}\right) \tag{145}$$

where δ_c is the critical overdensity. As discussed, for ordinary WIMP CDM $\delta_c \approx 1.686$, however we replace this with our redshift dependent threshold $\delta_c = \delta_c(z)$. There exist, however, other multiplicity functions which are often found to better match simulation data than PS [160]. One of the most popular alternatives is the Sheth-Tormen fit

$$f_{\rm ST}(\sigma) = A\sqrt{\frac{2a}{\pi}}\left[1+\left(\frac{\sigma^2}{a\delta_c^2}\right)^p\right]\frac{\delta_c}{\sigma}\exp\left(\frac{-a\delta_c^2}{2\sigma^2}\right), \tag{146}$$

where $A = 0.3222$, $a = 0.707$ and $p = 0.3$ [161].

Applying the outlined formalism on the power spectrum of the initial conditions, using one of the fitting functions above, we can estimate the HMF as a function of redshift assuming a Gaussian overdensity field[13].

D. N-body simulations

As well as these analytical and semi-analytical approaches, we can study the formation of non-linear structure formation using fully numerical simulations. These simulations can be largely grouped into two categories: N-body simulations and Schrödinger-Poisson (SP) solvers. Although, as discussed later in Sec. V C, SP are of central importance to the study of axion stars (See Ref. [162] for review), in this work we only make direct use of results from the N-body simulations. We will therefore limit our discussion to this class of simulations.

Consider a system of N particles of equal mass $m = 1$ with positions and velocities $(\mathbf{r}_i, \mathbf{u}_i)$ where $i = 1, 2, ..., N$. The velocity and acceleration of these particles is then given by

$$\frac{{\rm d}\mathbf{r}_i}{{\rm d}t} = \mathbf{u}_i, \tag{147}$$

and

$$\frac{{\rm d}\mathbf{u}_i}{{\rm d}t} = -\nabla\phi|_i, \tag{148}$$

respectively where ϕ is the gravitational potential experienced. This potential is given by the mass density ρ via the Poisson equation

$$\nabla^2\phi = 4\pi G\rho(\mathbf{r}, t). \tag{149}$$

[13] The code for this can be found on my GitHub account here: https://github.com/David-Ellis/ps-toolkit.

In cosmological simulations, the background space is uniformly expanding. Therefore, it is convenient to choose coordinates that expand with the background. The comoving positions and velocities are given by

$$\mathbf{x}_i = \mathbf{r}_i/a, \tag{150}$$

and

$$\mathbf{v}_i = \frac{\mathrm{d}\mathbf{x}_i}{\mathrm{d}t}, \tag{151}$$

respectively where a is the scale factor. The comoving acceleration is given by

$$\frac{\mathrm{d}\mathbf{v}_i}{\mathrm{d}t} + 2H(t)\mathbf{v}_i = -\frac{1}{a^2}\nabla_x\Phi|_x, \tag{152}$$

where $H(t) = \dot{a}/a$ is the Hubble parameter and Φ is the gravitational potential due to density *perturbations* given by

$$\nabla_x\Phi|_x = 4\pi G a^2 \left[\rho(\mathbf{x}, t) - \bar{\rho}(t)\right], \tag{153}$$

where $\bar{\rho}(t)$ is the average background density [92].

While the exact approach may vary, the evolution of a system of particles is simulated by:

1. calculate the gravitation field based on the positions of the particles at some time t_n

2. hence calculate the new speeds and position of each particle:

$$v_i(t_n) = v_i(t_{n-1}) + \frac{\mathrm{d}v_i}{\mathrm{d}t}\Delta t, \tag{154}$$

$$x_i(t_n) = x_i(t_{n-1}) + v_i(t_n)\Delta t. \tag{155}$$

3. recalculate the gravitation force due to the particles at their new positions.

Typically, to improve the precision and stability of the solution, an additional half-step is added such that the acceleration on each particle is calculated from their intermediate positions at $t_{n+1/2}$ instead of their initial position at t_n. This is known as the "leap-frog scheme" [92].

The simplest way to calculate the motion of the particles is to directly sum the gravitation force between each pair of particles as given by

$$F_i = \sum_{j \neq i} Gm \frac{r_i - r_j}{|r_i - r_j|^3}. \tag{156}$$

Since this does not introduce any approximations, using a direct sum offers the highest level of accuracy. However, it is also the most computationally expensive as $\mathcal{O}(N^2)$ operations need to be performed for each time-step [163].

One way of reducing the computation time is to use the tree code method. By subdividing the space into a hierarchy of cells, this method enables the force contribution of many distant particles to be approximated together. Doing so reduced the computation time to $\mathcal{O}(N \log N)$ [164]. This can be sped up further by considering the fact that the effect of distant particles will be very similar for all particles in a close group. By doing this, the Fast Multipole Method further reduces the calculation time to just $\mathcal{O}(N)$ [164]. Another method used to simplify and speed up the calculations is by using a particle-mesh (PM) algorithm. Here, instead of calculating the force directly between each pair of particles, the gravitational field is calculated by solving the Poisson equation for the mean density field.

Additionally, in order to avoid unphysical behaviour at small radii such as the formation of binary systems, N-body simulations typically employ a softening length below which the forces between particles are reduced.

In this work, we make us of N-body data produced by Ref. [87] in which they simulate the evolution of the initial field shown in Fig. 15 calculated in Ref. [55]. They performed their N-body simulations using Gadget-3, the precursor to the current version Gadget-4 [165]. This uses a hybrid PM-Tree approach.

They also use a softening length equal to one comoving astronomical unit (AU). As done in Ref. [87], we therefore take 4AU to be the limit of the spacial resolution of these simulations.

In these simulations, the Hubble parameter is given by

$$H(z) = H_0 \left[\Omega_{m0}(1+z)^3 + \Omega_{r0}(1+z)^4 + \Omega_{\Lambda 0}\right]^{1/2}, \tag{157}$$

with a standard ΛCDM cosmology ($\Omega_{m0} = 0.3$, $\Omega_{r0} == 8.48 \times 10^{-5}$ and $\Omega_{\Lambda 0} = 0.7$).

DM halos are located in the N-body data using the SUBFIND halo finder [166, 167]. This algorithm identifies the centres of halos as minima in the gravitational field. The virial radius is then determined by integrating outwards from this centre until the average internal density is given by $\Delta_{\rm vir}\rho_c$ where ρ_c is the critical density of the universe given by

$$\rho_c = \frac{3H^2(z)}{8\pi G}, \tag{158}$$

and $\Delta_{\rm vir}$ is the virial overdensity. Considering the spherical collapse of a perturbation in a universe composed of matter and dark energy, the virial overdensity can be approximated by

$$\Delta_{\rm vir} = 18\pi^2 + 82(\Omega_m(z) - 1) - 39(\Omega_m(z) - 1)^2, \tag{159}$$

with

$$\Omega_m(z) = \left(\frac{H_0}{H(z)}\right)^2 \Omega_{m0}(1+z)^3. \tag{160}$$

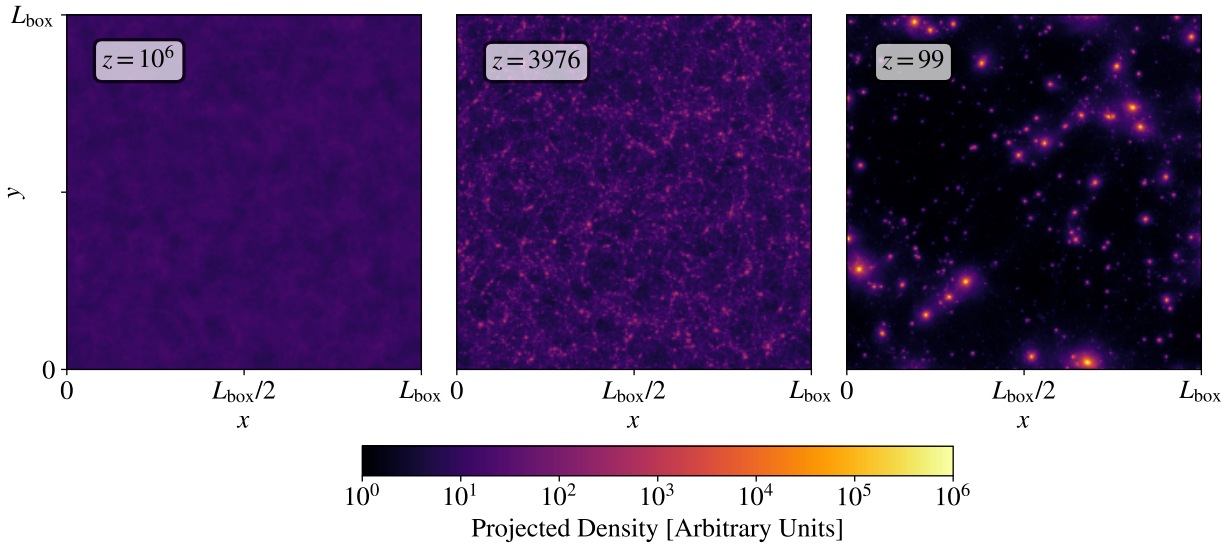

FIG. 22. *N-body Evolution.* Projected density of the the N-body distribution simulated by Ref. [87] from initial density field calculated by Ref. [55]

The evolution of the N-body field, shown in Fig. 22, is simulated until $z = 99$. After this redshift, it is expected that the box would soon go "non-linear" making the results unphysical. In Appendix. A, we show, by looking at the evolution of the matter-power spectrum at large scales, that this N-body simulation has begun to deviate from the linear prediction by $z = 99$. This is not expected to impact the N-body results significantly. However, as discussed in the next subsection, this has a more significant impact on the number of halos predicted using the Peak-Patch algorithm.

We can see clearly in Fig. 22 that there are two phases in the formation of axion miniclusters. Firstly, we see the initial large overdensities (miniclusters seeds) collapse and accrete matter from their local background. We see that, around matter-radiation equality, there are many small dense objects. After equality, the primary growth mechanism shifts to *hier-*

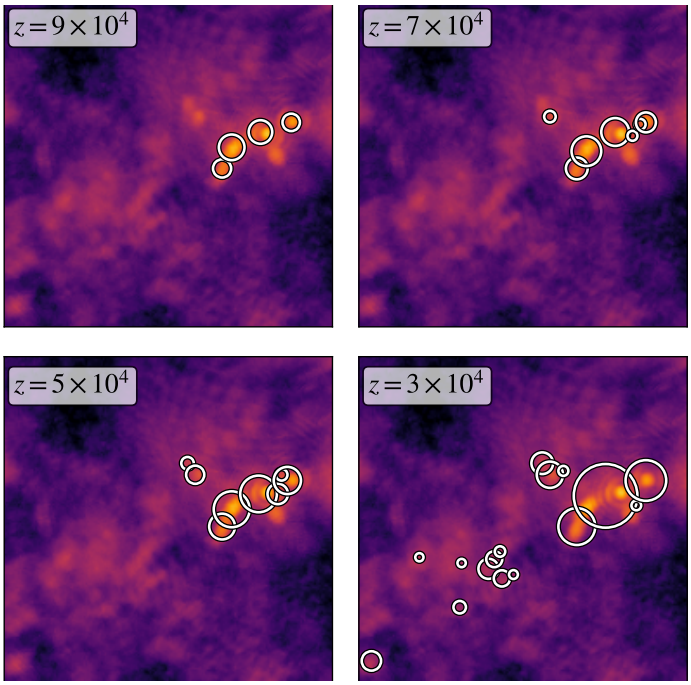

FIG. 23. *Evolution of DM Halos calculated by Peak Patch.* Calculated for a small section overlayed onto the initial density field. White circles indicate the radii of regions in which the contained overdensity is equal to the critical overdensity as shown in Fig. 21. The section shown is a few percent of the total box size. This figure and caption have been modified from Ref. [88]

archical structure formation as these collapsed seeds begin to merge together to form much bigger axion miniclusters seen in the right panel of Fig. 22.

E. The Peak-Patch Formalism

The following subsection has been taken from the section of the same title that I wrote for Ref. [88].

Typical full three-dimensional N-body dark matter simulations can be very computationally expensive. This expense is increased when simulating axion miniclusters since they begins to collapse deep into the epoch of radiation domination, thus requiring significantly longer simulation times. The mass-Peak Patch algorithm is an alternative to N-body simulations which is able to generally reproduce the same catalogue of halos using a fraction of the CPU time and memory. We use a modified version of this algorithm produced in [86].

Peak Patch is based on an extended Press-Schechter model in that it solves the excursion

set in real space on a true realisation of the density field. Excursion sets are regions in which the density field exceeds the threshold for collapse. However, while a region of unfiltered space might be below this threshold, the same region can be found to be over-dense when filtered (smoothed) on some scale. Therefore, we have to filter the density field on a hierarchy of scales R_f producing a four-dimensional field $F(\mathbf{r}, R_f)$. When this filtering is performed in Fourier space with a sharp k-filter and a Gaussian field, the excursion set can be solved analytically reproducing the Press-Schechter HMF without requiring the same fudge factor. However, when filtering in physical space, this can not be calculated analytically as it leads to a correlated random walk. Therefore, numerical methods such as this one must be employed [159].

The Peak Patch program utilises a massively-parallel procedure to identify peaks in a linearly evolved initial density field that has been smoothed on a range of scales. Once these peaks have been identified, a spherical integration is performed on the density field filtered on the largest scale at which the peak was found until the overdensity enclosed by the sphere is equal to the threshold overdensity at the redshift in question. This gives both the mass and the turn-around radius of the halos. The final sizes of the halos are calculated using the spherical collapse approximation. The final set of halos is then calculated by excluding overlapping patches. From this, the mass function can be calculated at each redshift. Additionally, the final locations of each peak are then calculated using first-order Lagrangian displacements. These displacements are estimated by performing an integral overdensity field in Fourier space [86].

In its unmodified form, Peak Patch identifies potential peaks as filtered cells containing an overdensity greater than the typical value of $\delta_{\rm crit} = 1.686$. The advantage for the present application is that, unlike PS, this method accounts correctly for all the non-Gaussianities in the initial distribution. A demonstration of the Peak Patch procedure is shown in Fig. 23. Here we plot the location and extent of halos calculated by Peak Patch at four different redshifts on top of the projected square density field for a small region of our box.

To use this formalism to simulate the collapse of axion miniclusters, two primary modifications have been made. Firstly, instead of using a random initial field, we input the realistic initial conditions calculated using field simulations by [55]. Secondly, we implement our redshift dependent threshold for collapse and growth factor from Eq. 138 and Eq. 137 respectively. Using this we can now calculate the final sizes, masses and positions of the DM

clumps originating from the realistic initial conditions.

Since the PP is so much faster than N-body simulations and its output file sizes are so much smaller, it can be used to make many snapshots over the evolution of a given initial density field. This makes PP very useful for producing merger trees.

We can build these merger trees by looking at the positions of halos at many time steps as shown in Fig.24. We start with a halo at some final redshift. In Lagrangian (undisplaced) coordinates, all progenitor halos at earlier redshifts must be contained within the radius of the final halo.

We start by using a series of k-dimensional trees (see Ref. [168]) to build up lists of halos that overlap with the final halo at each redshift. Then, to ensure that we do not count any matter which does not fall in the final halo, we consider only the mass contained within the overlapping region.

If two spheres with radii r_1 and r_2 spaced a distance d apart intersect then the volume of the intersection is given by

$$V_{\rm int} = \frac{\pi}{12d}(r_1 + r_2 - d)^2 \left(d^2 + 2^d(r_1 + r_2) - 3(r_1 - r_2)^2\right). \tag{161}$$

Then, assuming that the density of the overlapping region is uniformly distributed we take the progenitor mass to be

$$M_{\rm p} = \frac{V_{\rm int}}{V'} M' \tag{162}$$

where V' and M' are the volume and mass of the overlapping region respectively. Using this process we can very quickly build up merger trees for all halos in our data set with high temporal precision[14].

We use a total of 28 real space filters, logarithmically spaced from 1.77×10^{-3} pc to 0.229 pc to calculate the masses, sizes and positions of halos at 100 redshifts between $z = 10^6$ and $z = 99$. This final redshift was calculated in Ref. [87] to be safely before the box goes non-linear for our initial conditions. However, analysing the evolution of the power spectrum presented in Ref. [87], we have determined that the largest scales deviate from linear growth after $z = 629$. We, therefore, conclude that beyond this redshift their simulation enters the quasi-linear regime on the scale of the simulation box. The fact that the largest scales are no longer linear calls into question the accuracy of the N-body results for $z < 629$. In

[14] The code for this can be found on my GitHub account here: https://github.com/David-Ellis/m3p_merger.

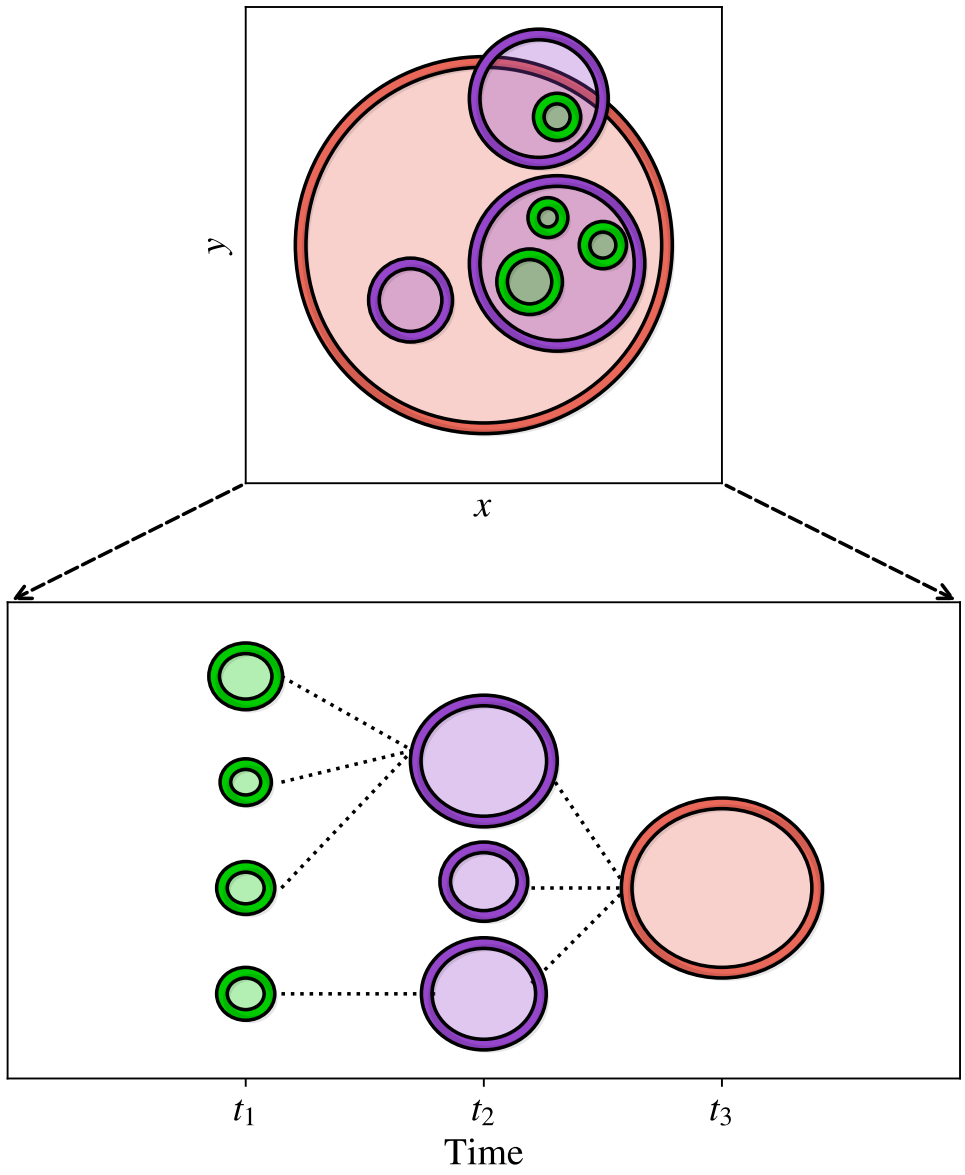

FIG. 24. *Building merger trees.* Sketch of the process of building merger trees. Top: Halo location and sizes in comoving Lagrangian coordinates in three different Peak Patch snapshots. Bottom: Merger tree built from Peak Patch data.

the quasi-linear regime, power is "moving" across scales, and on the largest scales, this is affected by the unphysical periodic boundary conditions.

Our results from Peak Patch depart significantly from the N-body results at $z < 629$. This is caused by the same scales experiencing different growth (Peak Patch only uses linear growth),[15] and results in a suppression in the number of low mass halos as a small number of

[15] If we artificially adopt the N-body quasi-linear growth at low redshift, this improves the agreement.

large halos come to dominate the total box size. We therefore conservatively only consider the HMF to a minimum redshift of $z = 629$, where the box scale is strictly linear.

However, while the halo number statistics are significantly affected for $z < 629$, the concentrations are affected less so. This is because, the $C(M)$ normalisation follows the growth factor, and the linear and quasi-linear growth only depart by $\mathcal{O}(10\%)$ even at $z = 99$. This can be understood by considering that the formation redshifts of surviving low mass halos (those not swallowed up by spurious large halos) are not affected; $C(M)$ is not a number statistic. Therefore, we still fit the concentrations of the halos by Peak Patch to those simulated by Ref. [87] at $z = 99$, this also being the only redshift at which such a comparison can be made. These results will be presented later in Sec. VII.

V. MINICLUSTER STRUCTURE

To date, there has been disagreement in the literature about what we should expect the radial density profiles of axion miniclusters to look like. The two most common suggestions are a single power-law profile and the familiar Navarro–Frenk–White (NFW) profile. The answer, we will see, is dependent on the miniclusters primary formation mechanism. Additionally, since axions are bosons, it is expected that they will form what are known as boson/axion stars in their centres.

In the next three subsections, we will explore the theory and existing simulation data regarding the main density profiles of axion miniclusters and their central boson stars. In Sec. V A, largely taken from the Sec. III D which I wrote for Ref. [88], we will explore the theory behind the NFW profile and how we can estimate a halo's concentration parameter. In Sec. V B, largely taken from the similarly titled section which I wrote for Ref. [91], we look at the analytical efforts made to predict the slope of a single power-law profile and the attempts to relate the scale density of a single power-law minicluster to its initial overdensity. Finally, in Sec. V C we introduce the axion star and derive the core-halo mass relation.

A. NFW Profile

We expect NFW profiles to form when objects form via *hierarchical structure formation*, that is, the merger of many smaller already collapsed objects [169]. Using the same initial density field as in this work, Ref. [87] showed that high-mass axion miniclusters have a radial density profile that is well described by the usual NFW profile

$$\rho(r) = \frac{\rho_c}{(r/r_s)(1 + r/r_s)^2}, \tag{163}$$

where ρ_c and r_c are the characteristic density and radius respectively. The concentration parameter is then defined by $c = r_{200}/r_s$ where r_{200} is the radius which encloses a region of mean density equal to $\rho_{200} = 200\rho_{\rm crit}$ [170].

Efforts have been made using N-Body simulations to relate the concentration parameter of a halo to its collapse redshift [169–172]. Navarro et. al defined the collapse redshift, sometimes also called the formation redshift, to be the redshift at which for some halo half of its final mass $M_{\rm final}$ is contained within progenitors of a mass larger than $fM_{\rm final}$ where f

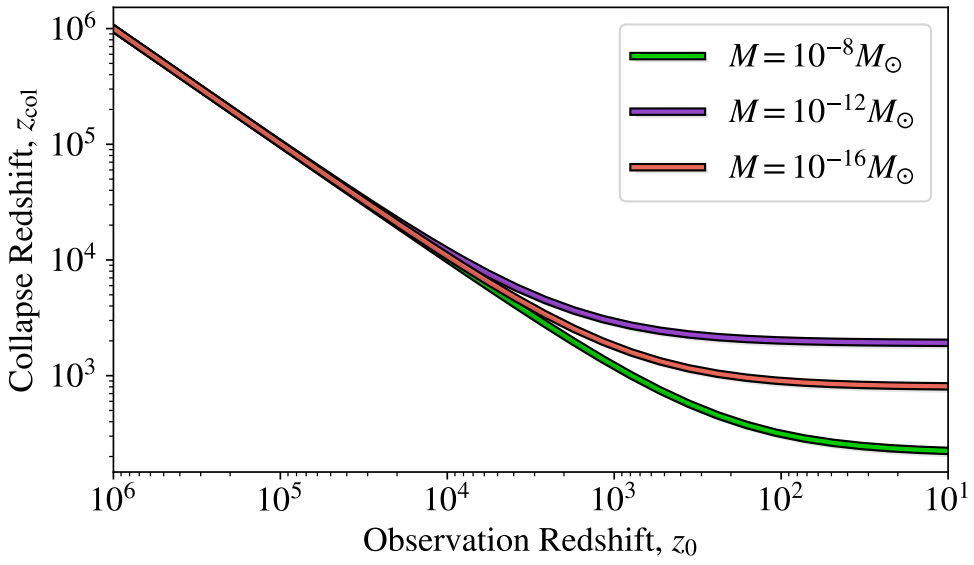

FIG. 25. *Collapse Redshift Evolution.* Calculated by solving Eq. 164 as a function of z_0 for a fixed mass with the minicluster power spectrum shown in Fig. 16.

is some fraction. This can be estimated using the Press-Schechter formalism

$$\mathrm{erfc}\big\{X(z_{\rm col}) - X(z_0)\big\} = \frac{1}{2}, \tag{164}$$

where

$$X(z) = \frac{\delta_c(z)}{\sqrt{2[\sigma^2(fM, z) - \sigma^2(M, z)]}}, \tag{165}$$

and $\sigma(M, z)$ is the linear variance of the power spectrum at some final redshift z [171]. Navarro et. al found that a fraction of $f = 0.01$ best matched the results from N-Body simulations of CDM with adiabatic initial conditions. We take f as a free normalisation constant in our application.

As shown in Fig. 25, if we solve Eq. 164 as a function of z_0 for a fixed mass using the mass variance for the power spectrum shown in Fig. 16, we find that the redshift at which a halo "collapses" is not fixed but instead evolves over time. We see that, for all masses, the collapse redshift initially falls proportional to z_0, then at $z_0 \sim z_{eq}$ the collapse redshift tends towards some constant value determined by the halo mass M.

Navarro et. al then assume that the scale density of the halo δ_s is proportional to the ratio of the density of the universe at this time to the density today. Thus implying

$$\delta_s(x, \kappa) = \kappa_{\rm NFW}(f)\frac{\rho_u(x_{\rm col})}{\rho_u(x)}, \tag{166}$$

where $\kappa_{\rm NFW}$ is a free parameter and $x_{\rm col}$ is the normalized scale factor relating to the point of collapse defined by Navarro et. al (not to be confused with the point of non-linear collapse from Sec IV B). Since the halos they considered only collapse at very late redshifts, only the matter component of the density was considered. However, since the halos we consider collapse much earlier, we must also acknowledge the contribution of radiation. Therefore, we take

$$\rho_u(x_{\rm col}) = \rho_{\rm eq}(x_{\rm col}^{-3} + {x_{\rm col}}^{-4}). \tag{167}$$

Having calculated the characteristic overdensity, the concentration parameter can then be calculated by solving

$$\delta_s = \frac{200}{3}\frac{c^3}{\ln(1+c) - c/(1+c)}. \tag{168}$$

Once the concentration parameter curve is calculated, the free parameter $\kappa_{\rm NFW}(f)$ can be fitted to results from N-Body simulations. In Fig. 26 we fit the predicted concentration parameter from the NFW formula with the power spectrum in Fig. 16 to the N-Body results from [87] and find $\kappa_{\rm NFW}(f = 0.01) = 1.28 \times 10^5$. We can then calculate the predicted concentration parameter as a function of redshift, as shown as solid lines in Fig. 26. The error bars seen on the N-Body values denote the range of halo masses used to calculate the concentration parameter. This was done by averaging the spherical density profiles and then fitting the resulting profile to Eq. 163.

More recently, Bullock et. al developed a more general model [172]. Firstly they simplify their definition of the collapse redshift to be the redshift at which for some halo half of its final mass $M_{\rm final}$ is contained within progenitors of any mass. This is equivalent to setting $f = 0$ in the NFW definition.

Additionally, they generalise the model by defining a more general characteristic density $\tilde{\rho_s}$, defined by $M_{\rm vir} \equiv \frac{4\pi}{3} r_s^3 \tilde{\rho_s}$. As done previously, this is then assumed to be associated with the density of the universe at the time of collapse according to

$$\tilde{\rho_s} = \kappa_{\rm B}^3 \Delta_{\rm vir}(a)\rho_u(a), \tag{169}$$

where $\kappa_{\rm B}$ is a proportionality constant which represents the contraction of the inner halo above the standard requirements from dissipationless top-hat halo virilisation.

For a universe dominated only by matter, it can then be found that

$$c(M, a) = \kappa_{\rm B}\frac{a}{a_{\rm col}} = \kappa_{\rm B}\frac{x}{x_{\rm col}}. \tag{170}$$

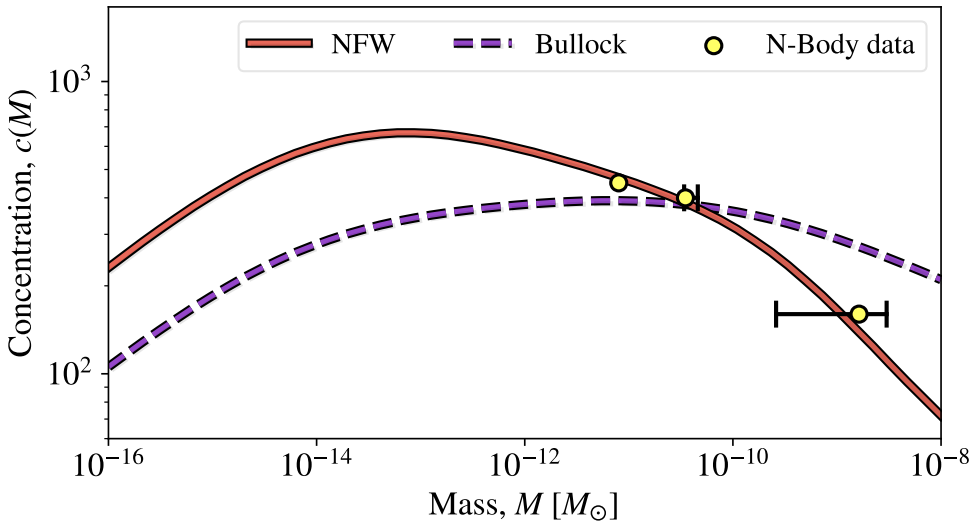

FIG. 26. *Concentration Parameter Estimates.* Curves calculated by solving Eq. 164 using the initial power spectrum to estimate the collapse redshift and combining with the concentration estimation formalism of NFW (solid lines) via Eq. 166 and Eq. 168 using $f = 0.01$ and the concentration estimation formalism of Bullock et. al (dashed lines) via Eq. 171 with $f = 10^{-5}$. The free parameters are determined using a least-squares fit to N-Body results from Ref. [87] and are found to be $\kappa_{\rm NFW} = 1.28 \times 10^5$ and $\kappa_{\rm B} = 10.7$ respectively.

However, again this must be modified to account for early radiation domination through Eq. 167. The new relation is found to be

$$c(M, x) = \kappa_{\rm B} \left(\frac{x^{-3} + x^{-4}}{x_{\rm col}^{-3} + x_{\rm col}^{-4}} \right)^{1/3}. \tag{171}$$

It can be seen that we recover Eq. 170 in the limit of large x and $x_{\rm col}$. Since $x_{\rm col}$ tends towards a constant value, we can therefore predict, as done by Bullock et. al, that at late times $c(M, x) \propto x$. While it is not as easy to see, the same is also true for the NFW case.

As with the NFW approach, we use this to predict the concentration parameter. For consistency with the Bullock approach, we use $f = 10^{-5} \approx 0$. Then, using a least-squares fit to the N-Body data at $z = 99$ and find a proportionality constant $\kappa_{\rm B} = 10.7$. This can be seen in as dashed curves in Fig. 26.

We see that the peak in concentration forms at $M \approx 2.4 \times 10^{-11} M_\odot$, roughly two orders of magnitude larger than predicted using the NFW approach. It should be noted that the overall shape of the curve is determined only by the choice of the progenitor fraction f

(as used in Eq. 164). The different treatments of the scale density change primarily the normalisation of the curve at each redshift.

It is clear from Fig. 26 that the NFW approach fits the N-Body results the best. We, therefore, choose to apply this approach moving forwards to our solution of the excursion set on the full initial density field.

Once we have fitted our concentration calculation to the N-body results, we can use it to estimate halo concentrations at any redshift as shown in Fig. 27. We see that at very early redshifts, all halos are predicted to have approximately the same concentration. This is because the threshold for collapse is still very high, as seen from Fig. 21. As a result, any collapsed object that is found, regardless of mass, will have most likely only just formed. Then, since the concentration is assumed to depend only on the collapse redshift, the value is, therefore, the same for all masses. At around matter-radiation equality a peak begins to form at $M \approx 10^{-13} M_\odot$. The location of this peak does not change over time. This indicates that at any point in time, objects with a mass around this value are the oldest and therefore most concentrated.

We will show later in Sec. VIII that this still provides a good description of the miniclusters density profiles even before matter-radiation equality.

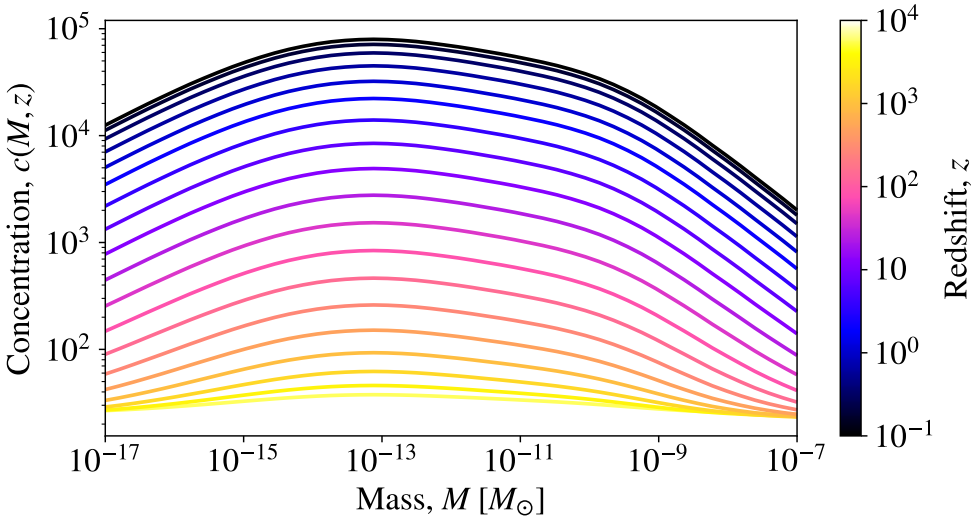

FIG. 27. *NFW concentration over time.* Curves calculated by solving Eq. 164 using the initial power spectrum to estimate the collapse redshift and using Eq. 166 with a progenitor mass fraction $f = 0.01$ and fitting parameter $\kappa_{\rm NFW} = 1.28 \times 10^5$ for many different redshifts.

B. Power-law profiles

While we know that high-mass miniclusters are well described by an NFW profile, we do not know if this is also true for smaller masses. As mentioned before, the NFW profile is expected to arise as a consequence of hierarchical structure formation. Such mergers naturally increase the total mass of a minicluster. Therefore, we might expect that some smaller miniclusters may have undergone few to no mergers and therefore exhibit a distinctly different density profile. Additionally, since the objects that collapsed very early are so dense, we might expect them to survive the merger process and therefore continue to exist today as substructures. Like with the low-mass miniclusters, it is possible that having experienced very few mergers, this substructure has a density profile that is not well described by NFW. We will therefore also consider the other most popular density profile for miniclusters: the single power law.

Analytical studies of self-similar infall typically predict that this should result in power-law density profiles of the form

$$\rho(r) = \rho_0 \left(\frac{r}{r_0}\right)^{-\alpha} \tag{172}$$

It was first shown that an initially static uniform spherical overdensity produces a density profile with $\alpha = 3$. However, under this approximation, later studies showed overdensities in an expanding background instead produces a density profile $\alpha = -9/4$ [173, 174]. Additionally, an axion field with a white-noise initial power spectrum simulated with N-body until $z = 3000$, produced halos with this predicted density profile [175]. As a result of this, many have assumed that axion miniclusters today might exhibit this type of density profile [77, 78].

To fully predict the density profile, we also need a relationship between the mass and radius of these miniclusters. One approach used in the past has been to take the total average density of the minicluster given by Eq. 127 found by Kolb and Tkachev [67, 77, 79]. We can use this to calculate the radius for a halo of some mass and initial overdensity δ_i.

If we define r_0 to be this radius, we can integrate Eq. 172 with respect to the radius to find that

$$M = \frac{4\pi\rho_0}{3-\alpha} r_0^3, \tag{173}$$

and hence

$$\rho_0 = \frac{3-\alpha}{3}\langle\rho\rangle \tag{174}$$

Now, given a mass and an initial overdensity δ_i, we can predict a power-law profile. However, at each point in time, there is a single threshold overdensity that defines which objects have collapsed. Therefore, all virialised objects at a single point in time can be considered to have the same initial overdensity [16]. By comparing the linear growth of an adiabatic perturbation overdensity, given by Eq. 130, with the non-linear collapse of a spherical tophat, given by Eq. 122, we find that the initial overdensity which collapses at redshift z is given by

$$\delta_{i,\mathrm{col}}(z) = \frac{1.686}{1-D(z)}, \tag{175}$$

where $D(z)$ is the growth factor given by

$$D(z) = 1 + \frac{3}{2}\left(\frac{z_{\mathrm{eq}}+1}{z+1}\right), \tag{176}$$

and z_{eq} is the redshift of matter-radiation equality. The collapsing initial overdensity is therefore inversely proportional to the scale factor and $\delta_{i,\mathrm{col}}(z_{\mathrm{eq}}) \sim 1$ [88].

C. Axion stars

Since the axion likely has a very small mass, it will also have a comparatively large de Broglie wavelength. This suppresses structure formation on small scales due to the uncertainty principle. Additionally, when the axions are cold, they can form a Bose-Einstein condensate. This condensation produces a solitonic core known as an axion star. The density profile of this core is well approximated by a Bose star solution[17]

$$\rho_\star(r) \approx \rho_0 \left[1 + 0.091\left(\frac{r}{r_\star}\right)^2\right]^{-8}, \tag{177}$$

with

$$\rho_0 = \frac{1.9\times10^{-6}}{a}\left(\frac{10^{-8}\mathrm{eV}}{m_a}\right)\left(\frac{10^{-3}\mathrm{pc}}{r_\star}\right)\frac{M_\odot}{\mathrm{pc}^3} \tag{178}$$

[16] Later we show the different initial densities of objects at z_{eq} based on their collapse redshift defined in Sec. V A. This collapse redshift is unique to each halo and ,therefore, should not be confused with the statement made here.

[17] This is in comoving coordinates.

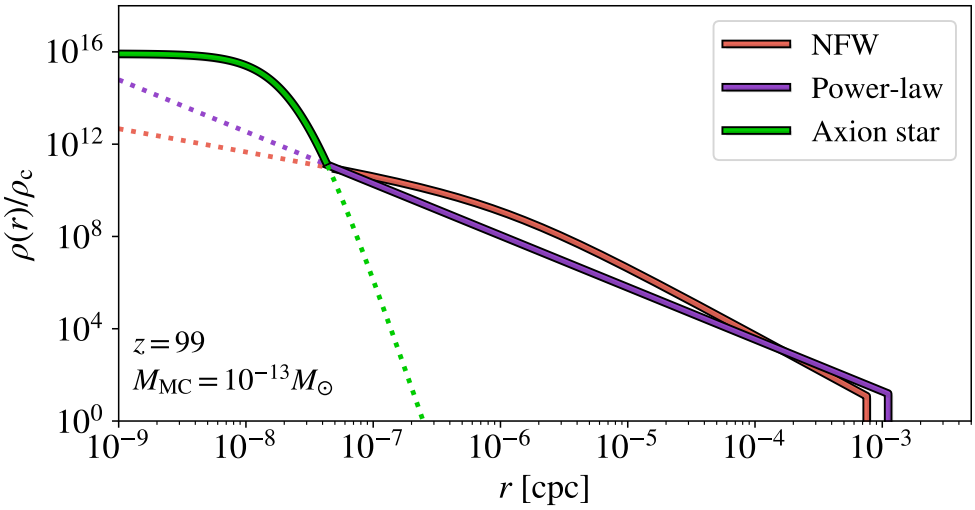

FIG. 28. *Possible Minicluster Density Profiles.* Red: NFW profile with a concentration given by the PS estimate shown in Fig. 26. Purple: Power-law profile with an $\alpha = 9/4$ slope and a radius given by Eq. 173. Green: Profile of the central axion star given by Eq. 177.

where $M_\star$ and $r_\star$ are the axion star mass and radius respectively. We see, as shown in Fig. 28, that this gives a flat core at the centre of dark matter halos. [176–178].

These solitons are most often considered for ultra-light axions ($m_a \sim 10^{-22}$eV) as a way of explaining problems faced by classic CDM such as the missing-satellite [179, 180] and cusp-core problems [169, 181]. However, it has been shown that they also form for masses which are relevant for the QCD axion [182].

Axion stars make up a significant part of the structure of miniclusters. They are particularly important in the context of gravitational microlensing as their flat core acts as a small radius cut-off which prevents the miniclusters "main" density profile from producing microlensing. This is discussed further in Sec. VI.

Simulating the formation of axion stars requires solving the full Schrödinger-Poisson equations. Therefore, the N-body simulations from Ref. [87] used in this work are unable to observe their formation. However, we can estimate the axion star masses and radii using known scaling relations.

Using wave simulations, Schive et al. found that the masses of axion stars are related to the total system energy and mass by

$$M_c' \sim \left(\frac{|E'|}{M'}\right)^{1/2} \tag{179}$$

where the primes denote that we are using redshift-independent coordinates ($M' = a^{3/4}M$, $E' = a^{5/4}E$, $x' = a^{1/4}x$).

Taking E' and M' in Eq. 179 to be the energy and mass of the halo respectively we can use the virial theorem to find that the total halo energy is given by

$$|E'_h| = \frac{|E'_p|}{2} \tag{180}$$

where E_p is the total gravitational potential energy.

For a uniform sphere, we know that

$$|E'_p| = \frac{3M'^2_h}{5x'_{vir}} \tag{181}$$

and hence

$$|E'_h| = \frac{3M'^2_h}{10x'_{vir}}. \tag{182}$$

Therefore, reinstalling the redshift dependence, we find the relation

$$M_c \sim a^{-1/2}\left(\frac{3M_h^2}{10x_{vir}}\right)^{-1/2}. \tag{183}$$

We can then remove x_{vir} by recalling the halo mass definition to find that

$$M_c \sim a^{-1/2}\xi(z)^{1/6}M_h^{1/3} \tag{184}$$

Due to the definition of the core mass $M(r < r_c)$, the core contains around 25% of the total soliton mass. We can therefore fix the units of the core-mass equation by requiring that

$$M_c(z = 0, M_h = M_{\min,0}) = \frac{1}{4}M_{\min,0}, \tag{185}$$

where $M_{\min,0}$ is the axion Jeans mass given by

$$M_{\min,0} = 375^{-1/4}32\pi\xi(0)^{1/4}\rho_{\mathrm{m}0}c^3\left(\frac{H_0 m_a}{\hbar}\right)^{-3/2}\Omega_{\mathrm{m}0}^{-3/4}. \tag{186}$$

Performing this process we find that

$$M_c = \frac{1}{4}a^{-1/2}\left(\frac{\xi(z)}{\xi(0)}\right)^{1/6}\left(\frac{M_h}{M_{\min,0}}\right)M_{\min,0} \tag{187}$$

This derivation assumes that the parent halos collapse during the matter-dominated era. This however is not true for axion miniclusters which we know begin to collapse deep into the radiation domination era. Additionally, if the minicluster sub-halos do have power-law

profiles, the central overdensity may be much larger than if they formed NFW profiles. This means that our assumption that the axion star forms within a uniform sphere of dark matter is made less valid in this case. However, as shown in Appendix. B, accounting for these factors makes a subdominant contribution to the core mass.

The axion star mass can be conveniently expressed in terms of the virial velocity of its parent halo. Simulations have found this relation to be

$$M_\star = 4.69 \frac{\hbar}{m_a} \frac{v_{\rm vir}}{G} \tag{188}$$

where $v_{\rm vir}$ is the virial velocity of the parent halo [183]. This can be rewritten as

$$M_\star = 4.16 \times 10^{-15} \left(\frac{50\mu{\rm eV}}{m_a}\right) \left(\frac{v_{\rm vir}}{0.1{\rm m\ s^{-1}}}\right) \tag{189}$$

and hence the axion star radii via

$$r_\star = 1.98 \times 10^{-9} \left(\frac{50\mu{\rm eV}}{m_a}\right)^2 \left(\frac{10^{-16} M_\odot}{M_\star}\right) {\rm pc}. \tag{190}$$

We can use this to "paint-on" the axion stars for halos in the N-body data by calculating their virial velocity. As mentioned previously we consider the axion star radius to be a small-radius cut-off on a halo's ability to lens.

D. Scaling relations

The masses and radii of axion miniclusters and their central axion stars are dependent on the mass of the axion. Therefore these calculations for these halo properties can be rescaled to other axion masses.

The masses of miniclusters scale as

$$M \sim \left(\frac{1}{m_a}\right)^{0.5}. \tag{191}$$

Lengths scale similarly as

$$L \sim \left(\frac{1}{m_a}\right)^{0.167}. \tag{192}$$

We can calculate similar scalings for our predicted axion star masses and radii. We expect that the virial velocity should scale as

$$v_{\rm vir} \sim M^{1/3} \sim \left(\frac{1}{m_a}\right)^{1/6}. \tag{193}$$

Therefore, from Eq. 188, we see that the axion star mass will scale as

$$M_\star \sim \frac{v_{\rm vir}}{m_a} \sim \left(\frac{1}{m_a}\right)^{7/6} \tag{194}$$

Finally, we can also use this to scale the axion star radius as

$$R_\star \sim \frac{1}{M_\star m_a^2} \sim \left(\frac{1}{m_a}\right)^{5/6} \tag{195}$$

We see that as the axion mass increases, the halo masses and radii decrease. The axion stars, however, have additional dependencies on the axion mass. We see that increasing axion mass increases the axion star mass while decreasing the axion star radius. Importantly, the axion star radius shrinks quicker than the parent halo. Therefore, at larger axion masses, the relative size of the axion star to the halo is smaller.

Throughout this work, we have assumed an axion mass of $m_a = 50\mu$eV. However, these scaling relations can be used to generalise our results to other axion masses.

VI. GRAVITATIONAL MICROLENSING

We have seen in Sec. II C 2 that gravitational lensing provides astronomers a way to detect matter which does not emit or block any light. Generically, gravitational lensing creates additional images of the original source. In microlensing, the separation between these images is typically too small to resolve[18]. Instead, we observe the combined brightness of all of the images together. We can observe this lensing as a brief magnification of the source light as a lens passes close to the line-of-sight to a light source as shown in Fig. 29. The first microlensing event was observed in 1979 [185]. Since then, microlensing has been used to discover over one hundred exoplanets and constrain the properties of dark matter [43, 186, 187].

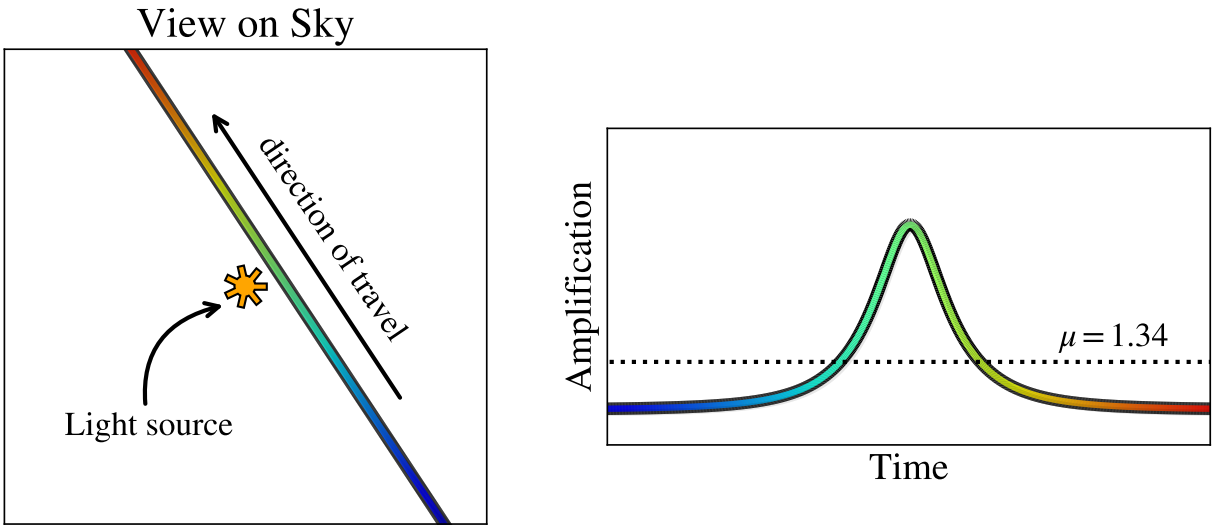

FIG. 29. *Point-mass microlensing event.* (Left) View on the sky centred on a light source (e.g a star) as a gravitational lens passes close to the line-of-sigh between the source and observer. Right: Amplification of the observed light over time. Line colour indicates time.

In Sec. VI A, we will introduce the simplest case of point light sources being lensed by point masses. This case is appropriate for most objects with masses greater than around that of typical asteroids. Then, in Sec. VI B we will derive, for the case of a point mass, the lowest-mass limit to microlensing enforced by wave effects. A complete microlensing calculation would also include the effect of the light source also having a finite size. However, as shown

[18] It should be noted that using modern techniques, it is sometimes possible to resolve the individual images [184]. However, this is not significant for this work.

in Ref. [188], these considerations make little contribution when included with wave-effects. We, therefore, do not consider them here. Finally, in Sec. VI C we will explore how we can incorporate the impact of a lens having an extended mass profile instead of being a point-mass. This consideration is essential for objects just as axion miniclusters. Some of this text has been taken from the section on microlensing that I wrote for Ref. [91].

A. Microlensing Basics

The magnification for a point source by a point mass, such as a primordial black hole (PBH), under the geometrical optics approx is given by

$$\mu^{p}_{nw}(u) = \frac{u^2+2}{u\sqrt{u^2+4}} \tag{196}$$

where $u = \xi/R_{\rm E}$ is a dimensionless impact parameter and $R_{\rm E}$ is the Einstein radius given by

$$R_{\rm E}(x) = 2\left[\frac{GMx(1-x)D_S}{c^2}\right]^{1/2}, \tag{197}$$

where $x = D_L/D_S$ in which D_L is the distance to the lends and D_S is the distance to the source. We use the same notation as in Ref. [188] in which the superscript p indicates that this is for a point mass and the subscript nw (no-wave) indicates that this equation does not include wave effects. As shown in Fig. 30, that the magnification is greater than 1.34 for $u < 1$. From this, we define a threshold impact parameter $u_{\rm T}$ as the maximum impact parameter which produces a magnification of 1.34.

This defines our *lensing tube* which has a radius of $u_{\rm T}R_{\rm E}(x)$. Only objects which cross the lensing tube with an impact parameter less than this threshold can produce measurable lensing events. For point masses under this approximation, the threshold impact parameter is one by definition. However, as we will see later, for more complex lensing models this impact parameter is dependent on both the lens structure and it's distance from the observer.

Currently, most of the constraints on PBHs come from two microlensing surveys. These are the Expérience pour la Recherche d'Objets Sombres (EROS) and the Subaru Hyper Suprime-Cam (HSC) surveys.

The EROS survey was the first of these two. This group observed stars within the Large Magellanic Cloud (LMC) located 50kpc away from Earth with galactic coordinates $(l, b) = (280^\circ, -33^\circ)$. They measured the brightness of each star in their sample every day

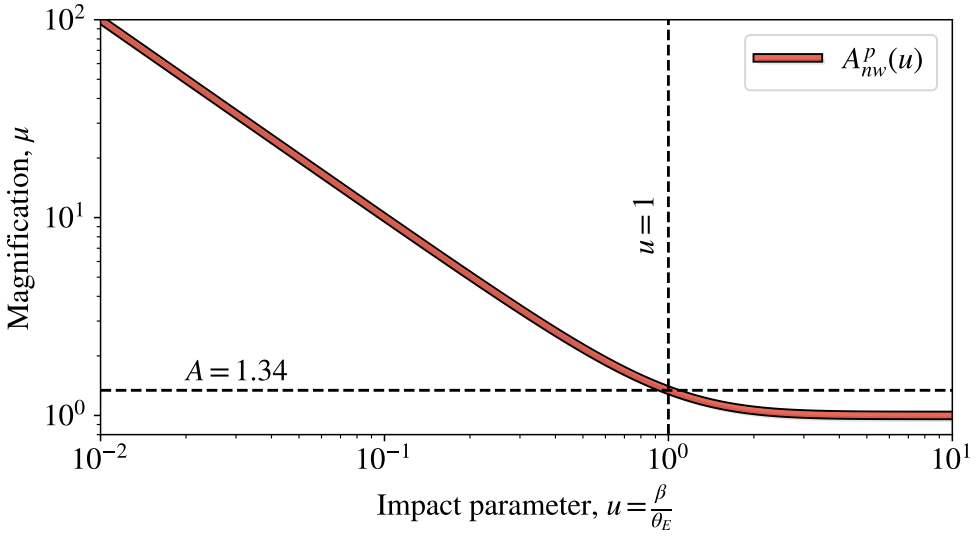

FIG. 30. *Simplified microlensing magnification.*

for a total of 1000 days with a total exposure of 3.67×10^7 star years. As shown in Fig. 11, this constrains the PBH mass fraction for masses in the range $5 \times 10^{-8} M_\odot < M_{\rm PBH} < 15 M_\odot$.

The Subaru/HSC survey instead makes measurements of stars within the Andromeda Galaxy (M31) located 770kpc away from Earth with galactic coordinates $(l, b) = (121.2°, -21.6°)$. They repeated their brightness measurements around every two minutes for seven hours over a single night. Determining exposure for HSC is a little more complicated than for the EROS survey. For simplicity, we follow Ref. [79] and find their exposure by calculating calculating a constraint curve for their survey and choosing the exposure which best matches the curve presented in Fig. 25 of Ref. [187]. Doing this we find an effective exposure of $E \sim 9.5 \times 10^4$ star years. Due to the smaller temporal resolution, the Subaru/HSC survey is able to constrain much lighter masses than EROS. As we seen in Fig. 11, they constrain are able to constrain the PBH mass fraction in the range $2.5 \times 10^{-12} M_\odot < M_{\rm PBH} < 10^{-5} M_\odot$. As we saw from Eq. 114, we expect axion miniclusters to have typically have masses $\sim (10^{-12} M_\odot$. We therefore only consider constraints from the Subaru/HSC.

The differential detection rate for light produced by point sources and lensed by point masses M is given approximately by

$$\frac{d\Gamma}{d\hat{t}} = \frac{32 D_s u_T^4}{\hat{t}^4 v_c^2} \frac{1}{M} \int_0^1 \rho(x) R_E^4(x) e^{-Q(x)} {\rm d}x, \tag{198}$$

where $\hat{t}$ is the time taken to cross the Einstein diameter, L is the exposure, $v_c = 220$ km s^{-1} is the local circular speed and

$$Q(x) = \frac{4R_E^2(x)u_T^2}{\hat{t}^2 v_c^2}. \tag{199}$$

To estimate the line-of-sight DM density, the Subaru/HSC model the density of the MW and M31 as NFW profiles as given by Eq. 163. The MW and M31 are taken to have scale densities of $4.88\times10^6 M_\odot$ kpc^{-3} and $4.96\times10^6 M_\odot$ kpc^{-3} and scale radii of 21.5kpc and 25kpc respectively. We see from Fig. 31 that the density from M31 gives a significant contribution to the total.

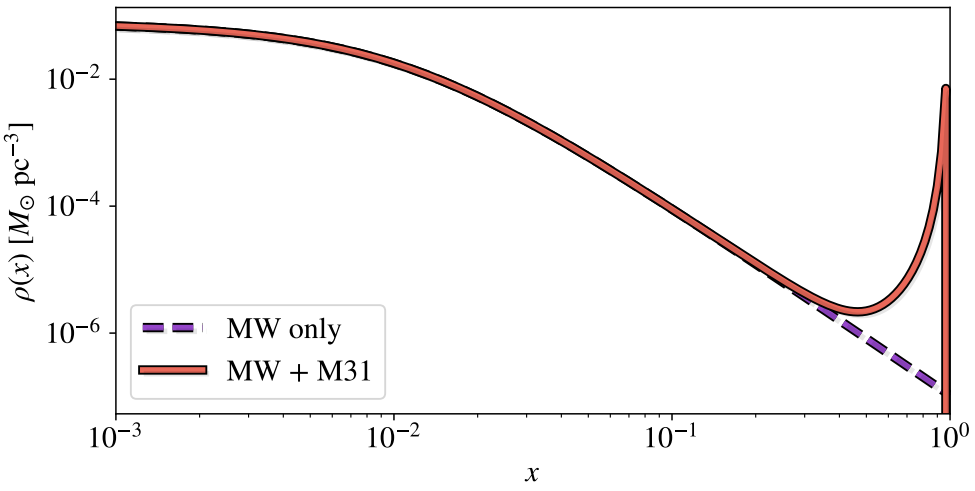

FIG. 31. *Subaru/HSC line-of-sight density.* Calculated assuming the MW and M31 both have NFW density profiles as given by Eq. 163.

Using this line-of-sight density, we can calculate the differential detection give by Eq. 198. We assume that the PBH dark matter has a monochromatic mass function, that is, all PBHs have a single mass. The resulting differential detection rate is shown for a range of masses in Fig. 32.

We can then estimate the expected number of observed events by integrating Eq. 198

$$N_{\rm exp} = E\int_0^\infty \frac{{\rm d}\Gamma}{{\rm d}\hat{t}}\epsilon(\hat{t}){\rm d}\hat{t}, \tag{200}$$

where E is the exposure and the sensitivity $\epsilon(\hat{t})$ is the probability that an event with a

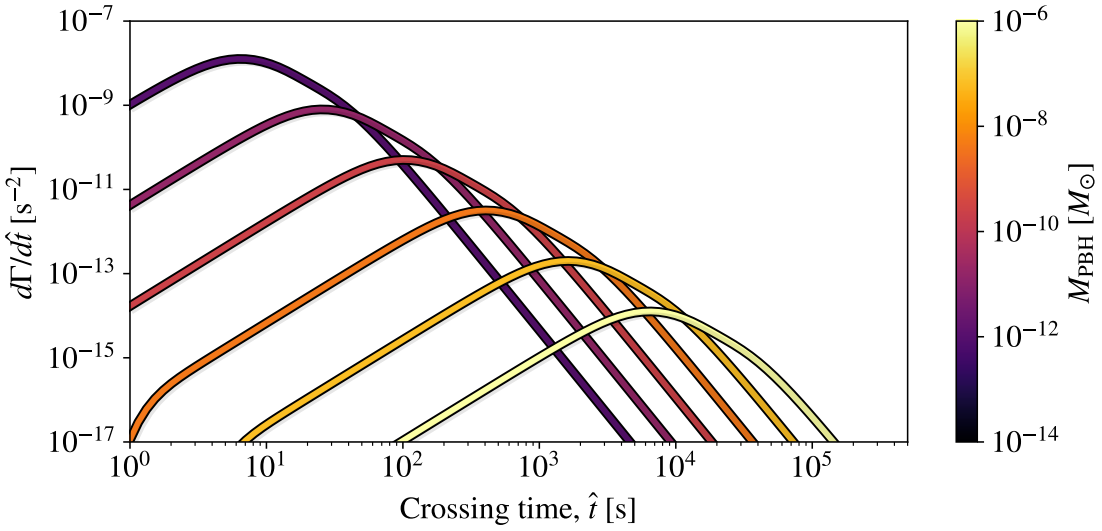

FIG. 32. *Subaru/HSC Differential Detection Rate.* Calculated assuming the MW and M31 both have NFW density profiles as given by Eq. 163 for point-mass lenses with masses from $M = 10^{-12} M_\odot$ to $M = 10^{-6} M_\odot$.

duration $\hat{t}$ is detected. For HSC, we can approximate the sensitivity of the HSC survey as

$$\epsilon(\hat{t}) = \begin{cases} 0.5 & \text{if } 180\text{s} < \hat{t} < 10800\text{s} \\ 0 & \text{otherwise.} \end{cases} \tag{201}$$

From Poisson statistics, the probability of k events occurring in a time interval t is given by

$$P(k|t) = \frac{(rt)^k e^{-rt}}{k!} = \frac{N_{\rm exp}^k e^{N_{\rm exp}}}{k!}. \tag{202}$$

Therefore, in the absence of any observed events, we can find the 95% confidence interval upper limit by finding f_{pbh} such that $N_{\rm exp} = 3$. We can therefore simply calculate this interval as

$$f_{\rm pbh}^{95\%} = \frac{3}{N_{\rm exp}(f_{\rm pbh} = 1)}. \tag{203}$$

where $f_{\rm pbh}$ is the PBH mass fraction given by

$$f_{\rm pbh} = \frac{\Omega_{\rm pbh}}{\Omega_{\rm DM}}. \tag{204}$$

The resulting constraint on the PBH mass fraction is shown in Fig. 33.

This calculation however overestimates the Subaru/HSC ability to constrain the abundance of PBHs as we have not included wave effects. As we will see in the next subsection,

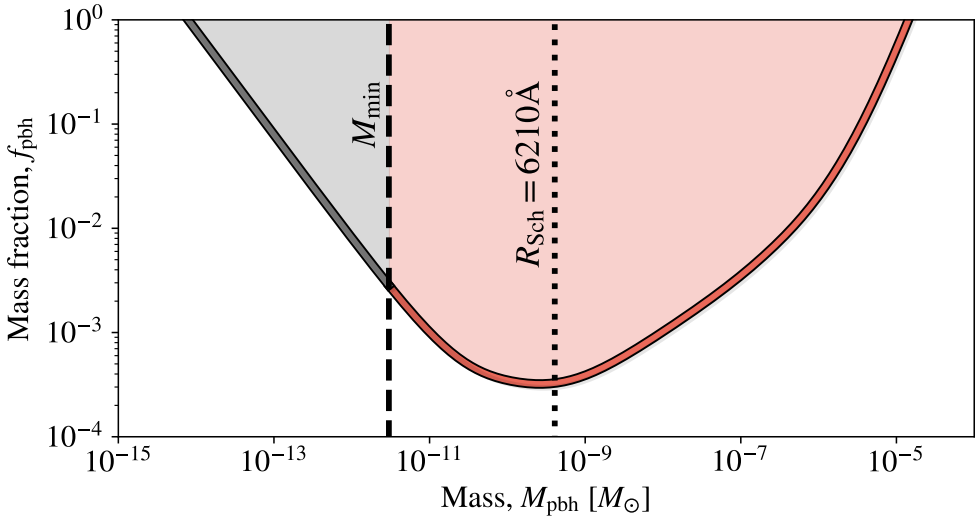

FIG. 33. *Subaru/HSC PBH Constraint.* Calculated assuming the MW and M31 both have NFW density profiles as given by Eq. 163 for a single mass PBH without wave effects. The black dotted shows the point at at which wave effects become important and the black dashed line shows the mass below which wave effects completely suppress microlensing.

wave effects suppress the ability of very low-mass objects to produce microlensing signals. We highlight this cut-off for the Subaru/HSC survey on Fig. 33.

B. Wave effects

The "geometrical optics approximation" outlined above is only applicable when the Schwarzschild radius of the gravitational lenses is much larger than the wavelength of the lensed light. For point-like lenses this simply means that the approximation is only valid for large masses. For smaller masses, this approximation breaks down and we have to consider wave optics effects. As we will see, these wave effects suppress the the magnification of light due to small masses therefore reducing their detectability.

When wave optics are included, the magnification due to a point-mass is given by

$$A^p_w(w,u) = \frac{\pi w}{1-e^{-\pi w}} \left| {}_1F_1\left(\frac{i}{2}w, 1; \frac{i}{2}wu^2\right)\right|^2, \tag{205}$$

where w parameterises the wave effects and is given by

$$w \equiv \frac{8\pi GM}{\lambda} \tag{206}$$

in which λ is the wavelength of the source light and ${}_1F_1$ is the confluent hypergeometric function. Here again, we follow the notation used by Ref. [188] in which "w" denotes "wave-effect". In the limit of small wavelengths ($w \gg 1$) we recover the magnification under the geometrical optics approximation

$$A^p_{geo}(w,u) = \frac{u^2+2}{u\sqrt{u^2+4}} + \frac{2}{u\sqrt{u^2+4}} \sin\left[w\left(\frac{1}{2}u\sqrt{u^2+4} + \log\left|\frac{\sqrt{u^2+4}+u}{\sqrt{u^2+4}-u}\right|\right)\right]. \quad (207)$$

We see that we recover the "no-wave" magnification of Eq. 196 plus an additional contribution which rapidly oscillates with u. We will assume an r-band filter wavelength of $\lambda = 6210\mathring{A}$ and a lens redshift of $z_L \approx 0$. The magnification as a function of impact parameter including these wave effects is shown in Fig. 34.

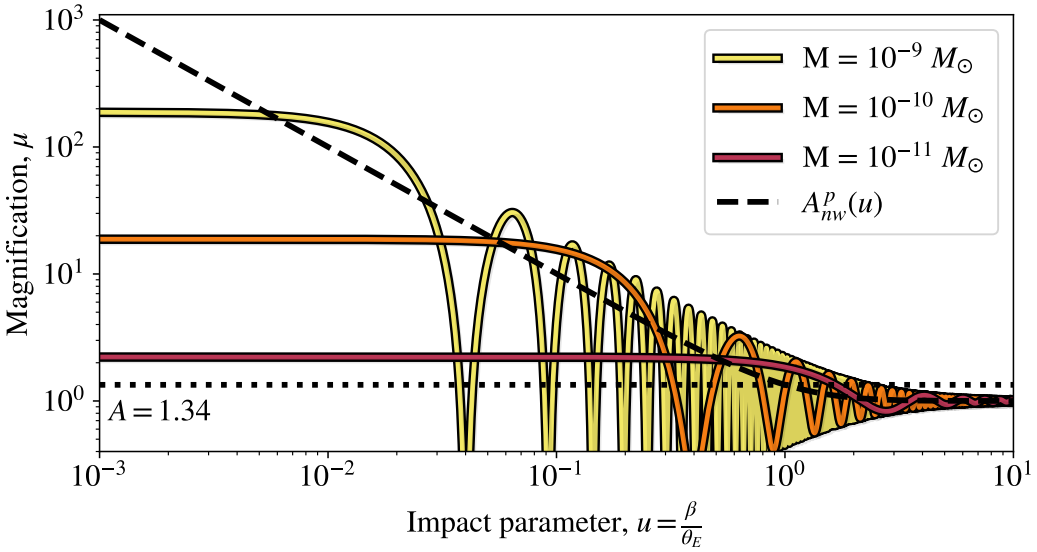

FIG. 34. *Magnification with wave effects.* Calculated using Eq. 205 assuming an r-band filter wavelength of $\lambda = 6210$Å and a lens redshift of $z_L \approx 0$ for a point mass. Black-dashed line shows the "no-wave" approximation given by Eq. 196.

We see that for large masses and impact parameters, the solution including wave effects oscillates around the "no-wave" approximation given by Eq. 196. However, unlike in the "no-wave" approximation, the magnification tends to a constant at small impact parameters. Fig. 34 also shows us that the central magnification $\mu_0 = \mu(u = 0)$ decreases with lens mass. This means that below some threshold lens mass $M_{\rm min}$, the maximum magnification will be less than the threshold value of 1.34. As shown in Fig. 35, this minimum detectable

mass is $M_{\rm min} \approx 3 \times 10^{-12} M_\odot$. This is the minimum mass which the Subaru/HSC is able to constrain. Since most surveys will likely use a similar filter wavelength, we will take take this to be a rough lower limit on all microlensing surveys.

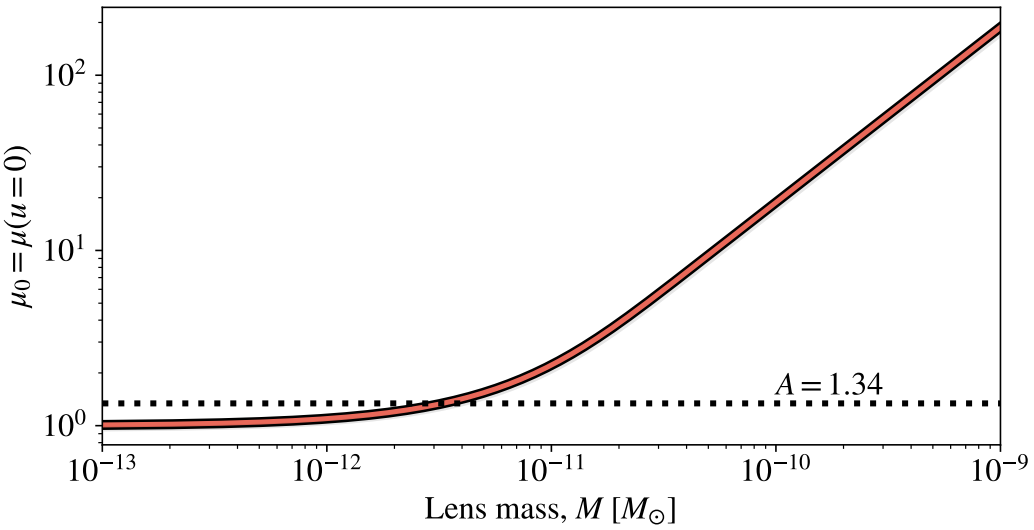

FIG. 35. *Central Magnification with wave effects.* Calculated using Eq. 205 assuming an r-band filter wavelength of $\lambda = 6210$Å and a lens redshift of $z_L \approx 0$ for a point mass. Black dotted line shows the threshold magnification below which we assume microlensing events are not visible.

So far we have only considered the lensing of point masses. However, the objects we are interesting in, axion miniclusters, are extended objects. This, as we will see, plays a critical role in whether or not miniclusters are able to produce microlensing signals.

C. Extended Sources

Since axion miniclusters are not point-masses, we have to consider their extended density profile. Specifically, we need to consider the two-dimensional projection of this density onto the lens plane known as the surface mass density $\Sigma(\xi)$ (and hence the surface mass profile $M(\xi)$) where ξ is the radial coordinate from the line between the centre of the distribution ($r = 0$) and the observer at infinity.

For an axisymmetric mass distribution, the magnification is found to be

$$\mu(\xi) = \frac{1}{(1-B)(1+B-C)}, \tag{208}$$

with

$$C = \frac{1}{\Sigma_c \pi r} \frac{\mathrm{d}M(\xi)}{\mathrm{d}\xi}; \quad B = \frac{M(\xi)}{\Sigma_c \pi r^2} \tag{209}$$

where

$$\Sigma_c = \frac{c^2 D_s}{4\pi G D_L D_{LS}} \tag{210}$$

is the critical surface mass density for lensing [79, 189]. We will see that the threshold impact parameter is always smaller for an extended lens than for a point lense of the same mass. This makes means that the probability of events is lower and that the lensing events that do occur are shorter, as shown in Fig. 36.

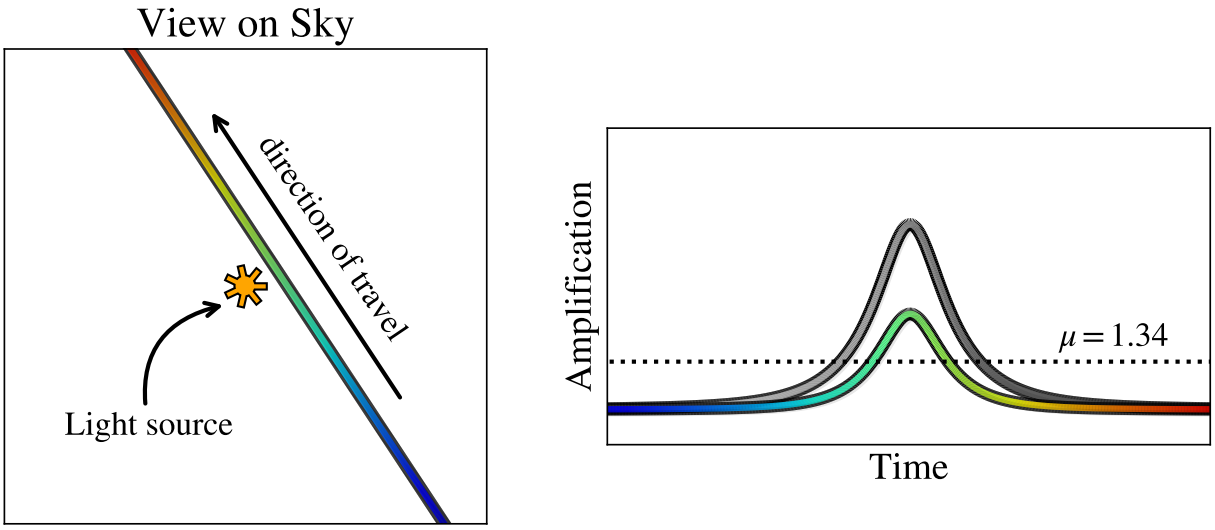

FIG. 36. *Extended-profile microlensing event.* (Left) View on the sky centred on a light source (e.g a star) as a gravitational lens passes close to the line-of-sigh between the source and observer. Right: Amplification of the observed light over time for an extended (coloured) and point (gray) lens. Line colour indicates time.

We will consider two possible density profiles a power-law profile and the NFW profile. As done by Fairbairn et. al in Ref. [79], calculating the ratio of the impact parameters which can produce lensing in the extended lens case to the point mass case. This is given by

$$\mathcal{R} = \left\langle \frac{\xi_c(x)}{R_{\mathrm{E}}(x)} \right\rangle_x, \tag{211}$$

where $\xi_c(x)$ is the maximum radius in the lens plane at which the magnification is greater than 1.17. This is the value of the magnification of the outermost image in the point mass case.

It is important to remember at this point that the density profiles of axion miniclusters have a natural small radius cut-off due to their central axion star. This is because the axion star has a cored density profile and hence $C \approx 0$ and $B \sim$ const. Therefore, the magnification reaches a maximum as it crosses the axion star radius. As a result, if $\xi_c(x)$ is smaller than the axion star radius the minicluster will be unable to produce microlensing. It is possible that the axion stars themselves are able to produce microlensing (See Refs. [190–192]). However, such considerations are beyond the scope of this work.

1. NFW Profile

Integrating the NFW profile as given by Eq. 172 along the line of sight from $-\infty$ to ∞, it can be shown that the NFW profile have a surface mass density given by

$$\Sigma(x) = \frac{\rho_s r_s}{x^2 - 1} f(x), \tag{212}$$

in which

$$f(x) = \begin{cases} 1 - \frac{2}{\sqrt{x^2-1}} \arctan \sqrt{\frac{x-1}{x+1}} & \text{if } x > 1, \\ 1 - \frac{2}{\sqrt{1-x^2}} \arctan \sqrt{\frac{1-x}{1+x}} & \text{if } x < 1, \\ 0 & \text{if } x = 1, \end{cases} \tag{213}$$

where $x = \xi / r_s$ and ξ is the radius in the lens plane [42]. The surface mass profile can then be calculated numerically by integrating Eq. 212 as

$$M(\xi) = 2\pi \int_0^{\xi} \Sigma \left(\frac{\xi}{r_s} \right) \xi d\xi. \tag{214}$$

It should be noted that we have assumed that the halo extends infinitely beyond its virial radius which we know to be untrue. However, the mass contributed by large radii is very small. Additionally, we can make a partial fix to this approximation by enforcing that $M(r > R_{\rm vir}) = M_{\rm vir}$.

We can then substitute Eq. 214 into Eq. 208 to calculate the magnification as a function of impact parameter. We can do this as a function of concentration c and minicluster mass $M_{\rm MC}$ as shown in Fig. 37. Where, for simplicity, we take the virial radius to be R_{200} defined by

$$R_{200} = \left(\frac{3 M_{\rm MC}}{4\pi (200 \rho_c)} \right)^{1/3}, \tag{215}$$

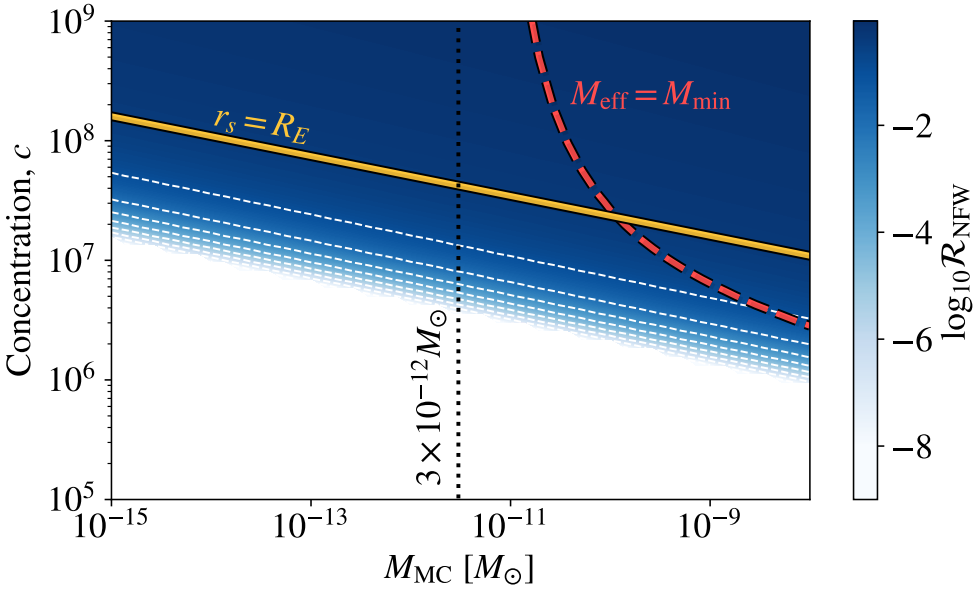

FIG. 37. *NFW Lensing Ratio.* Ratio of threshold radius to Einstein radius for an NFW profile with concentration c. Yellow line highlights where halos have a scale radius equal to the Einstein radius. The red dashed line shows the contour above which halos have a mass contained within the impact parameter greater than the minimum mass for lensing allowed due to wave effects.

where ρ_c is the critical density of the universe.

We see that this lensing ratio is largely a step function with concentration. For $c \gtrsim 10^7$ the ratio is mostly 1 and for $c \lesssim 10^6$ the ratio is mostly 0. There is also a weaker correlation with mass in which a heavier halo of the same concentration has a greater lensing capability.

The sharp turn over in $\mathcal{R}$ with concentration occurs because the central $\rho \sim r^{-1}$ part of the density profile prevents the occurrence of caustics. Therefore, if the threshold magnification is not achieved within the outer $\rho \sim r^{-3}$ part of the profile, there will no be any lensing at all. We can see this more clearly by plotting the line along which the scale radius is equal to the Einstein radius $r_s = R_{\rm E}$ as shown in Fig. 37. We see that the ratio drops rapidly below this line. This confirms the previous assumption that NFW profiles can largely lens like a point mass when the scale radius is smaller than its Einstein radius.

However, this calculation does not consider the impact of wave effects. We could simply require that halos have to have a virial mass larger than our calculated minimum mass of $3 \times 10^{-12} M_\odot$ as shown in Fig. 37. However, this is incorrect as the a large proportion of the halo's density profile does not actually contribute to the lensing. Instead, we need to

consider the mass contained within ξ_c. This *effective* mass $M_{\rm eff}$ is often much smaller than the virial mass R_{200}. This, therefore, further restricts the range of NFW halos which are able to produce microlensing signals.

In Fig. 37 we show the contour for which $M_{\rm eff} > 3 \times 10^{-12} M_\odot$. Above this line, we can expect that halos are able to produce lensing signals. Since in this region $\mathcal{R} \approx 1$, all of these halos will lens much like point masses but with their smaller effective lensing mass $M_{\rm eff}$. Below this line, wave effects prevent halos from producing microlensing. As expected, we see that this line asymptotes to our minimum mass at high concentrations.

2. Power-law profile

For the power-law, we can actually find the surface mass profile analytically. Integrating Eq. 172, we can find a surface mass density

$$\Sigma_{\rm PL}(\xi) = \rho_0 r_0^{-\alpha} B\left(\frac{\alpha}{2} - \frac{1}{2}, \frac{1}{2}\right) \xi^{1-\alpha}, \tag{216}$$

where $B(x, y)$ is the Beta-function which is defined in terms of the Gamma-function $\Gamma(x) = (x-1)!$ by

$$B(x, y) = B(y, x) = \frac{\Gamma(x)\Gamma(y)}{\Gamma(x+y)}. \tag{217}$$

Integrating the radial density (as defined in Sec. V B) from zero to the virial radius, we find

$$\rho_0 r_0^{\alpha} = \frac{3-\alpha}{4\pi} \frac{M_{\rm vir}}{R_{\rm vir}^{3-\alpha}}, \tag{218}$$

allowing us to define the surface mass density in terms of the viral mass and radius as

$$\Sigma_{\rm PL}(\xi) = \frac{3-\alpha}{4\pi} \frac{M_{\rm vir}}{R_{\rm vir}^{3-\alpha}} B\left(\frac{\alpha}{2} - \frac{1}{2}, \frac{1}{2}\right) \xi^{1-\alpha}. \tag{219}$$

We see that this can be straightforwardly integrated to give the surface mass profile

$$M_{\rm PL}(\xi) = \frac{1}{2} \frac{M_{\rm vir}}{R_{\rm vir}^{3-\alpha}} B\left(\frac{\alpha}{2} - \frac{1}{2}, \frac{1}{2}\right) \xi^{3-\alpha}. \tag{220}$$

As with the NFW case, we have assumed that a halos density profile extends infinitely beyond its virial radius. This leads us to include slightly too much mass into our calculation. However, particularly for larger values of α, this additional mass makes a very small contribution. Again, we make a partial fix to this assumption by defining $M(r > R_{\rm vir}) = M_{\rm vir}$.

From Eq. 138, we expect that collapsed halos at $z = 99$ will have an overdensity of $\delta_c = 1.72$. This relates to an initial overdensity of $\delta_i = 0.0318$. As discussed previously, can use this to fix the relation between $M_{\rm vir}$ and $R_{\rm vir}$ using the expected final density given by Eq. 127. We can therefore calculate $\mathcal{R}$ as a function of M and α as shown in Fig. 38.

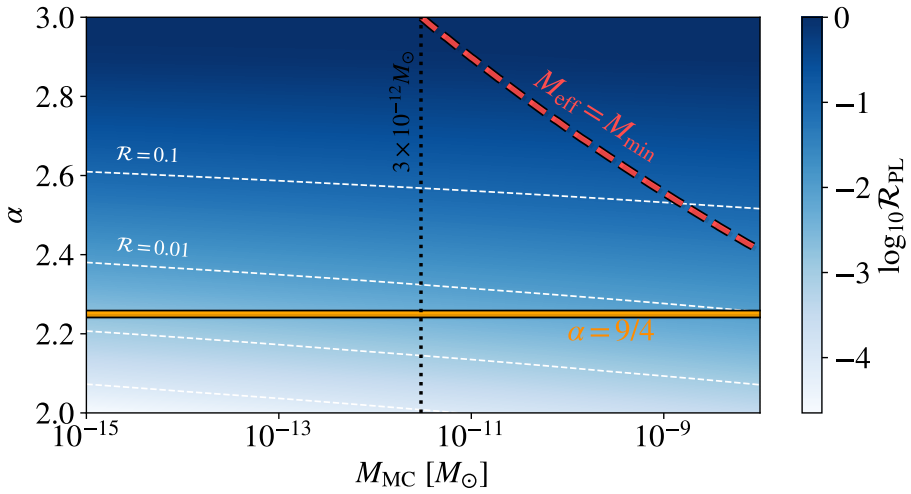

FIG. 38. *PL Lensing Ratio.* Ratio of threshold radius to Einstein radius for an PL profile with slope α. Yellow line highlights where $\alpha = 9/4$. The red dashed line shows the contour above which halos have a mass greater than the minimum mass for lensing allowed due to wave effects.

We see that for all of the PL density profiles shown ($2 \leq \alpha \leq 3$) there exists some small radius at which the halo can produce lensing (before including wave effects). Although not shown here, this is the case for all halos with $\alpha > 1$.

However, as before, we need to consider the wave effects. Fig. 38 shows the contour where the effective lensing mass $M_{\rm eff}$ is large enough for the lensing signal not to be completely suppressed by wave effects. We see that for the relevant mass ranges, a slope of $\alpha = 9/4$ is not steep enough to produce a microlensing signal for our chosen value of δ_i.

VII. FORMATION OF AXION MINICLUSTERS

In Ref. [88], we applied a modified Peak Patch algorithm, as outlined in Sec. IV E, to the minicluster initial density field, introduced in Sec III C 2. Our first task was to reproduce some of the HMF and total bound mass fraction found by Ref. [182] using N-body simulations as described in Sec. IV D on the same initial density field.

As mentioned in Sec. IV D, our results from Peak Patch depart significantly from the N-body results at $z < 629$. This is caused by the same scales experiencing different growth (Peak Patch only uses linear growth),[19] and results in a suppression in the number of low mass halos as a small number of large halos come to dominate the total box size. We therefore conservatively only consider the HMF to a minimum redshift of $z = 629$, where the box scale is strictly linear.

However, while the halo number statistics are significantly affected for $z < 629$, the concentrations are affected less so. This is because, as discussed, the $C(M)$ normalisation follows the growth, and the linear and quasi-linear growth only depart by $\mathcal{O})(10\%)$ even at $z = 99$. This can be understood by considering that the formation redshifts of surviving low mass halos (those not swallowed up by spurious large halos) are not affected; $C(M)$ is not a number statistic. Therefore, we still fit the concentrations of the halos by Peak Patch to those simulated by Ref. [87] at $z = 99$, this also being the only redshift at which such a comparison can be made. These differences are explored further in Appendix A.

Much of the following subsections have been taken directly from sections I wrote for Ref. [88].

A. Reproducing N-Body results with Peak-Patch

In Fig. 39 we present the calculated HMFs at seven different redshifts together with the results from Ref. [87] in which the same initial conditions are simulated using traditional N-Body techniques.

Qualitatively the results are very similar. Both methods show that the number of objects at all masses increase rapidly over time up to around matter-radiation equality where the distribution falls and broadens to higher masses. We understand this evolution as the initial

[19] If we artificially adopt the N-body quasi-linear growth at low redshift, this improves the agreement.

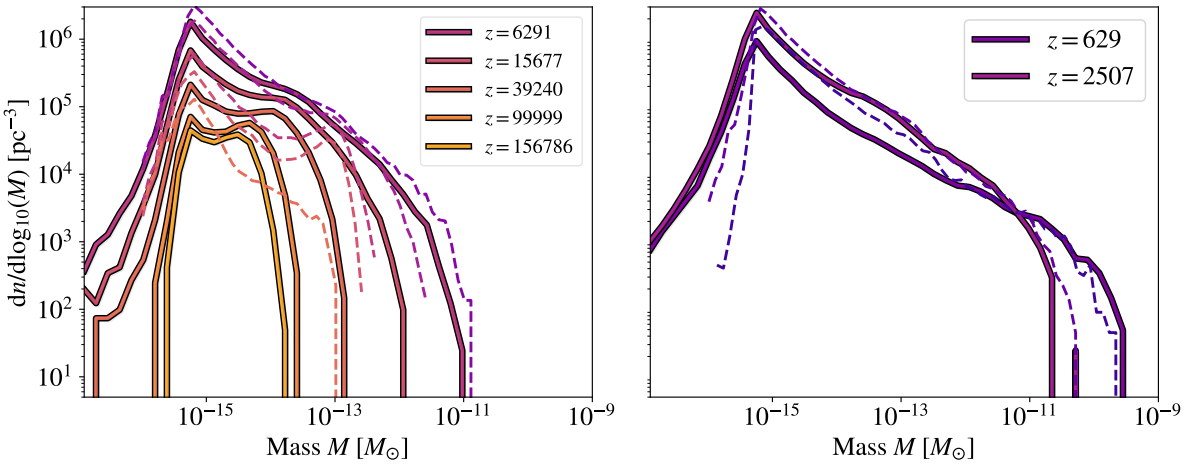

FIG. 39. *Minicluster mass function from Peak Patch.* Solid lines show the HMF calculated using peak-patch with a redshift dependent collapse threshold calculated in Sec. IV. Dotted lines show the HMFs at the same redshifts calculated using N-Body techniques in Ref. [87]. Figure modified from Ref. [88].

collapse of high-density regions followed later by the merging of existing halos. At ($z = 629$), we find that the HMF has a slope of $M^{-0.6}$, this is slightly lower than the value of $M^{-0.7}$ calculated by N-Body. This difference could be a hint at the box beginning to leave the linear-regime as it is consistent with the fact that our method finds more high-mass halos at this redshift. These halos are potentially suppressing the number of low-mass halos as they take up a dominant fraction of the total matter within the box.

We compare the different analytical HMFs calculated assuming Gaussianity and the initial P(k) in Fig. 40. We find that the standard Press-Schechter and Sheth-Torman fitting functions predict very similar HMFs. However, the Peak Patch calculation again produces fewer low-mass halos than predicted using this formalism. Since we can extrapolate the power spectrum to larger scales, the Press-Schechter estimate is immune to problems of going "non-linear" faced by Peak Patch and N-Body calculations. This therefore further suggests that the reduced number of small-halos in our Peak Patch estimate is due to the sizes of the largest halos becoming comparable with the total box volume.

In Fig. 41 we compare the calculated number of halos above different masses as a function of redshift to the value predicted from PS using the standard PS multiplicity function. For each mass range, we see a very rapid initial growth of halos followed by a slow stagnation

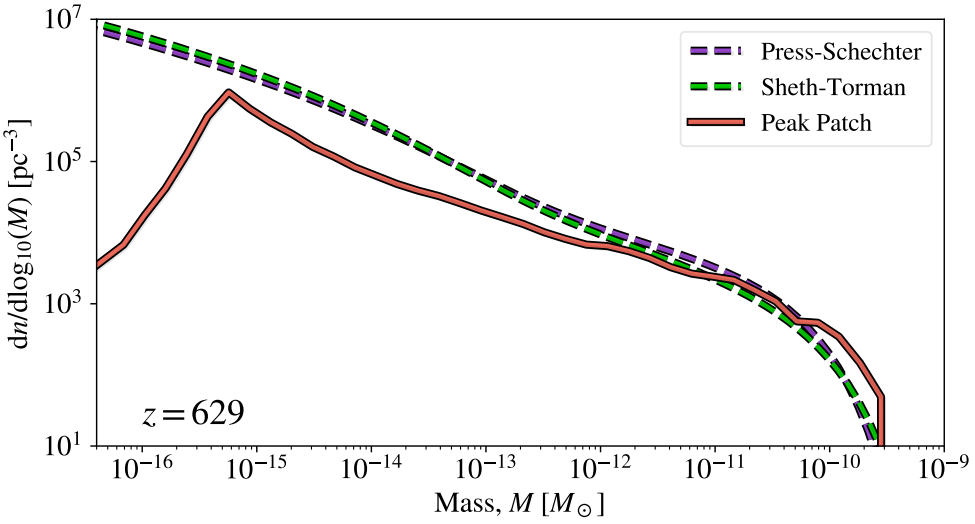

FIG. 40. *Comparison of HMF with PS Prediction.* Solid line indicates the HMF calculated using peak-patch at $z = 629$. Dotted and dot-dashed lines show the Press-Schechter predictions for the HMF at the same redshift using fitting functions PS and ST. Figure modified from Ref. [88].

and then a decline. Interestingly, Peak Patch finds many more low mass objects at early redshifts than are predicted by PS. The N-body simulations also find objects to form faster than PS predicts, however, these objects are still seen much later than in Peak Patch. This is thought to be related to the fact that at early times our density field is highly non-Gaussian whereas the PS approach assumes exactly the opposite to be true.

B. Estimating Halo Concentrations with Peak Patch

Next, we use the results from Peak Patch to build merger trees as discussed in Sec.IV E. An example case of a halo with a final mass of $\sim 10^{-12} M_\odot$ is shown in Fig. 42.

It can be seen from the example case shown that initially, isolated halos grow through the accretion of surrounding matter. Then, there is a period in which many mergers take place. At this point, the total mass of the progenitors stagnates and increases only slowly through accretion and occasional mergers.

It can be seen that, at late times, the progenitor mass becomes slightly noisy and varies a little over time. This is because, when the Lagrangian radii overdensities become large, neighbouring overdensities begin to overlap. Using spherical integral, it comes somewhat difficult to assign mass to particular overdensities in a way that is completely consistent over

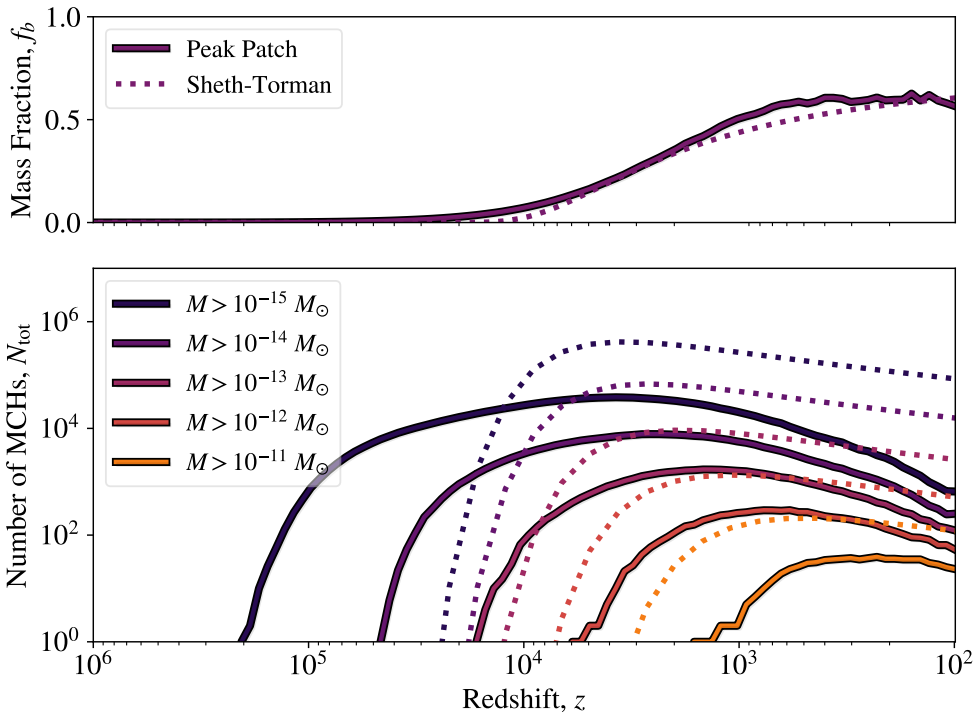

FIG. 41. *Number of Minicluster Halos.* Top: Total fraction of gravitationaly bound mass. Bottom: Total number of miniclusters above mass scales in the range $\{10^{-15}, 10^{-10}\}M_\odot$. Solid lines indicate the values calculated using peak-patch while dotted lines show the values predicted using Press-Schechter. Peak Patch finds a large number of halos to form at high redshift from the strongly non-Gaussian density peaks, consistent with the results of N-body. Figure modified from Ref. [88].

time. However, as can be seen from Fig. 42, this does not significantly impact the overall trend of growth.

Using these merger trees it is then possible to assign a collapse redshift to each halo using the half-mass definition as discussed in Sec. IV. In doing this we can then also estimate the shape of the concentration-mass curve from the true initial density field. The normalisation of the curve is then set by the same fitting parameter of $\kappa_{\rm NFW} = 1.28 \times 10^5$ calculated earlier using Press-Schechter.

The collapse redshift was calculated for the halos found by Peak Patch using three a threshold fraction of $f = 0.01$ however we found that, unlike with the PS predictions, the choice of threshold fraction only makes a significant impact for masses above the peak mass of $M \approx 10^{-11} M_\odot$.

Using the same fitting parameter calculated for using the PS predictions for $C(M)$, we

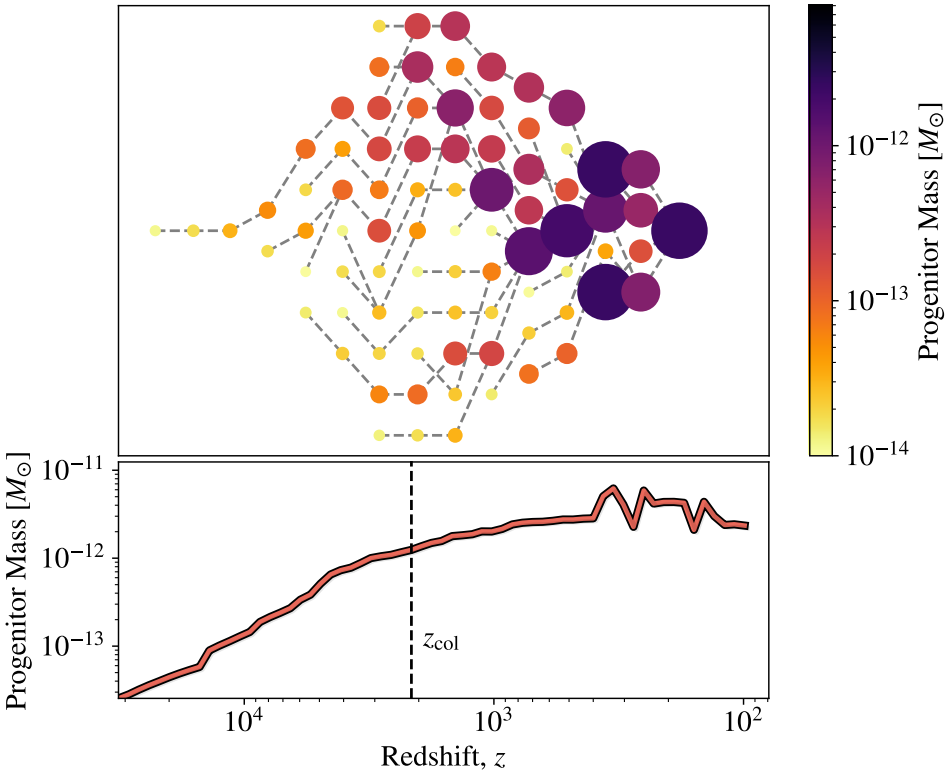

FIG. 42. *Example merger tree.* Top: Merger tree for a halo with a final mass of $2.35 \times 10^{-12} M_\odot$ showing all progenitors with a mass greater than $10^{-14} M_\odot$. The radius of the circles is proportional to the effective radius of the progenitor. Bottom: Total mass of progenitors that have a mass greater that 0.01 times the final halo mass. The collapse redshift is then defined as the point at which this total equals half of the final mass, as introduced by Navarro et. al in Ref .[170].

find a concentration distribution as shown in Fig. 43. It can be seen that for masses above $\sim 10^{-12} M_\odot$ the Press-Schechter and Peak Patch approaches make comparable predictions for a large proportion of the miniclusters. However, Peak Patch also produces a large number of halos with a very low concentration at all masses up to $\sim 10^{-11} M_\odot$.

Finally, given the success of our calibrated analytical approach in fitting both the N-body and Peak Patch results, we can extend our PS calculation to $z = 0$ to predict the concentration parameter of the axion miniclusters today. Doing so, we find a maximum value of 7.9×10^4 at $M = 2.0 \times 10^{-13}$ as shown in Fig. 43.

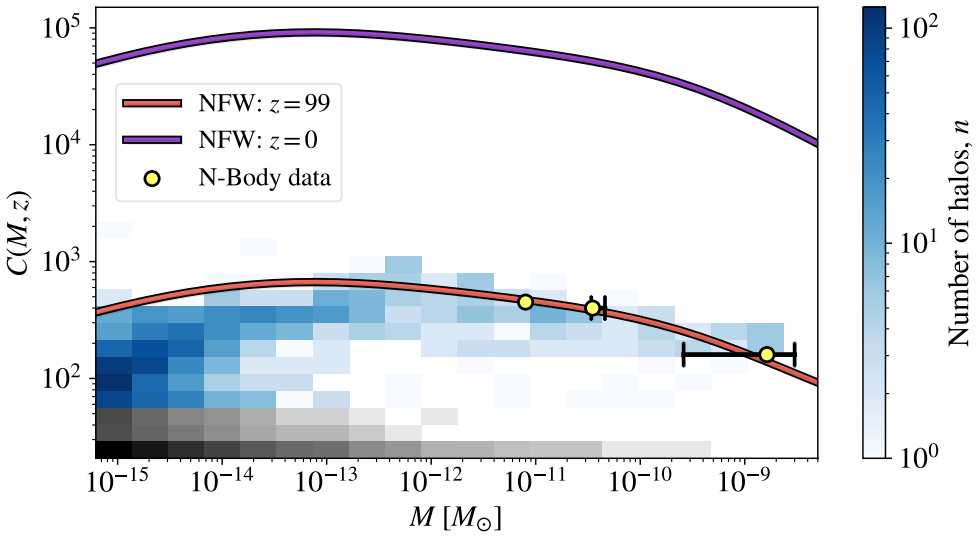

FIG. 43. *Minicluster Concentrations.* The Colour map indicates the concentration parameters calculated using Peak Patch merger trees. The solid green and dashed red lines show the concentrations from the power spectrum, assuming Gaussianity. The grey colour map shows halos calculated to have concentrations less than 50. Since these objects have only just formed it is thought that they have not had enough time to become as dense as the NFW prediction. Figure modified from Ref. [88].

C. Microlensing of Axion Miniclusters

Now that we have an estimate for the minicluster concentration-mass relation, we can compare this to the halo parameters required for microlensing that we calculated in Sec. VI. In Fig.44, we see that the minicluster concentration extrapolated to today $c(M, z = 0)$ falls short of the region in which lensing can occur by around two orders of magnitude. When we consider wave effects, the predicted concentration curve is even further away from the required density.

Here, we have used the concentration calculated assuming Gaussianity in a PS-style calculation also shown in Fig. 43. As we see from the $z = 99$ case, this is akin to a mean halo concentration. We, therefore, expect there to be a statistical spread from this curve.

It is possible to estimate the maximum possible concentration for a halo formed via hierarchical structure formation. Recall from Sec. V A that a halos scale density is proportional to the density of the universe at the redshift at which it collapsed. This means that halos

that collapse earlier have higher concentrations. We can therefore estimate the maximum possible concentration as a function of mass by finding the first redshift at which a halo of each mass forms and taking this to be the collapse redshift.

Using PS, we can estimate the halo number density $n(M)$ as a function of halo mass. Doing so, we can find the maximum mass $M_{\rm max}$ we would expect to find within a volume equal to the size of our box $V_{\rm box}$ by solving $n(M_{\rm max})V_{\rm box} = 1$. We can then relate each of these masses to a maximum concentration $c_{\rm max}(M)$ calculated from Eq. 167 as shown in Fig. 44.

We chose to use PS to calculate this maximum curve for constancy with our "total" concentration curve. We see that this curve also falls short of the parameter space which allows for gravitational microlensing, however only slightly. Recall from Sec. V D that a smaller axion mass gives rise to larger miniclusters. It is therefore likely that such an axion would cause the maximum concentration curve to enter the region for which $\mathcal{R} > 0$. However, it is less likely that it can enter the region for which $M_{\rm eff} > M_{\rm min}$ without conflicting with existing constraints on the axion mass outlined in Sec. III.

Additionally, as we saw from Fig. 41, PP calculates halos collapsing much earlier than PS. This means we might expect the maximum concentration to be higher than that calculated here. However, as we see from Fig.43, the spread of concentrations calculated from PP deviates very little from our PS calculation. Comparing this to our maximum concentration curve, it feels safe to assume that this safely captures all possible concentrations with room to spare. The validity of this assumption will be further strengthened in the next section.

This might lead us to assume that microlensing with miniclusters is not possible. However, so far we have assumed that all miniclusters exhibit NFW profiles. This need not be the case. While Ref. [87] showed the miniclusters are well described an NFW profile, they only looked at halos with masses $\gtrsim 10^{-11} M_\odot$.

It is therefore possible to imagine that smaller miniclusters have different density profiles. Additionally, many of these light halos will have only recently formed and therefore not have had a chance to undergo many significant mergers. It is therefore plausible that, having formed primarily from the accretion of background matter, their profiles might look more like a single power-law described in Sec. V B.

Another important consideration is minicluster substructure. Ref. [87] showed that miniclusters are not perfectly spherically symmetric objects but instead typically have a rich

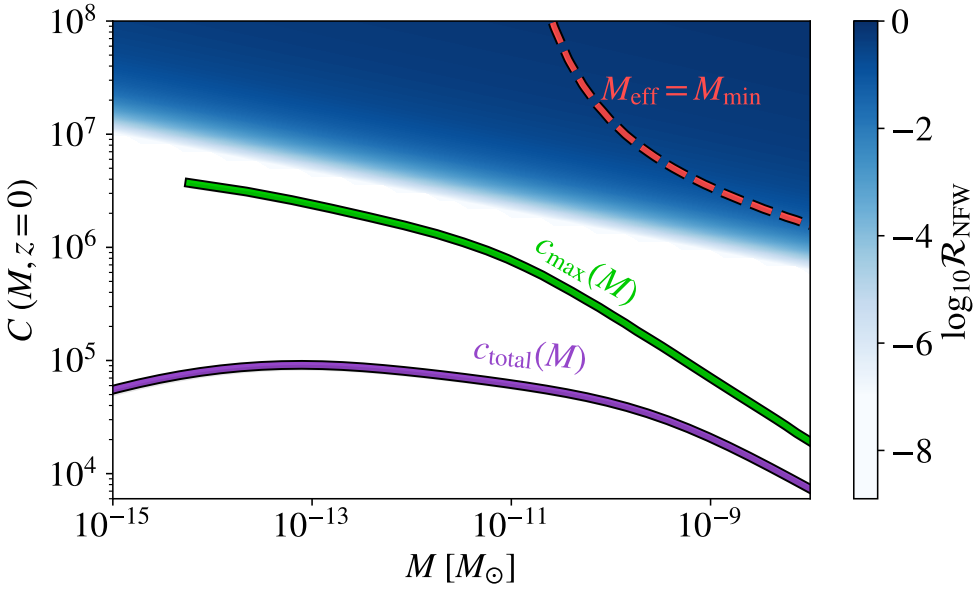

FIG. 44. *Miniclusters microlensing ability.* Predicted mean minicluster concentration (Purple) and maximum minicluster concentration (Green) at $z = 0$. Both fall short of the blue region in which halos are dense enough to produce microlensing and even further short of the minimum effective mass requirement from wave effects. Figure modified from [91]

substructure. This substructure, by definition, collapsed before the parent halo. As a result, if these subhalos have NFW profiles, their concentrations might be significantly higher than that calculated for the bulk halos shown in Fig. 43. Alternatively, these objects could also turn out to look more like power-law profiles.

To investigate these possibilities, in the next section, we explore how we can use the results from Peak Patch to locate objects that collapse very early in the N-body simulations performed in Ref. [87]. By tracking these objects forwards to today, we will investigate what impact if any this early collapse has on their final structure. We also use this data to make predictions about the axion stars we would expect to be present at the centres of each of these halos (and subhalos). We will then determine whether we expect these objects will be able to produce microlensing signals.

VIII. FIRST MINICLUSTER STRUCTURES

In this section, we will combine our results from Peak Patch with the N-Body data from Ref [87] to identify and study the structure of the densest miniclusters as they evolve through cosmic time. We will attempt to look for trends between the initial density field and the final halo structure. Finally, we will calculate whether the structure formed from these densest structures are able to produce microlensing signals. Much of this section has been modified from Ref. [91].

A. Tracking Early Collapsing Objects

We saw in the previous section that Peak Patch can reproduce the halo mass function calculated using traditional N-body methods with a high degree of agreement. However, the algorithm is also very good at predicting the locations of halos, particularly in Lagrangian (undisplaced) coordinates.

A comparison between this modified PP and N-body is presented in Fig. 45. The left and right panels show projection plots of the N-body particle density in Lagrangian and Eulerian coordinates respectively for the 400 largest halos found in our simulations using the SUBFIND halo finder introduced in Sec. IV D [166, 167]. The locations of these halos as found by SUBFIND are shown in blue. The most likely equivalent halos in the PP data are shown in red. We see that the PP estimates are in close agreement with N-body, particularly in Lagrangian coordinates. This makes sense since PP works on the initial density field. In Eulerian space, the sizes and masses of the halos are well estimated by PP, while the locations are systematically offset. This can be understood since we use only first-order Lagrangian displacements. These results confirm the accuracy of our modifications to PP described in Sec. IV E for producing accurate halo catalogues in minicluster cosmologies with isocurvature initial conditions, large non-Gaussianities, and collapse during the radiation epoch (a similar comparison for standard ΛCDM cosmologies was shown in Ref. [86]).

Since Peak Patch is particularly good at finding halos in the initial density field, we can use this to mark particles in the initial N-body distribution which we expect to later be contained within collapsed halos.

As discussed previously, most of the halo mergers take place after matter-radiation equal-

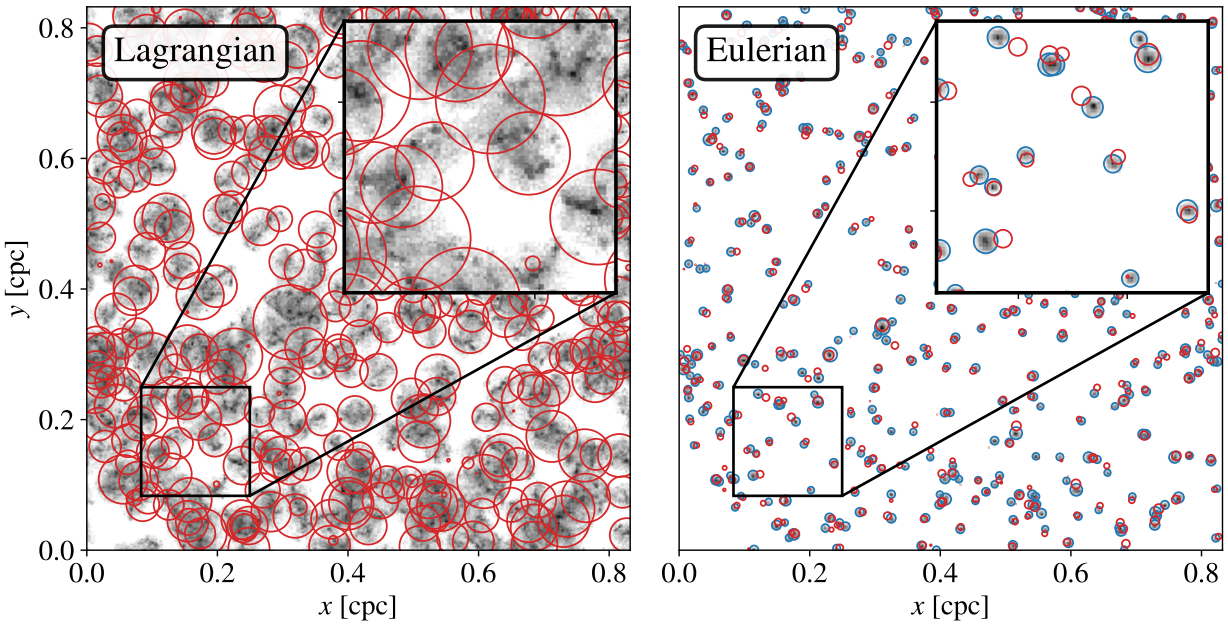

FIG. 45. *Peak-Patch comparison with Nbody.* Projection plot of the N-body particles (black) contained within the 400 largest halos located using the SUBFIND halo finder at a redshift $z = 3976.5$ in Lagrangian coordinates, without displacement (left) and Eulerian coordinate, with displacement (right). Blue circles indicate the size and extent of the halos as found using SUBFIND. Red circles indicate the most likely equivalent from the Peak-Patch data.

ity. Therefore, if we want to find the objects which may later go on to be sub-halos, we have to identify objects collapsed before this time. The closest snapshot to this for which we have N-body data is at $z = 3976.5$ as shown in Fig.45 above.

However, in the previous section, we saw that the density profile of a DM halo is also dependent on its collapse redshift. Therefore we look for similar trends in the sub-halos. Here, however, we go slightly further and connect this to the initial density field by calculating the initial density field related to this collapse redshift via Eq. 175. We denote this initial density $\delta_{\rm col}(z)$, where z is the redshift at which the collapse redshift was calculated.

Samples are chosen by making a uniform sample in $\delta_{\rm col}(z)$-mass space in order to ensure that the full spectrum of objects are well represented.

We track these halos by first noting the IDs of particles in the initial ($z \sim 10^6$) N-body particle distribution contained within the Lagrangian sphere for each of our objects predicted by PP to have collapsed by $z = 3976.5$.

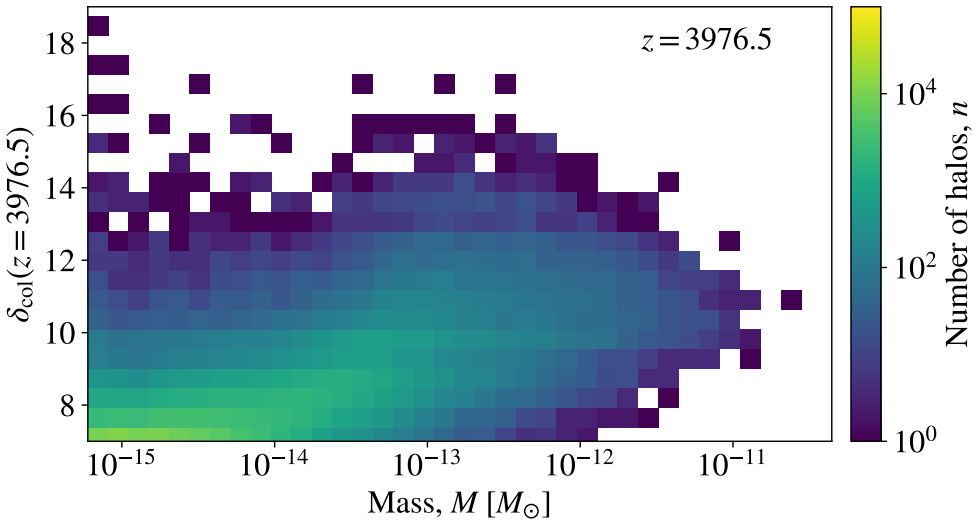

FIG. 46. *Initial overdensities of halos at* $z = 3976.5$. Collapse redshifts of halos predicted using Peak Patch calculated by building merger trees as outlined in Sec. IV E. These redshifts are then related to an initial overdensity from Eq. 175.

We then locate these particles again at later snapshots and determine their point of maximum density using a kernel density estimation (KDE) algorithm (See Appendix C for further details). Taking this point of maximum density to be the centre. We then "collect" these particles by working radially outwards this point until the desired mass is found.

We estimate the final mass of an object by assuming that from $z = 3976.5$ the halos grow only by accreting matter from the background. As such, we predict that the mass will evolve as

$$M = M(z' = 3976.5)\frac{1 + 3976.5}{1 + z}. \tag{221}$$

Using this method, we locate and track halos to $z = 3976.5$ and $z = 99$. We will analyse the density profiles of the samples at both of these redshifts. We will also calculate additional properties of the halos at $z = 99$ and use this to make estimates about their ability to produce microlensing.

In order to estimate how many of our samples are subhalos, we compare the location of the centre of each sample with their nearest halo found using SUBFIND. If the centre of the nearest SUBFIND halo is closer to the centre of a sample than the radius of that sample, we assume that it is a full halo. Otherwise, if the distance is greater, we assume that the sample is a sub-halo. Doing this, we find that around a third of our samples are sub-halos

with the remaining two thirds being ordinary miniclusters.[20]

B. Properties of Tracked Objects

1. *Survival rate*

It is important to note that not all of the objects we track will survive until $z = 99$. Many will be completely disrupted through gravitational interactions with larger halos. In order to analyse the survival of these objects, we define a metric called the index matching fraction f_m. This is the fraction of particles that were marked in the initial density field which are found in our new sample at a later redshift.

In Fig. 47, we see that halos with a large index matching fraction tend to have a much more well-defined density profile. We, therefore, restrict our analysis of halos at $z = 99$ to samples with $f_m \geq 0.75$. Interestingly, we find that a lower index matching fraction is required for our samples to have a well-defined density profile at $z = 3976.5$. Therefore, at this redshift, in order to maximise the number of samples, we only restrict our analysis to samples with $f_m \geq 0.5$. It should be noted that these thresholds are hand-picked and are therefore rather arbitrary.

We start by investigating the trends in this survival metric as shown in Fig. 48. We see that there is a strong correlation between the index-matching fraction and the sample mass. This makes sense as larger objects have a deeper gravitational well which protects them from disruption.

From the two-dimensional histogram, we see that for sample masses $\gtrsim 2 \times 10^{-13} M_\odot$ there might be a slight trend in which higher initial overdensities lead to a higher survival rate. This also makes sense as we expect objects that collapse earlier should be more highly concentrated. This, as shown in Ref. [77] in the context of stellar disruptions, should make halos more resistant to disruption.

[20] It should be noted that this estimate assumes that SUBFIND has correctly identified all full-halos.

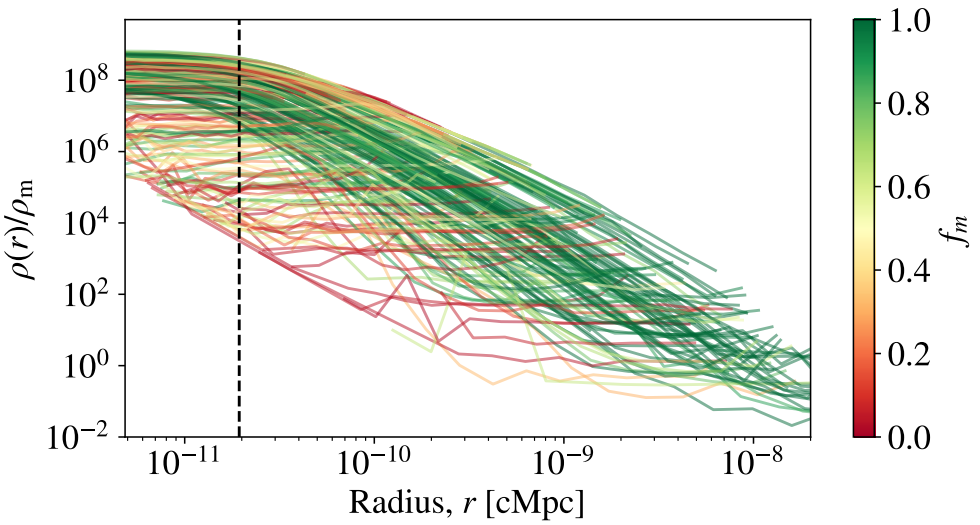

FIG. 47. *Demonstration of survival metric.* Random selection of 300 N-body particle samples at $z = 99$ for $f_m > 0.02$. Those with a high index matching fraction f_m have much more well defined density profiles. Gray shaded region indicates radii smaller than the softening cut-off. Taken from Ref. [91].

2. *Virialisation*

Recall from Sec. II A that once a halo has relaxed into a stable state it is said to be virialised. This is defined to have occurred when

$$2K - W = 0. \tag{222}$$

where K and W are the halo's total kinetic and potential energy respectively.

The total kinetic energy of a halo can be straightforwardly calculated from the N-body particle velocities as

$$K = \frac{1}{2}\sum_i m_p v_i^2, \tag{223}$$

where m_p is the N-body particle mass and v_i is the velocity of the i-th particle relative to the mean velocity of the halo.

The total gravitational potential is given by the sum of potentials between all pairs of particles

$$W = -G\sum_{1\le i\le j\le N}\frac{m_p^2}{|r_i - r_j|}. \tag{224}$$

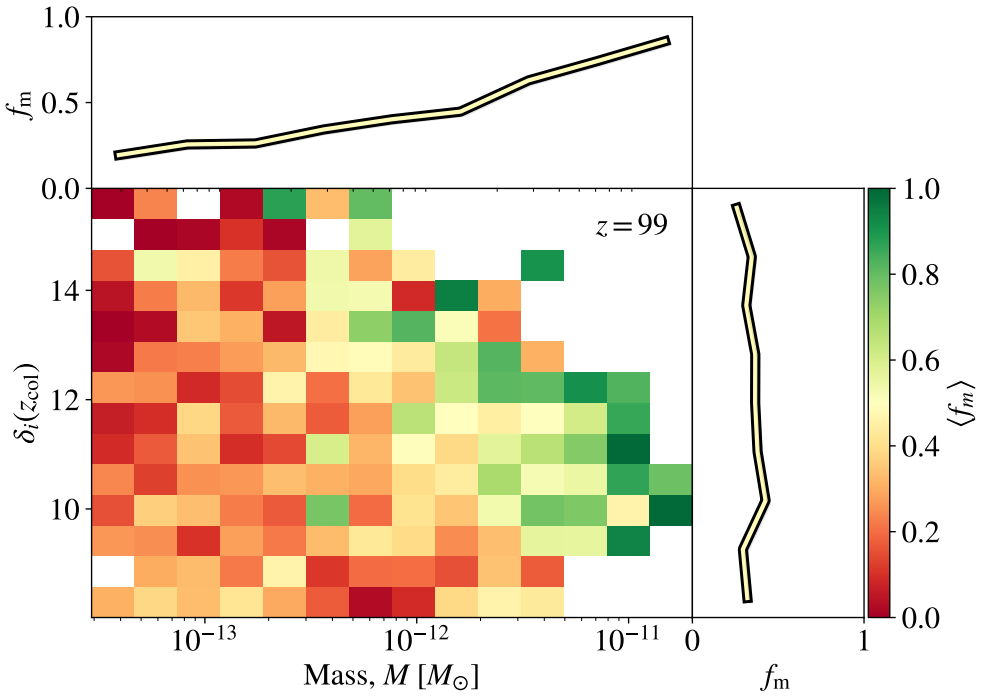

FIG. 48. *Trends in halo survival.* Two-dimensional histogram for index matching fraction as a function of mass and $\delta_i(z_{\rm col})$ for all 1028 sample halos at $z = 99$. Top: Index matching fraction as a function of sample mass M. Right: Index matching fraction as a function of $\delta_i(z_{\rm col})$.

However, since there are so many particles this is computationally expensive to calculate. Instead, we bin the particles in a three-dimensional grid with $n_{\rm bin}^3$ cells. We then calculate the sum of the potentials between each pair of these cells. As shown in Appendix D, this calculation converges to a single value with an increasing number of cells. We find that for all relevant masses, the calculated potential changes very little for $n_{\rm bin} > 25$. We therefore use $n_{\rm bin} = 25$ to calculate the potentials of all of our samples. We start by looking at how the level of virialisation correlates with our halo survival metric f_m for our final halos at $z = 99$ as shown in Fig. 49. We see that samples with a high value of f_m are well virialised or are slightly dominated by the gravitational potential. This is as we would expect as we have seen from Fig. 47 that these samples have well-defined density profiles with dense centres and hence a deep potential well. This also helps to demonstrate the ability of index matching fraction f_m to act as a metric for halo survival.

However, we also see that there is also a group of halos with a high index matching fraction are very poorly virialised in the top right corner of Fig. 49. When we plot the density profiles

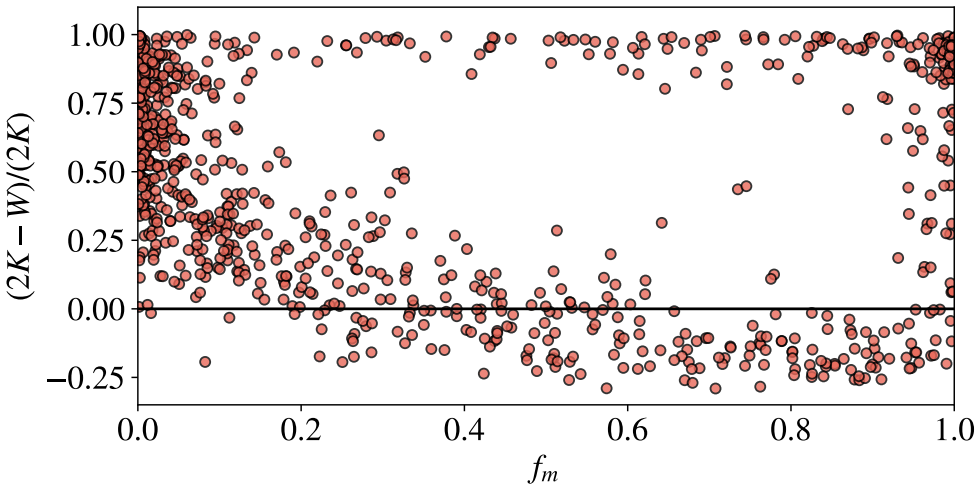

FIG. 49. *Virialisation and index matching fraction.* Relative level of sample virialisation as a function of index matching fraction for 1028 samples at $z = 99$.

of all of these high f_m halos, we see that those which seem to be poorly virialised include large amounts of *unvirialised* background matter beyond the limits of the central halo. This implies that, for these halos, our mass estimate from Eq. 221 overestimates the final mass. This causes us to collect more particles in our sample than are actually contained within the virialised halo.

On the other end of the f_m spectrum, since there are so few of the particles that we marked on the initial density field, the location of the sample is almost completely arbitrary. Samples are therefore able to take on the full range of possible virialisation values which is exactly what we see from Fig. 49.

We also investigate the relationship between the level of virialisation of our halos and their average overdensity Δ. Typically, we expect that within their virial radius, halos have an overdensity of $\Delta = 200$ (Or similarly from, for example, Eq. 159). However, as we see from Fig. 50 the halos which have a virial parameter closest to zero instead have overdensities $\Delta \sim 10^5$. This is because, despite the collection of high f_m-low virialisation samples discussed previously, the masses of most of our samples are much smaller than their virial masses. This tells us that most of our samples are from the dense cores of dark matter halos.

We also see that for samples with low values of f_m, those that are fairly well virialised also tend to have a large average overdensity. This suggests that the sample is at the centre

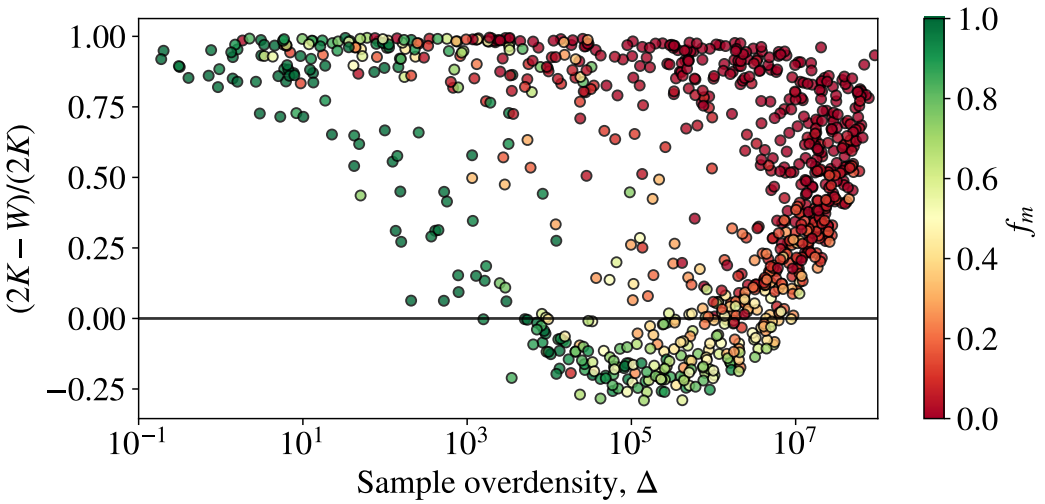

FIG. 50. *Virialisation and average overdensity. Relative level of sample virialisation as a function of average sample overdensity* Δ *for 1028 samples at* $z = 99$*. Colour indicates the samples index matching fraction.*

of a large halo which could suggest that the original halo whose particles we tracked have been disrupted/consumed by a larger halo.

3. Density profiles

To compare the density profiles of our sample halos to theory, we want to plot all of the profiles on a single curve. This can be done for both NFW and PL profiles. For NFW profiles we can do this by plotting $\rho(r)/\rho_0$ against r/r_s, and for PL profiles by plotting $\rho(r)/\rho_0$ against $r/R_{\rm vir}$. We can therefore compare the profiles of all of our profiles to a single "predicted" curve as shown in Figs. 51 and 52 for $z = 3976.5$ and $z = 99$ respectively. However, to do this we need to find the "virial" radius for each of our halos and, for comparing to NFW, the halo concentration. As done in Ref. [88] we take the virial radius to be $R_{\rm vir} = R_{200}$ where R_{200} is the radius which contains a sphere with a total overdensity $\Delta = 200$.

However, in some of our samples, the maximum particle radius is smaller than R_{200}. This is particularly true for our samples at $z = 99$ because we under-predict the mass growth from $z = 3976.5$. This under-prediction implies that these objects gain a significant proportion of their mass from mergers as opposed to only from the accretion of the background. For these samples, we extrapolate the radial overdensity profile $\Delta(r)$ as a power-law to larger

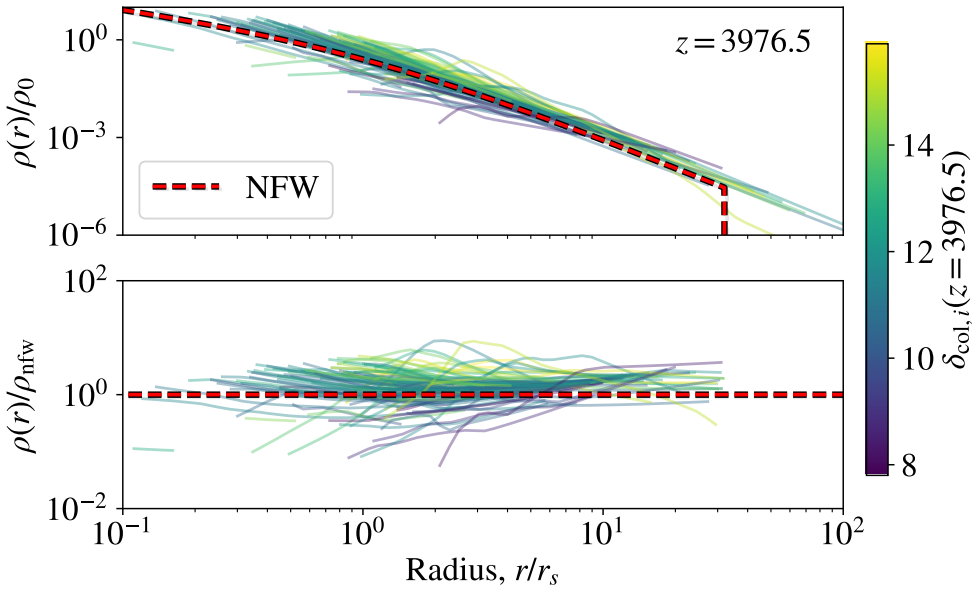

FIG. 51. $z = 3976.5$ *NFW comparison.* Showing 100 samples for which matching-fraction $f_m > 0.5$ with line colours showing $\delta_{\rm col,i}(z = 3976.5)$ for each sample. Top: Radial density profile compared to the NFW prediction given by our $c(M, z)$ prediction shown in Fig. 27. Bottom: Ratio of N-body profile to NFW prediction.

r. We choose to extrapolate $\Delta(r)$ instead of $\rho(r)$ as this profile is less "noisy" since it is an average over a larger volume.

As mentioned previously, the halo concentration is dependent on the halo virial mass. Therefore, to find the predicted halo concentration, we need an estimate for the halo virial mass. We do this by calculating the mass contained within R_{200} for each halo. Again, since some of the samples are smaller than R_{200}, we use an extrapolation of the internal mass function $M(r)$. We can then extract our estimate for the halo concentration from our two-dimensional interpolation of Fig. 27.

We start by comparing the density profiles to the NFW profile predicted for their calculated virial mass. We see from Figs. 51 and 52 that most of our profiles match their NFW prediction very well. For $z = 99$ we can see clearly the presence of a split power-law profile. Within the resolution of the N-body data, there is no evidence of profiles that have a slope much steeper than $\sim r^{-1}$ at radii smaller than the predicted r_s. We, therefore, have no reason to favour a PL profile model for these samples over the NFW profile.

However, as shown in Fig.53 almost 80% of our samples have scale radii greater than our

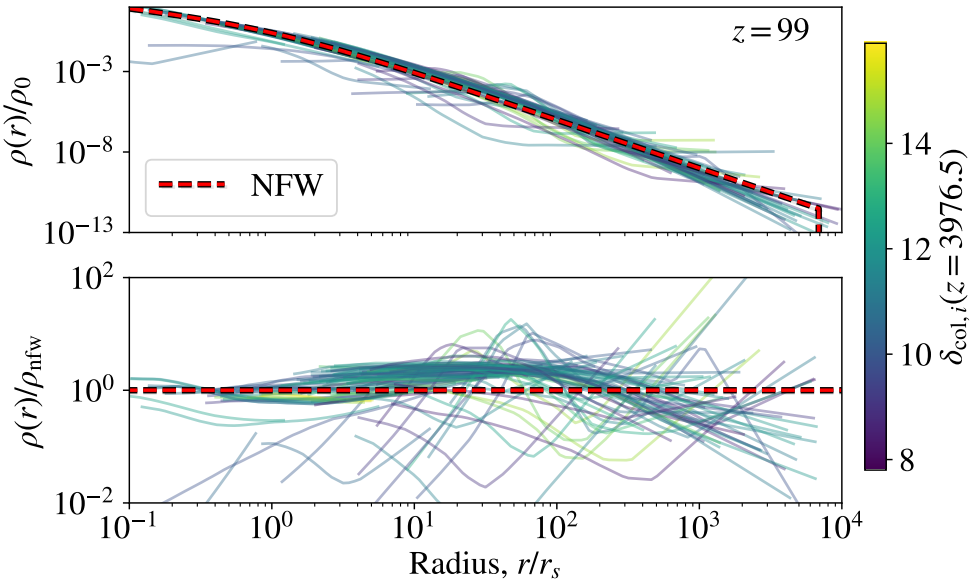

FIG. 52. $z = 99$ *NFW comparison.* Showing 100 samples for which matching-fraction $f_m > 0.75$ with line colours showing $\delta_{\rm col,i}(z = 3976.5)$ for each sample. Top: Radial density profile compared to the NFW prediction given by our $c(M, z)$ prediction shown in Fig. 27. Bottom: Ratio of N-body profile to NFW prediction.

smoothing length cut-off. For these halos, since r_s is unresolved, it is, therefore, possible that these halos instead have a single power law.

Such a distinct split power law is not so obvious for our samples at $z = 3976.5$. We find that at this redshift halos are also fairly well described by a single power law. This is despite around three quarters having predicted scale radii which are larger than the softening cut-off.

Therefore, for all halos at $z = 3976.5$ and for halos at $z = 99$ whose predicted scale radii are smaller than the softening cut-off, we also compare the profiles to the PL prediction derived in Sec. V B. In order to compare profiles to a single PL curve, we first calculate the average slope by using a least-square fit to fit a single power law to each profile. We show the calculated slopes as a function of $\delta_{{\rm col},i}(z = 3976.5)$ in Fig. 54.

We see that profiles at $z = 99$ are distinctly steeper with an average slope of $\alpha \approx 2.9$ than those at $z = 3976.5$ with an average slope of $\alpha \approx 2.4$. This makes sense since, as we saw from Fig. 53, the halos at $z = 3976.5$ have a larger comoving scale radius. Therefore, assuming a split power law like NFW, the shallower slope below the scale radius takes up a larger proportion of our sample. This reduced the average slope of the halo's density

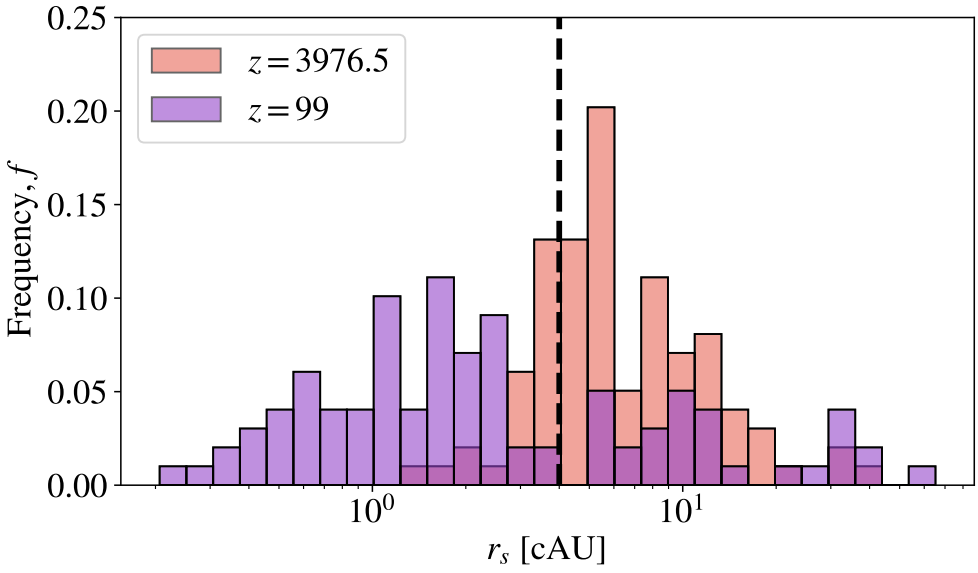

FIG. 53. *Scale radii.* Frequency density $f = n/\sum n$ of predicted scale radii of halos at $z = 3976.5$ (red) and $z = 99$ (purple). Dashed line shows smoothing cut-off at 4AU.

profile. Similarly, for the halos at $z = 99$, since the scale radius is not resolved the sample is dominated by the outer $\sim r^{-3}$ part of the density profile.

We also see that for our samples at $z = 3976.5$, halos with a higher initial overdensity at collapse have steeper profiles. This is also consistent with our understanding of the relationship between a halo's concentration and its collapse redshift. Halos with a larger initial density at collapse by definition (see Eq. 175) have larger collapse redshift. Therefore, as discussed in Sec. V A, we expect these halos to have larger concentrations and hence smaller scale radii. Again, this means that a larger proportion of the density profile for these samples is composed of the outer $\sim r^{-3}$ slope which increases the average slope size.

Conversely, we see that there is no such trend for the samples at $z = 99$. However, we know from the previous section that the density profile of these halos is dependent on their collapse redshift. However, in the previous section, we considered the collapse redshift *calculated at* $z = 99$. The fact that there is not a clear correlation between the density profile at $z = 99$ and the collapse redshift *calculated at* $z = 3976.5$ suggests that there is similarly little to no correlation between $z_{\rm col}(z = 99)$ and $z_{\rm col}(z = 3976.5)$.

This contradicts the commonly held assumption that a minicluster's structure is dependent on the initial overdensities ($\delta \gtrsim 1$) of axion minicluster seeds which seeded its formation

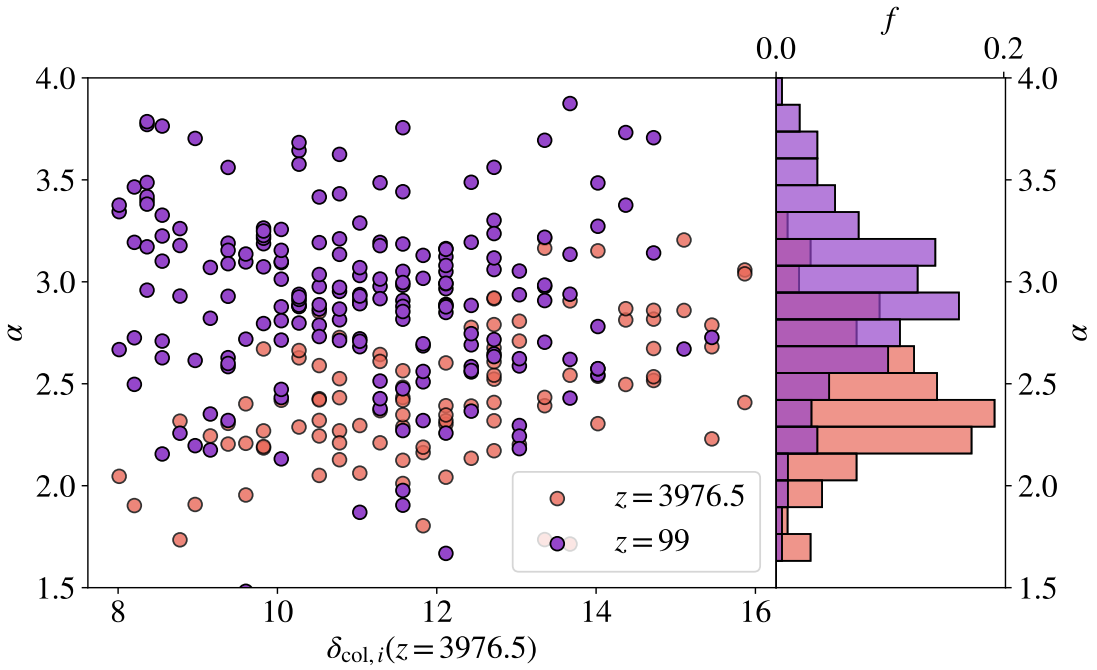

FIG. 54. *PL slopes.* Left: Single power-law slopes α calculated using a least-square fit for $z = 3976.5$ (red) and $z = 99$ (purple) as a function of $\delta_{\mathrm{col},i}(z = 3976.5)$. Right: Frequency density $f = n/\sum n$ of the power-law slopes for $z = 3976.5$ (red) and $z = 99$ (purple).

[77, 79]. Instead, it seems that the density is much more dependent on its collapse redshift and hence its mass growth history. This is linked to the initial overdensity of the whole halo from Eq. 175 however, the overdensities of the first minicluster seeds are completely washed out.

Using the calculated mean power-law slopes, we also compare the density profiles of all samples at $z = 3976.5$ and samples at $z = 99$ whose scale radius is smaller than the softening cut-off to a single power law as shown in Figs 55 and 56 respectively.

As with our comparison to the predicted NFW profile, we find M_{200} for each halo. Using this, we can calculate the expected halo radius r_0 using the Kolb & Tkachov average density equation given by Eq.173. However, we find that the resulting radii tend to be around half the size of our computed R_{200}. This, in turn, causes us to estimate ρ_0 incorrectly. This is not a problem if we instead take $r_0 = R_{200}$.

By eye, the density profiles of our samples at $z = 3976.5$ seem to agree slightly better with the predicted profile as a single power-law. However, comparing the relative differences in the bottom panels of Figs. 51 and 55 it is not clear that either matches either prediction

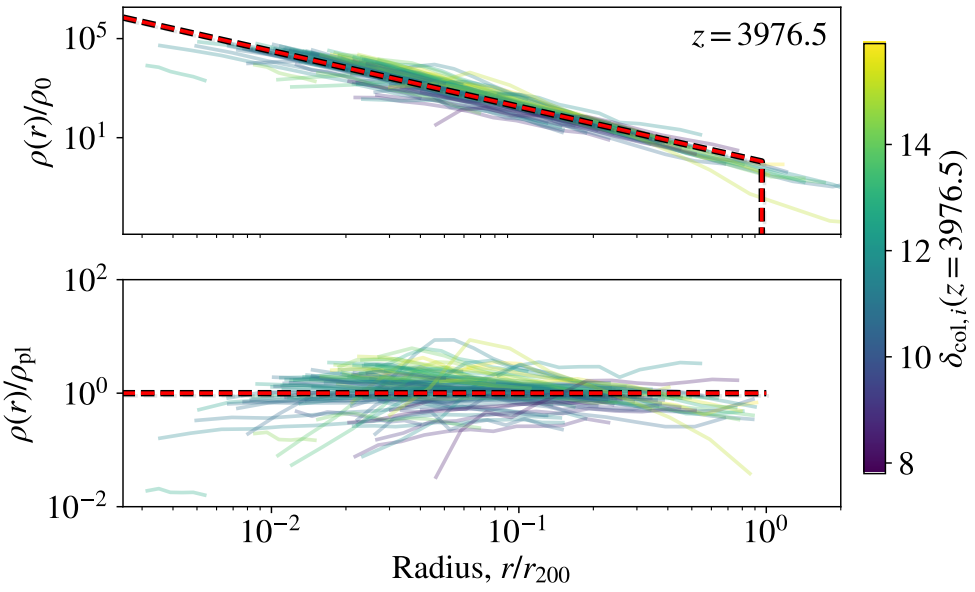

FIG. 55. $z = 3976.5$ *PL comparison.* Showing 100 samples for which matching-fraction $f_m > 0.5$ with line colours showing $\delta_{\rm col,i}(z = 3976.5)$ for each sample. Top: Radial density profile compared to the PL prediction with a slope of $\alpha = 2.5$. Bottom: Ratio of N-body profile to PL prediction.

better.

Conversely, for samples at $z = 99$, it appears that most halos are shallower than the single power-law at small radii. This is consistent with these halos having a split power-law profile such as NFW in which the inner power-law is shallower even though the scale radius is not resolved. This is because the gradient of the density profile already begins to turn over at radii slightly larger than the scale radius.

For completeness, even though these profiles appear slightly better described at small radii by the NFW prediction, in Sec. VIII C we will calculate their ability to produce microlensing signals using both their NFW and PL profile predictions.

However, as discussed previously, in order to correctly calculate whether axion miniclusters can produce microlensing, we need to consider their central axion star as this provides a low-radius cut-off to the density profile. In the next subsection we will estimate the properties we would expect the axion stars for our samples to have from the N-body data.

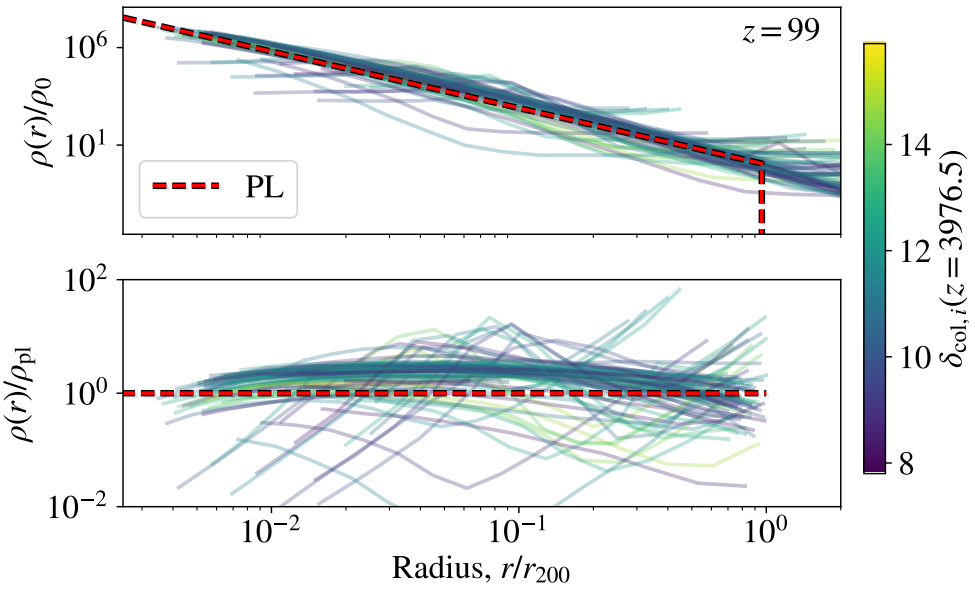

FIG. 56. *$z = 99$ PL comparison.* Showing 100 samples for which matching-fraction $f_m > 0.75$ with line colours showing $\delta_{\rm col,i}(z = 3976.5)$ for each sample. Top: Radial density profile compared to the PL prediction with a slope of $\alpha = 2.9$. Bottom: Ratio of N-body profile to PL prediction.

4. *Virial velocity and axion stars*

Since axion stars are a wave-based phenomena, they are not resolved in our N-body simulations such as those performed by Ref. [182] which produced the data presented here. However, as discussed in Sec. V C, the mass of an axion star is proportional to the virial velocity of an axion minicluster. We can therefore use Eq. 189 to estimate mass and hence the radius from Eq. 190 of the axion star which would be present at the centre of the minicluster.

The virial velocity $v_{\rm vir}$ is the modal relative velocity of the particles contained within the virial radius of a halo. However, we saw in Sec. VIII B 2 that since the masses of our tracked halos have often been underestimated, their radii are typically smaller than the virial radius. However, as shown in Appendix D, the virial velocity is primarily defined by the velocities of particles in the centre of the halo. In fact, we find that over the full radius of a halo the virial velocity typically varies by only $\sim \mathcal{O}(2)$. The difference between the values calculated for our samples and their halos "true" virial velocity should therefore be much smaller than this.

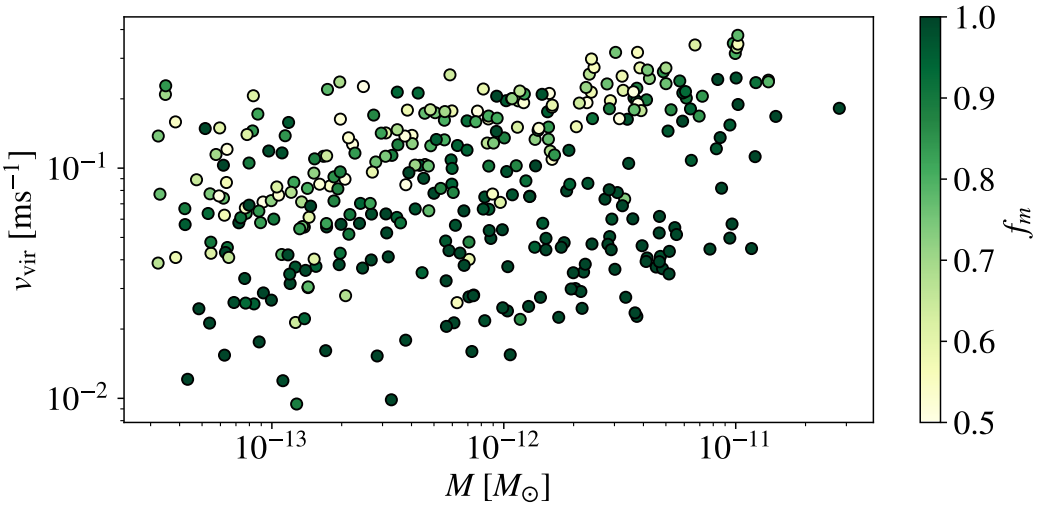

FIG. 57. *Virial velocity and sample mass.* Calculated for N-body halo samples with $f_m > 0.5$.

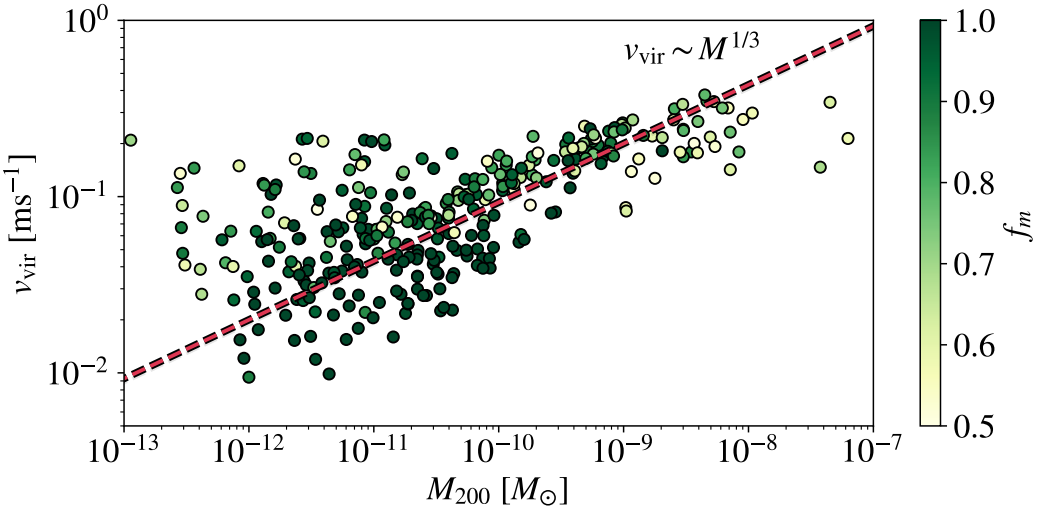

FIG. 58. *Virial velocity and virial mass.* Calculated for N-body halo samples with $f_m > 0.5$.

The virial velocity for all of our samples at $z = 99$ with $f_m > 0.5$ are shown in Fig. 57. The relationship between $v_{\rm vir}$ and M might appear a lot weaker than we would expect. However, this is because our sample mass is only weakly related to the virial mass of each object. We can estimate the virial mass as M_{200} by again extrapolating our density profile until we have an overdensity of 200. Calculating this for each of our samples, we see from Fig. 58 that this is much closer to the $v_{\rm vir} \sim M^{1/3}$ relation that we expect.

We see from Fig. 57 that some of the estimated virial masses are up to four orders of magnitude larger than the sample mass. This is because, as shown in Fig. 50, some

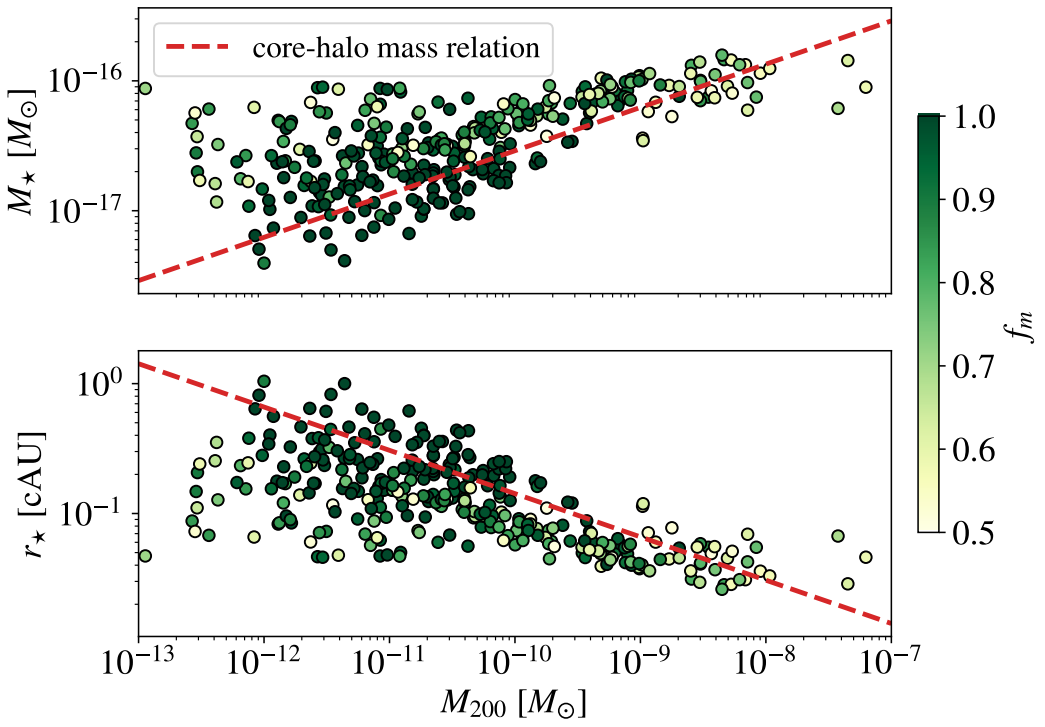

FIG. 59. *Axion star mass and radius.* Estimated by calculating $v_{\rm vir}$ for N-body halo samples with $f_m > 0.5$ and substituting into Eqs. 189 and 190 respectively.

of the samples are very overdense $\Delta \sim \mathcal{O}(10^5)$. Therefore, we have to extrapolate to a comparatively very large radius to reach an internal overdensity of $\Delta = 200$.

Substituting these values into Eq. 189 and Eq. 190 we obtain the predicted mass and radius respectively axion stars which would be in the centre of each of our samples as shown in Fig. 59. We see that most of the predicted axion stars have masses in the range $10^{-17} M_\odot \lesssim M_\star \lesssim 10^{-16} M_\odot$. For the axion mass we consider, this places them well below the minimum mass arising from wave effects which can produce microlensing for surveys such as Subaru/HSC (See Sec. VI B).

We also find that the typical axion star radii are of the order 0.1 cAU. This means that they are around an order of magnitude smaller than the N-body softening scale. This is fortunate as it means that, on the scales resolved by the N-body simulation, it is safe to neglect axion wave effects.

Since the axion star masses are related to the masses of their parent halos and as discussed previously, and demonstrated in Fig. 42, by $z = 99$ most halos are expected to have stopped growing, we can expect these axion star properties shown in Fig. 59 to reflect those present

today.

C. Microlensing of Minicluster Sub-Structure

Now that we have an estimate of the axion star radius for each of our samples, we can estimate whether our samples would be able to produce microlensing signals. To do this, we use the predicted NFW/PL curve for each of our sample halos at $z = 99$ for which $f_m > 0.75$. For each profile we then look for critical lensing radii ξ_c as outlined in Sec. VI C.

As shown from Fig. 42, our halos are expected to have almost completely stopped growing in mass by $z = 99$. This does not mean that the virial radius stops growing. In fact, the physical radius continues to grow as the scale factor[21]. Critically, the virial radius grows at the same rate as the concentration which, for $z \lesssim z_{\rm eq}$ also grows as the scale factor. This is important as it means that the scale radius of a halo does not actually change.

Since microlensing is dependent only on the central component of a halo, we can therefore essentially calculate the lensing for the profiles as they are at $z = 99$. However, our lensing calculation shown in Fig. 44 is performed based on a relationship between the virial mass and radius defined at $z = 0$. Therefore, to use the same calculation we have to extrapolate the values for the radius and concentration to today. This can be done simply as $c(z = 0) = 100c(z = 99)$ and $R_{\rm phys}(z = 0) = 100R_{\rm phys}(z = 99) = R_{\rm com}(z = 99)$ where "phys" and "com" denote physical and comoving coordinates respectively.

Assuming that our samples are well modelled by their predicted NFW profiles as shown in Fig. 52, we find that either the halos have no critical lensing radius at all or that their critical lensing radius greater is smaller than their axion star radius. This is to be expected as all of their predicted concentrations are defined by the same concentration mass relation shown in Fig. 44. However, for these samples, the virial radius is measured from the density profile instead of being completely defined by the mass via Eq. 215. Additionally, we find that this inability to produce microlensing persists even when we scale the results by the axion mass, as outlined in Sec. V D.

However, as discussed in the previous section, the majority of our samples are predicted to have scale radii which are smaller than the softening length cut-off of the N-body simulations which produced them. Although we have no reason to believe that these halos should deviate

[21] The resulting change in halo mass is negligible.

from the NFW prediction, for completeness we consider the possibility that their single power law extends to smaller radii. We, therefore, assume that all of our samples are well modelled by a power-law profile with the mean slope of $\alpha = 2.9$. Note that we use virial mass and radius calculated from the density profile of each sample to define the power-law model and not Eq. 127 derived from spherical collapse in Sec. IV as used by Ref. [77] since we find that this underestimates the halo radius.

Using this PL model for our samples, since the slope is steeper than $\alpha = 1$ we are always able to calculate a critical lensing radius. However, for the axion mass assumed in this work ($m_a = 50\mu$ eV) this radius is much smaller than the axion star radius. Therefore, we do not expect that these halos would be able to produce microlensing.

However, as discussed in Sec. V D, we can rescale these results to other axion masses. Doing so, we find that if we considered an axion mass $\gtrsim 10^{-4}$eV, critical lensing radii larger than the predicted axion star mass can be found. We also find that the largest of these halos would also have effective lensing masses $M_{\rm eff} \gtrsim 10^{-11} M_\odot$. This is larger than $3 \times 10^{-12} M_\odot$ required to avoid suppression of the microlensing signal by wave effects.

Fig. 60 shows fraction of objects in the sample found to have critical radii which are simultaneously greater than the axion star radius and bound a mass greater than the minimum required by wave effects is shown as a function of axion mass. We see that thus fraction peaks at just under 10% at $m_a \sim 1\,$meV. It should be noted that this fraction is not representative of the DM mass fraction.

While this finding is interesting, it is important to remember that there is no particular reason for us to suspect that the density profiles for these halos would not turn over to a shallower central slope. As mentioned in the previous section, it appears from Fig. 56 that even our samples for which the scale radius has not been resolved show signs of their density slopes becoming less steep at small radii. However, this does provide us with motivation for new simulations to resolve these halos at a higher resolution.

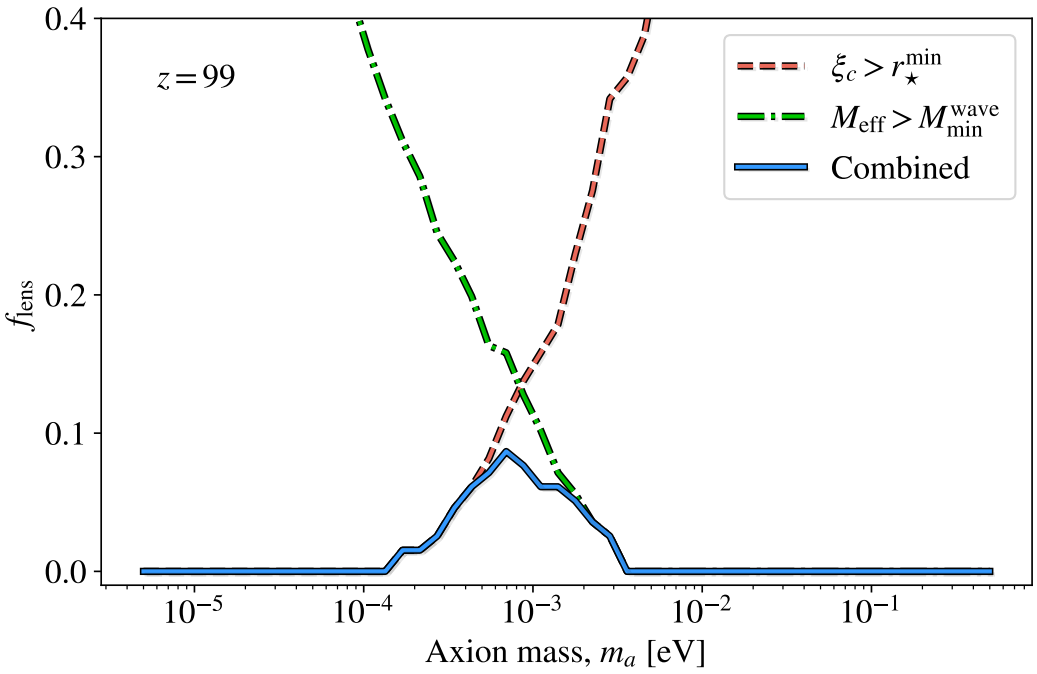

FIG. 60. *Fraction of samples meeting criteria for lensing.* The fraction was calculated for lenses exactly halfway between the observer and the light source. Lensing and non-lensing halos were shown in Fig.46 as yellow stars and orange circles, respectively.

IX. CONCLUSIONS

In Sec. VII, we demonstrated how analytical and semi-analytical methods can be used to estimate the mass function and concentration mass relations for axion miniclusters from a realistic highly non-Gaussian initial axion density field produced by Ref. [55] using a fraction of the computation time as required by traditional N-body methods.

We presented a modified Peak Patch algorithm and show how it can be used to solve the spherical collapse of overdensities in real space and therefore include the full non-Gaussianity of this field. The qualitative behaviour produced by this semi-analytical algorithm is shown to be exactly the same as seen from N-body simulations of the same initial field by Ref. [87].

At late times, Peak Patch gives a halo mass function proportional to $M^{-0.6}$ in the range $10^{-15}M_\odot \lesssim M \lesssim 10^{-10}M_\odot$ which is comparable to N-body simulations. Additionally, we show that, at these late times, the mass function is also well described by a Press-Schechter calculation on the initial power-spectrum with linear growth and assuming Gaussianity.

We follow the approach developed by Navarro et al to use the collapse redshifts of these

halos to estimate their concentrations [89]. We use an analytical formula based on the initial mass variance to estimate the collapse redshift of halos as a function of mass. From this, we calculate a concentration-mass relation that can be fitted to the results from N-body with a single fitting parameter.

We then use Peak Patch to construct merger trees for all of the halos with high temporal precision. We can then calculate the collapse redshift for each individual halo. Then, using the same fitting parameter, we are able to estimate the full statistical spread of halo concentrations.

Our model predicts that the halo concentration reaches a maximum at $M \sim 10^{-13}(m_a/50\mu\text{eV})^{-0.5}M_\odot$ due to the transition to hierarchical structure formation at matter-radiation equality. This feature is not resolved by N-body simulations as their resolution is not high enough to resolve the scale radii of halos at these relatively small masses. This provides us with renewed motivation for higher resolution numerical simulations to investigate this predicted feature.

These concentrations can be straight-forwardly extrapolated to $z = 0$. We find that typical axion miniclusters today would have $c \sim \mathcal{O}(few) \times 10^4$. We show, following lensing calculations for extended density profiles presented by Ref. [79], that such miniclusters would be too diffuse to produce microlensing signals.

In Sec. VIII, we combine our results from Peak Patch with the N-body data produced in Ref. [87] to further investigate the structure of axion miniclusters and their substructure.

We try to identify structures whose density profiles are most likely to deviate from the NFW prediction of Sec. VII. To do this, we use Peak Patch to identify the dense *axion minicluster seeds* which collapse before matter-radiation equality as many of these early collapsing objects should survive as distinct substructures. A random selection of these seeds are then tracked in the N-body data as they evolve from $z = 3976.5$ to $z = 99$. Comparing the final positions of these objects with the positions of the halos determined using SUBFIND we find that this sample is a mix of around 65% ordinary halos and 35% sub-halos.

Developing a metric for the survival of these objects, we find that most of these initial objects are completely disrupted by the merger process. We see that the most important factor which determines whether these early halos survive is their mass, with higher mass halos being more likely to survive.

We also calculate the radial density profiles for our sampled objects at both $z = 3976.5$ and $z = 99$. It is found that at $z = 3976.5$ the density profiles are still very well described by the analytical formula for the concentration-mass relation found in Sec. V A. However, at this redshift, these halos are equally well fit by a single power-law with an average slope of $r^{-2.5}$. Interestingly, as discussed in Sec. VIII B 3, we see that the slopes of each individual sample correlate with the samples redshift of collapse in a way that is consistent with the formalism from Navarro et al.

For halos at $z = 99$, we see that their density profiles are better described by the NFW profile predicted using the same analytical formula than by a single power law. However, the predicted scale radii for most of these samples are smaller than the resolution of the N-body simulations. We are therefore unable to state with certainty that these lower mass halos are best fit by a split power law such as NFW.

For this subset, we, therefore, consider the possibility that they are well fit by a single power law profile with a slope $\sim r^{-2.9}$ down to small radii. We find that such a profile fits these halos relatively well, however, there are signs that many of these the sample's density profiles are beginning to turn over to a shallower slope at small radii.

For these halos and sub-halos at $z = 99$, we find no discernible relationship between the overdensities of the first seeds from which they formed and their final density profiles. This is in contrast to what has previously been assumed in the literature.

By calculating their virial velocity, we also estimate the masses and radii of the axion stars that we would expect to be present at the centres of these halos. We find that, for an axion mass of $m_a = 50\mu\text{eV}$, most axion stars would have masses in the range $10^{-17}M_\odot \lesssim M_\star \lesssim 10^{-16}M_\odot$. These masses are below the minimum mass required from wave optics to be able to produce microlensing.

Assuming that this subset of halos at $z = 99$ can be safely described by such a power law down to small radii, we find that for the axion mass considered ($m_a = 50\mu\text{eV}$), the predicted axion star prevents the object from producing a microlensing signal. However, using the scaling relations derived in Sec. V D, we find that, for axion masses $m_a \gtrsim 100\mu\text{eV}$, the critical lensing radius is larger than the radius of the axion star. Additionally, we find that for the largest of these halos, the effective lensing mass is slightly larger than the minimum required from wave optics to be able to produce microlensing. This result further highlights the need for higher resolution N-body simulations to determine the inner density

profiles of these minicluster halos and sub-halos.

There are a number of ways that this work could be extended in the future. For example, we have applied our Peak Patch algorithm to the initial density field produced by simulations performed by Vaquero et al., there exist a number of other similar simulations. Each of these simulations differs slightly, incorporating different phenomena into the initial evolution of the axion field and/or simulating the evolution of the field during different epochs. Using the methods developed here, we could very quickly compare both the halo mass functions and the concentrations that arise from these different initial fields.

One could also extend the use of the merger trees calculated by Peak Patch in a number of ways. A particular point of interest is the relationship between a halo's merger history and its final substructure. One way of investigating this could be to combine merger trees produced by Peak Patch with N-body results to train a machine-learning algorithm to estimate the final halo substructure based on the input merger trees.

As mentioned in Sec. III, if most of the axion DM is bound in miniclusters, this would significantly reduce the average axion flux passing through the Earth and hence severely reduce the sensitivity of direct detection experiments such as ADMX. In this case, the ability of these experiments to detect the axion will depend critically on the extent to which axion miniclusters are disrupted by, for example, gravitational interactions with stars as they orbit the galaxy. Kavanagh et al have shown in Ref. [77] that the extent to which we can expect miniclusters to be disrupted by these sorts of events is highly dependent on their distribution and internal structure. Therefore, further studies similar to the work presented here will play a critical role in defining future efforts to find the axion.

Appendix A: Considerations for PP comparison with N-Body

Initially, for late times, the HMF produced using Peak Patch differed significantly from that calculated from N-body. After some discussion with the authors of Ref. [87], it was determined that the differences between our semi-analytic model and N-body simulations arise largely because, at the late redshifts in question, the largest scales of the N-body simulations have entered into the quasi-linear regime. This can be seen by the fact that their power spectra on large scales are smaller than what is predicted by linear theory (see below for a quantitative study). This results in there being fewer massive halos in the simulation than predicted by analytical models based on linear growth. Subsequently, more small halos are able to survive thus explaining the increased magnitude of the HMF. As we will discuss, however, the departure of a simulation from linear growth on the largest scales (corresponding to the box size) calls into question the reliability of the simulations at late times. Ultimately, we have decided to restrict our discussions of the mass function to $z \leq 629$, where linear growth is accurate on the box size.

As shown above, the growth factor predicted by linear theory is

$$D_{\rm lin}(x) = 1 + \frac{3}{2}x, \tag{A1}$$

where $x = a/a_{\rm eq}$.

We then reconstructed the growth factor from the N-body simulations using the largest scales of their power spectrum at each redshift. Assuming that this function should follow a similar evolution to linear theory, we allow for a different power-law dependence on x

$$D_{\rm nb}(x) = 1 + \frac{3}{2}x^{\alpha}. \tag{A2}$$

Performing a least-squares fit to the data we find a power of 0.758 best fits the N-body data, as shown in Fig. 61. While this fitted growth function does not perfectly capture the evolution of the N-body data shown in Fig. 61, it is sufficient to highlight the source of the differences in Peak Patch.

As seen in Fig. 62, when we modify Peak Patch to use this fitted growth function, the outputted HMF at $z = 99$ much better matches the N-body result compared to the linear case. We additionally see, as we would expect, that the two cases are almost identical for $z > z_{\rm eq}$.

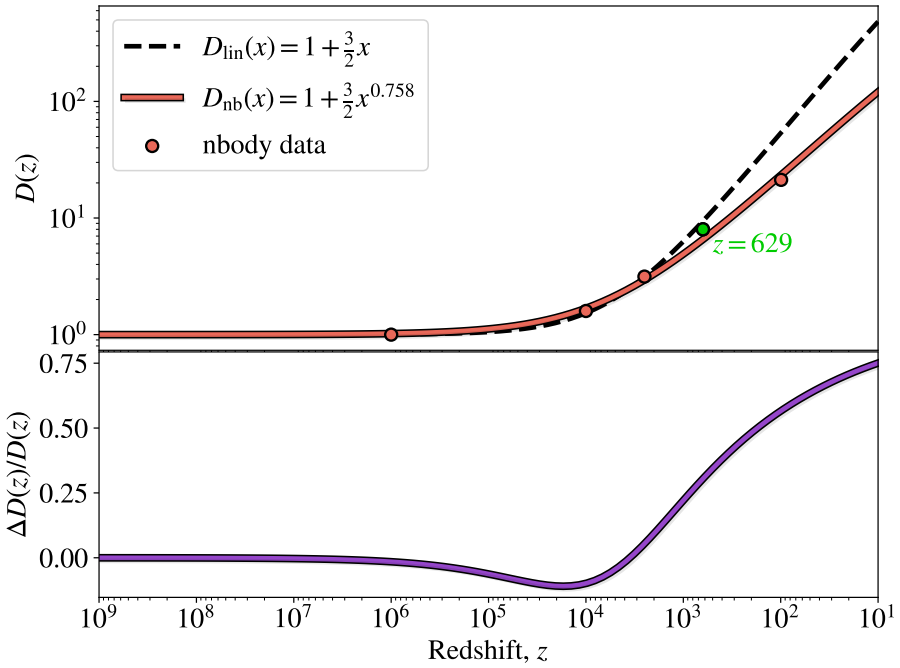

FIG. 61. *Growth Factor* - Comparison of the growth factor calculated from linear theory and the effective growth factor of Ref [87] determined from the largest scales of their power spectrum at each redshift.

Interestingly, the PS prediction using the linear growth factor appears to almost perfectly match the N-body HMF. If we instead use the fitted growth function we find that the magnitude of the HMF is slightly higher with a lower cut-off mass. However, since we know that the N-body simulation becomes non-linear at the largest scales, it is plausible that the HMF is lower than what we would predict from PS even with the fitted growth factor. This is because, given the finite size of the box, the number of small halos can only fall as the largest halos reach a size comparable to that of the box. Additionally, different fitting functions, such as Sheth-Torman, produce HMF estimates that do not match the N-body data so well. Therefore, the fact that using the standard Press-Schechter fitting function matches so well, is likely to be largely coincidental.

We also find that this change in growth makes very little difference to the predicted halo concentrations.

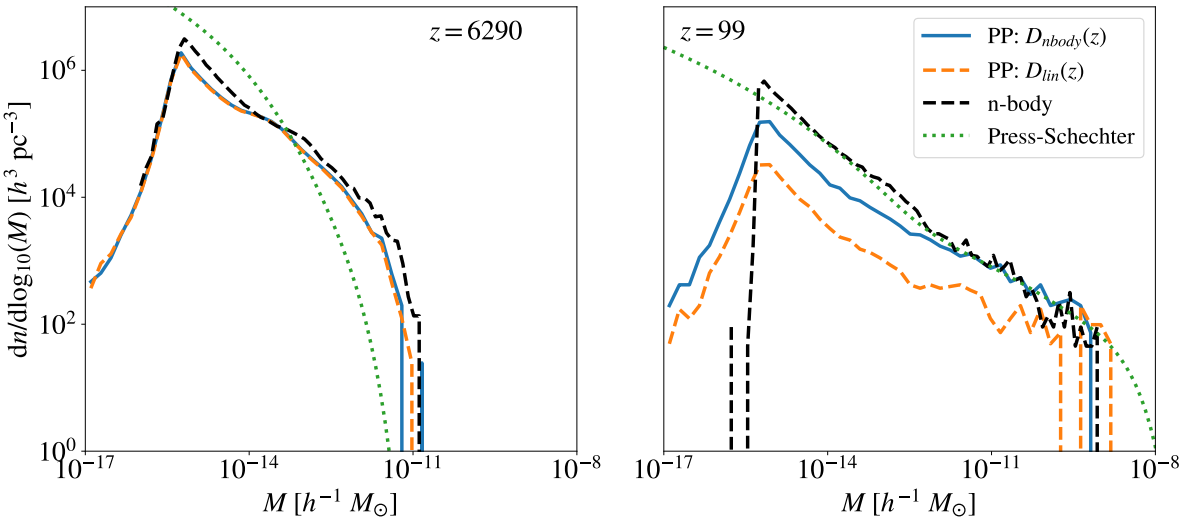

FIG. 62. HMF from Peak Patch with the linear growth factor and the growth factor fitted from N-body. The green dotted line shows the Press-Schechter prediction for the HMF using the standard Press-Schechter fitting function.

Appendix B: Core-halo mass relation for a power-law minicluster

For a generic spherically symmetric density field, the total gravitational potential energy within a sphere of radius R is given by

$$E_p(R)' = -4\pi G \int_0^R \frac{M'(r)\rho'(r)r'^2 \mathrm{d}r'}{r'}. \tag{B1}$$

For a PL profile, the radial density is given by

$$\rho'(r) = \rho'_0 \left(\frac{r'}{r'_0}\right)^{-\alpha} \tag{B2}$$

and radial mass profile by

$$M'(r) = M'_{\mathrm{PL},0} \left(\frac{r'}{r'_0}\right)^{3-\alpha} \tag{B3}$$

where we define $M'_{\mathrm{PL},0}$ to be the total mass of the halo given by

$$M'_{\mathrm{PL},0} = \frac{4\pi\rho_0}{3-\alpha} {r'_0}^3. \tag{B4}$$

Performing the integral, we find that

$$E'_{p,\mathrm{PL}}(r'_0) = -G\frac{{M'_{pl,0}}^2}{r'_0}\frac{3-\alpha}{5-2\alpha}. \tag{B5}$$

For $\alpha = 0$, we recover the uniform sphere case, as expected.

Applying the virial theorem as before, we find that

$$M_c \sim a^{-1/2} \left(\frac{3-\alpha}{10-4\alpha} \right)^{1/2} \left(\frac{M_{\rm PL,0}}{r_0} \right)^{1/2}. \tag{B6}$$

We see that this is the same as the uniform case with the addition of a term involving density slope α which suppress the core mass.

As well as this, the radius of the halo r_0 is defined via the classic Kolb and Tkachev density formula

$$\langle \rho \rangle_{\rm KT} = 136 \rho_{eq} \delta_i^3 (1+\delta_i), \tag{B7}$$

where δ_i is the initial halo overdensity [22]. From this we find

$$\frac{1}{r_0} = \left[\frac{4\pi 136 \rho_{eq} \delta_i^3 (1+\delta_i)}{3 M_h} \right]^{1/3}, \tag{B8}$$

thus giving us a core mass

$$M_c \sim a^{-1/2} \left(\frac{3-\alpha}{10-4\alpha} \right)^{1/2} \delta_i^{1/2} (\delta_i + 1)^{1/6} M_{\rm PL,0}^{1/3}. \tag{B9}$$

Following the uniform case, we normalise such that for uniform halos ($\alpha = 0$) with initial overdensities δ_i which reproduce the standard final overdensity ($\langle \rho \rangle_{\rm KT} / \rho_m(z) = \xi(z)$) we predict the axion star core mass to be $M_c(z) = M_{\rm min}(z)/4$. We therefore need to find the normalising initial overdensity which we denote $\delta_{\rm N}$

$$\frac{\langle \rho \rangle}{\rho_m(z)} = \xi(z) \tag{B10}$$

$$\implies 136 \frac{\rho_{eq}}{\rho_m(z)} \delta_{\rm N}^3 (\delta_{\rm N} + 1) = \xi(z) \tag{B11}$$

$$\implies \delta_{\rm N}^{1/2} (\delta_{\rm N} + 1)^{1/6} = \left(\frac{\xi(z)}{136} \right)^{1/6} \left(\frac{a_{\rm eq}}{a} \right)^{1/2} \tag{B12}$$

We then find our core mass to be

[22] As discussed briefly in Sec. VIII B 3, the halo densities that we estimate using this equation are around a factor of 8 larger than are found using N-Body simulations. However, this may be, in part, due to the specific way in which we estimate δ_i.

$$M_c(M_h = M_{\rm min}) = N \left(\frac{3}{10}\right)^{1/2} \delta_{\rm N}^{1/2} (1+\delta_{\rm N})^{1/6} M_{\rm min,0}^{1/3}, \tag{B13}$$

where N is our normalisation factor which we see must be

$$N = \frac{1}{4} \left(\frac{a}{a_{eq}}\right)^{1/2} \left(\frac{10}{3}\right)^{1/2} \left(\frac{136}{\xi(0)}\right)^{1/6} M_{\rm min,0}^{2/3}. \tag{B14}$$

After some algebra, we then find our core-halo mass relation to be

$$M_c = 4.16 \times 10^{-16} M_\odot A(\alpha) \Delta(\delta_i) \left(\frac{M_{\rm PL}}{10^{-12} M_\odot}\right)^{1/3} \left(\frac{m_a}{50 \mu{\rm eV}}\right)^{-1} \tag{B15}$$

where $A(\alpha)$ and $\Delta(\delta_i)$ are given by

$$A(\alpha) = \sqrt{\frac{3-\alpha}{5-\alpha}}, \tag{B16}$$

and

$$\Delta(\delta_i) = \delta_i^{1/2} (\delta_i + 1)^{1/6}, \tag{B17}$$

respectively.

This is essentially identical to the uniform sphere case but with the addition of the $A(\alpha)$ and $\Delta(\delta_i)$ functions. The former acts to suppress the core mass while the latter enhances it compared to the uniform sphere case. It should also be noted that the scaling $\Delta(\delta_i)$ could have also been found by simply replacing $\xi(z)$ in the standard core-halo mass relation with Eq. B10.

Appendix C: Kernel Density Estimator

As mentioned in Sec. VIII, we use a kernel density estimator to determine the location of the centre of halos. In this, we assign each particle a Gaussian distribution with some width σ. Then, after summing the total amplitude of all of these *kernals* over all space, we can simply take the maximum point as the point of maximum local density and therefore the centre of a halo.

As shown in Fig. 63, if we define the centre of a halo to be its point of maximum density, this method can often locate the centres of halos much more effectively than cruder methods such as simply calculating the median particle position.

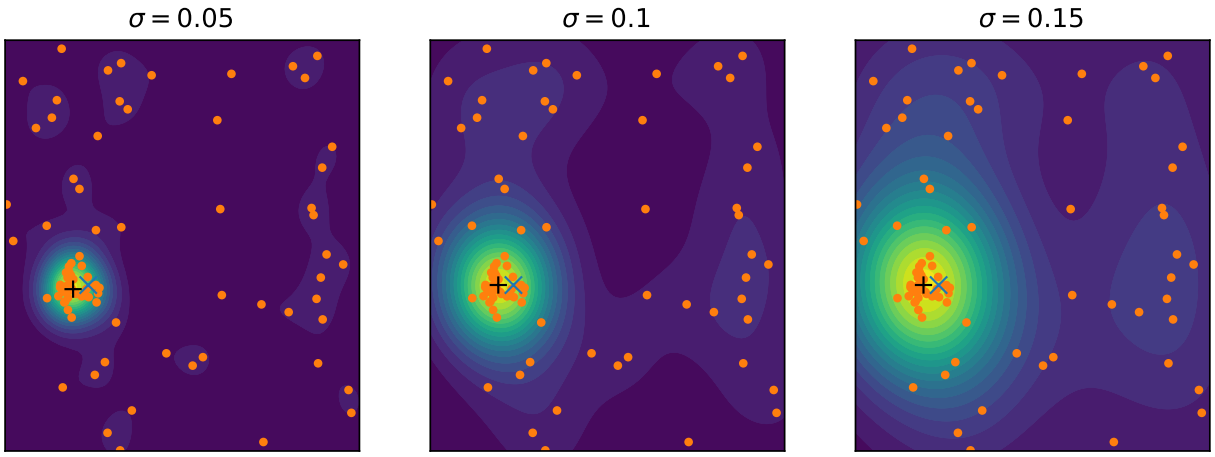

FIG. 63. *Kernel density estimator* - Demonstration of the KDE in which each particle is represented by a Gaussian wave packet of width σ. The halo centres calculated using the KDE and median particle position are shown as a black cross and blue x respectively. Colour map indicates the sum of the wave packets.

Appendix D: Calculating the virial properties

As discussed in Sec. VIII, we want to measure the virial velocity of our samples however for most the total radius of the sample is smaller than the virial radius of the halo/sub-halo to which it belongs. However, as shown in Fig. 64, the virial velocity is defined primarily by the centre of the halo and changes very little with the radius of the sample considered.

Additionally, as mentioned in Sec. VIII, calculating the total gravitational potential by summing the potentials between each pair of N-body particles would the computationally very expensive. Therefore, we instead calculate U by binning the particles into n_{bins}^3 cells and then summing the potentials between each pair of cells.

For a spherically uniform halo, it can be shown that the total gravitational potential energy is given by

$$U_{\text{sph}} = -\frac{3GM^2}{5}. \tag{D1}$$

This is used as a baseline for comparison to our calculation in Fig. 65. We see that, for each of our test cases, the calculated potential has almost completely converged by $n_{\text{bins}} = 25$. One of the test halos is noticeably further from convergence than the others, however this should make only around $\mathcal{O}(1)$ difference to the calculation. Therefore, in the interest of

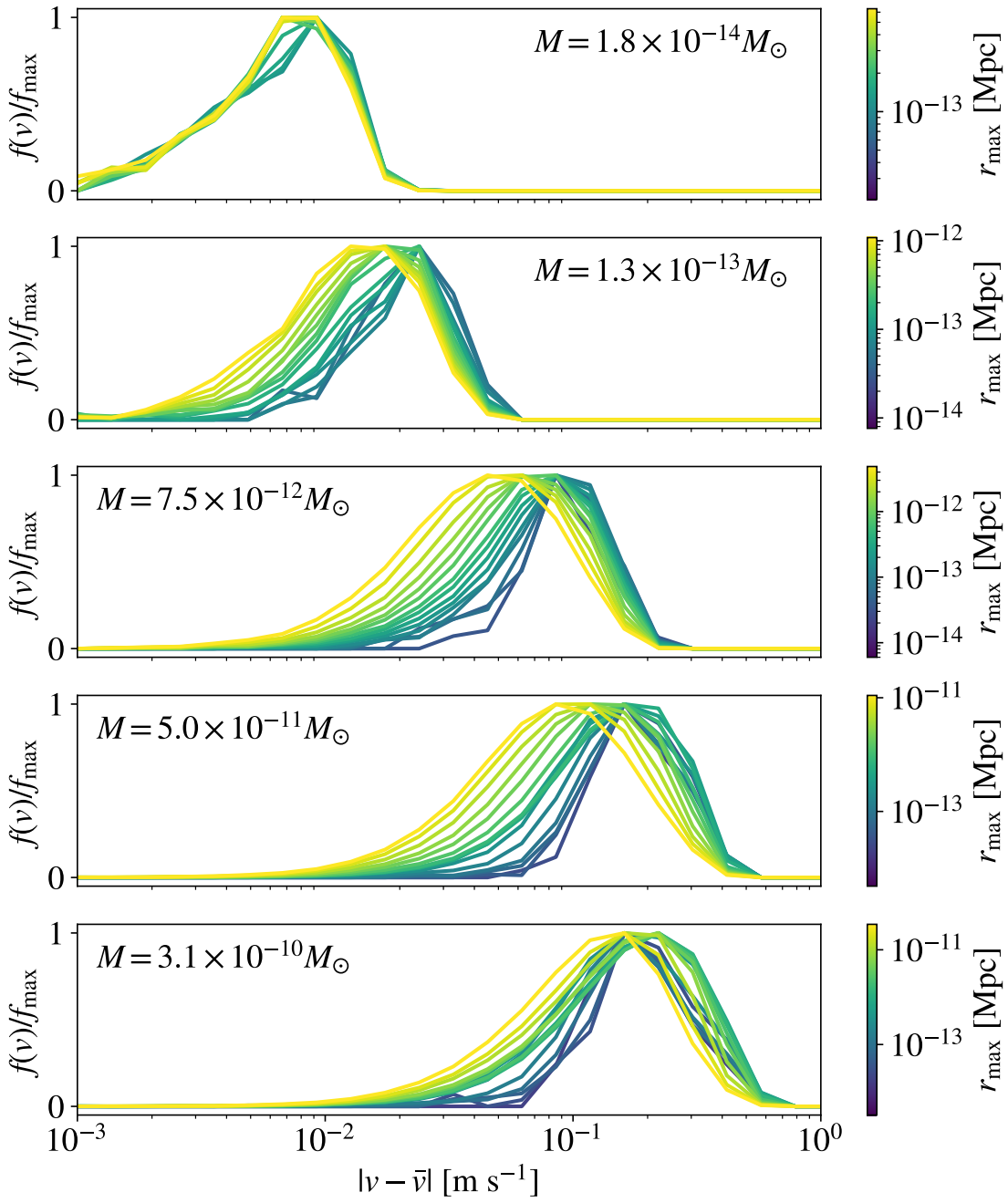

FIG. 64. *Velocity distribution as a function of sample radius.* - Colour indicates the radius from the halo centre in which particles were included in the calculation of the velocity distribution for five test halos which reflect the full mass range of the N-body data.

limiting computation time, we, therefore, use this value when calculating the potential for our samples.

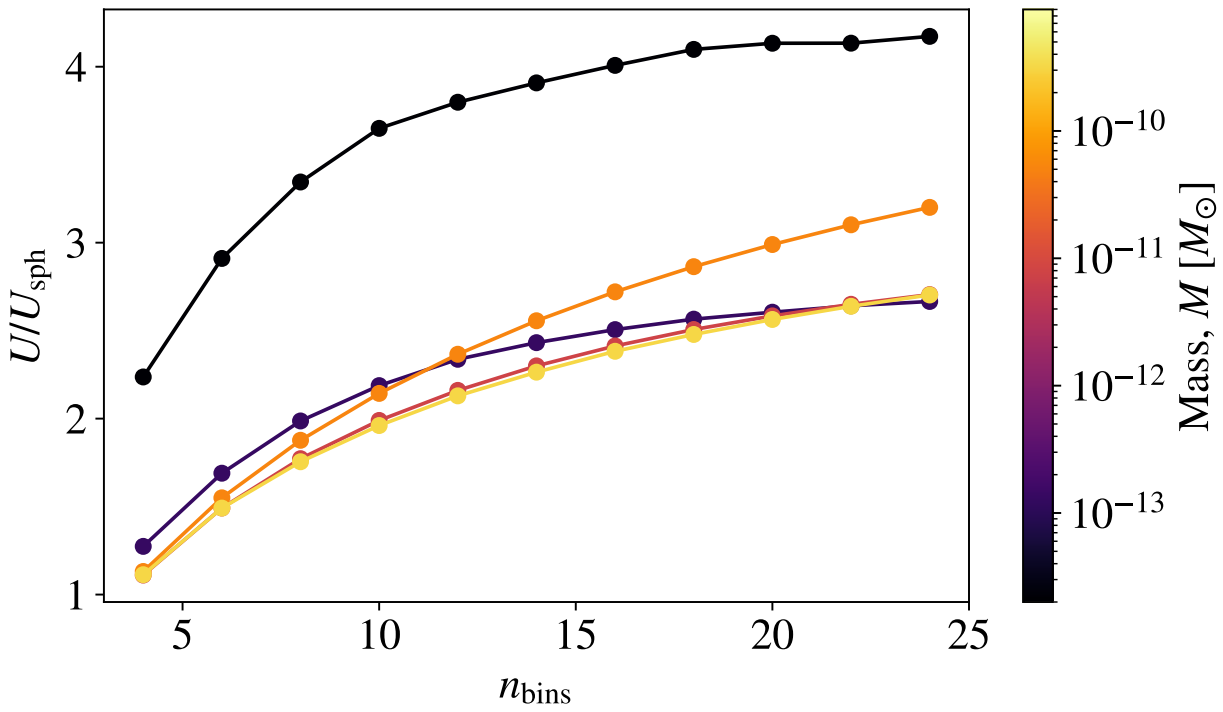

FIG. 65. *Total gravitational potential energy* - Calculated by binning the particles into n^3_{bins} bins and then summing the potentials between each pair of cells for five different halo masses which reflect the full range of halo masses in the N-body data.

---

[1] F. Zwicky, Helvetica Physica Acta **6**, 110 (1933).

[2] F. Zwicky, Astrophys. J.**86**, 217 (1937).

[3] W. Thomson, Baron Kelvin, *Baltimore Lectures on Molecular Dynamics and the Wave Theory of Light* (Cambridge University Press, 2010).

[4] H. Poincaré, Popular Astronomy **14**, 475 (1906).

[5] J. C. Kapteyn, Astrophys. J.**55**, 302 (1922).

[6] J. H. Oort, Bain **6**, 249 (1932).

[7] V. C. Rubin and J. Ford, W. Kent, Astrophys. J.**159**, 379 (1970).

[8] V. C. Rubin, J. Ford, W. K., and N. Thonnard, Astrophys. J.**238**, 471 (1980).

[9] S. T. Gottesman, R. D. Davies, and V. C. Reddish, MNRAS**133**, 359 (1966).

[10] M. S. Roberts, Astrophys. J.**144**, 639 (1966).

[11] C. M. Will, Living Rev. Rel. **9**, 3 (2006), gr-qc/0510072.

[12] R. Massey, T. Kitching, and J. Richard, Rept. Prog. Phys. **73**, 086901 (2010), 1001.1739.

[13] A. A. Penzias and R. W. Wilson, Astrophys. J.**142**, 419 (1965).

[14] R. H. Dicke, P. J. E. Peebles, P. G. Roll, and D. T. Wilkinson, Astrophys. J.**142**, 414 (1965).

[15] D. J. Fixsen *et al.*, Astrophys. J.**420**, 445 (1994).

[16] C. L. Bennett *et al.*, ApJS**208**, 20 (2013), 1212.5225.

[17] Planck Collaboration *et al.*, A&A**641**, A1 (2020), 1807.06205.

[18] J. H. Davis and J. Silk, Phys. Rev. Lett. **114**, 051303 (2015), 1410.5423.

[19] CAST, S. Aune *et al.*, Solar axion search with the CAST experiment, in *34th International Conference on High Energy Physics*, 2008, 0810.1874.

[20] M. H. Chan, Sci. Rep. **11**, 20087 (2021), 2109.11734.

[21] Fermi-LAT, V. Gammaldi *et al.*, PoS **ICRC2021**, 509 (2021), 2109.11291.

[22] A. Sarkar *et al.*, JCAP **04**, 012 (2016), 1512.03325.

[23] V. Poulin, P. D. Serpico, and J. Lesgourgues, JCAP **08**, 036 (2016), 1606.02073.

[24] M. Dentler *et al.*, (2021), 2111.01199.

[25] D. J. E. Marsh and J. C. Niemeyer, Phys. Rev. Lett. **123**, 051103 (2019), 1810.08543.

[26] M. Viel, J. Lesgourgues, M. G. Haehnelt, S. Matarrese, and A. Riotto, Phys. Rev. D **71**, 063534 (2005), astro-ph/0501562.

[27] S. Hannestad, A. Mirizzi, G. G. Raffelt, and Y. Y. Y. Wong, JCAP **08**, 001 (2010), 1004.0695.

[28] J. L. Feng, Ann. Rev. Astron. Astrophys. **48**, 495 (2010), 1003.0904.

[29] L. Roszkowski, E. M. Sessolo, and S. Trojanowski, Rept. Prog. Phys. **81**, 066201 (2018), 1707.06277.

[30] A. M. Green and B. J. Kavanagh, J. Phys. G **48**, 043001 (2021), 2007.10722.

[31] D. J. E. Marsh, Phys. Rept. **643**, 1 (2016), 1510.07633.

[32] S. P. Martin, Adv. Ser. Direct. High Energy Phys. **18**, 1 (1998), hep-ph/9709356.

[33] S. Tremaine and J. E. Gunn, Phys. Rev. Lett.**42**, 407 (1979).

[34] L. Roszkowski, Phys. Lett. B **262**, 59 (1991).

[35] XENON, E. Aprile *et al.*, Phys. Rev. Lett. **121**, 111302 (2018), 1805.12562.

[36] Fermi-LAT, M. Ackermann *et al.*, Phys. Rev. Lett. **115**, 231301 (2015), 1503.02641.

[37] G. Arcadi *et al.*, Eur. Phys. J. C **78**, 203 (2018), 1703.07364.

[38] Y. B. Zel'dovich and I. D. Novikov, AZh**43**, 758 (1966).

[39] S. Hawking, MNRAS**152**, 75 (1971).

[40] LIGO Scientific, Virgo, B. P. Abbott *et al.*, Phys. Rev. X **9**, 031040 (2019), 1811.12907.

[41] S. W. Hawking, Nature (London)**248**, 30 (1974).

[42] M. Meneghetti, *Introduction to Gravitational Lensing* .

[43] EROS-2, P. Tisserand *et al.*, Astron. Astrophys. **469**, 387 (2007), astro-ph/0607207.

[44] N. Smyth *et al.*, Phys. Rev. D **101**, 063005 (2020), 1910.01285.

[45] R. Peccei and H. Quinn, Physical Review Letters **38**, 1440 (1977).

[46] J. Preskill, M. B. Wise, and F. Wilczek, Physics Letters B **120**, 127 (1983).

[47] L. Abbott and P. Sikivie, Physics Letters B **120**, 133 (1983).

[48] M. Dine and W. Fischler, Physics Letters B **120**, 137 (1983).

[49] A. Arvanitaki, M. Baryakhtar, and X. Huang, Phys. Rev. D **91**, 084011 (2015), 1411.2263.

[50] M. J. Stott and D. J. E. Marsh, Phys. Rev. **D98**, 083006 (2018), 1805.02016.

[51] G. G. Raffelt, Lect. Notes Phys. **741**, 51 (2008), hep-ph/0611350.

[52] J. H. Chang, R. Essig, and S. D. McDermott, JHEP **09**, 051 (2018), 1803.00993.

[53] E. Armengaud *et al.*, Journal of Cosmology and Astroparticle Physics **2019**, 047 (2019).

[54] M. Gorghetto, E. Hardy, and G. Villadoro, JHEP **07**, 151 (2018), 1806.04677.

[55] A. Vaquero, J. Redondo, and J. Stadler, (2018), 1809.09241, [JCAP1904,no.04,012(2019)].

[56] M. Buschmann, J. W. Foster, and B. R. Safdi, (2019), 1906.00967.

[57] V. B. Klaer and G. D. Moore, JCAP **11**, 049 (2017), 1708.07521.

[58] T. Hiramatsu, M. Kawasaki, K. Saikawa, and T. Sekiguchi, JCAP **01**, 001 (2013), 1207.3166.

[59] T. Hiramatsu, M. Kawasaki, K. Saikawa, and T. Sekiguchi, Phys. Rev. D **85**, 105020 (2012).

[60] T. Hiramatsu, M. Kawasaki, T. Sekiguchi, M. Yamaguchi, and J. Yokoyama, Phys. Rev. D **83**, 123531 (2011).

[61] R. A. Battye and E. P. S. Shellard, Phys. Rev. Lett. **73**, 2954 (1994).

[62] D. Harari and P. Sikivie, Physics Letters B **195**, 361 (1987).

[63] M. Hindmarsh, J. Lizarraga, A. Lopez-Eiguren, and J. Urrestilla, Phys. Rev. Lett. **124**, 021301 (2020).

[64] M. Y. Khlopov, B. A. Malomed, and Y. B. Zeldovich, Monthly Notices of the Royal Astronomical Society **215**, 575 (1985), https://academic.oup.com/mnras/article-pdf/215/4/575/4082842/mnras215-0575.pdf.

[65] C. Hogan and M. Rees, Physics Letters B **205**, 228 (1988).

[66] E. W. Kolb and I. I. Tkachev, Astrophys. J. **460**, L25 (1996), astro-ph/9510043.

[67] E. W. Kolb and I. I. Tkachev, Phys. Rev. **D50**, 769 (1994), astro-ph/9403011.

[68] MADMAX Working Group, A. Caldwell *et al.*, Phys. Rev. Lett. **118**, 091801 (2017).

[69] D. J. E. Marsh, K.-C. Fong, E. W. Lentz, L. Smejkal, and M. N. Ali, Phys. Rev. Lett. **123**, 121601 (2019), 1807.08810.

[70] S. Lee, S. Ahn, J. Choi, B. Rok Ko, and Y. K. Semertzidis, CAPP-8TB: Search for Axion Dark Matter in a Mass Range of 6.62 to 7.04 μeV, in *Meeting of the Division of Particles and Fields of the American Physical Society (DPF2019) Boston, Massachusetts, July 29-August 2, 2019*, 2019, 1910.00047.

[71] M. Baryakhtar, J. Huang, and R. Lasenby, Phys. Rev. D **98**, 035006 (2018), 1803.11455.

[72] A. Mitridate, T. Trickle, Z. Zhang, and K. M. Zurek, (2020), 2005.10256.

[73] M. Lawson, A. J. Millar, M. Pancaldi, E. Vitagliano, and F. Wilczek, Phys. Rev. Lett. **123**, 141802 (2019), 1904.11872.

[74] P. Tinyakov, I. Tkachev, and K. Zioutas, JCAP **01**, 035 (2016), 1512.02884.

[75] V. I. Dokuchaev, Yu. N. Eroshenko, and I. I. Tkachev, J. Exp. Theor. Phys. **125**, 434 (2017), 1710.09586, [Zh. Eksp. Teor. Fiz.152,no.3,511(2017)].

[76] C. A. J. O'Hare and A. M. Green, Phys. Rev. D **95**, 063017 (2017), 1701.03118.

[77] B. J. Kavanagh, T. D. P. Edwards, L. Visinelli, and C. Weniger, (2020), 2011.05377.

[78] M. Fairbairn, D. J. E. Marsh, and J. Quevillon, Phys. Rev. Lett. **119**, 021101 (2017), 1701.04787.

[79] M. Fairbairn, D. J. E. Marsh, J. Quevillon, and S. Rozier, Phys. Rev. D **97**, 083502 (2018), 1707.03310.

[80] A. Katz, J. Kopp, S. Sibiryakov, and W. Xue, JCAP **12**, 005 (2018), 1807.11495.

[81] T. D. P. Edwards, B. J. Kavanagh, L. Visinelli, and C. Weniger, Phys. Rev. Lett. **127**, 131103 (2021).

[82] I. I. Tkachev, JETP Lett. **101**, 1 (2015), 1411.3900.

[83] J. R. Bond and S. T. Myers, ApJS**103**, 1 (1996).

[84] J. R. Bond and S. T. Myers, ApJS**103**, 41 (1996).

[85] J. R. Bond and S. T. Myers, ApJS**103**, 63 (1996).

[86] G. Stein, M. A. Alvarez, and J. R. Bond, Mon. Not. Roy. Astron. Soc. **483**, 2236 (2019), 1810.07727.

[87] B. Eggemeier, J. Redondo, K. Dolag, J. C. Niemeyer, and A. Vaquero, Phys. Rev. Lett. **125**,

041301 (2020), 1911.09417.

[88] D. Ellis, D. J. E. Marsh, and C. Behrens, Phys. Rev. D **103**, 083525 (2021), 2006.08637.

[89] J. F. Navarro, C. S. Frenk, and S. D. M. White, Astrophys. J.**490**, 493 (1997), astro-ph/9611107.

[90] J. Enander, A. Pargner, and T. Schwetz, Journal of Cosmology and Astroparticle Physics **2017**, 038 (2017).

[91] D. Ellis, In preparation (2021).

[92] H. Mo, F. van den Bosch, and S. White, *Galaxy Formation and Evolution*Galaxy Formation and Evolution (Cambridge University Press, 2010).

[93] D. Marsh, D. Ellis, and V. Mehta, *Introduction to Dark Matter* (TBC, 2021).

[94] P. D. Sackett and L. S. Sparke, Astrophys. J.**361**, 408 (1990).

[95] J. Einasto, Trudy Astrofizicheskogo Instituta Alma-Ata **5**, 87 (1965).

[96] The NASA/IPAC extragalactic database, https://ned.ipac.caltech.edu/, (accessed: 16.09.2021).

[97] F. W. Dyson, A. S. Eddington, and C. Davidson, Philosophical Transactions of the Royal Society of London Series A **220**, 291 (1920).

[98] N. Kaiser, G. Squires, and T. J. Broadhurst, Astrophys. J. **449**, 460 (1995), astro-ph/9411005.

[99] D. Clowe *et al.*, Astrophys. J. Lett. **648**, L109 (2006), astro-ph/0608407.

[100] V. Mukhanov, *Physical Foundations of Cosmology* (Cambridge University Press, 2005).

[101] Royal Society Summer Exhibition 2013, https://chrisnorth.github.io/planckapps/Simulator/, (accessed: 19.09.2021).

[102] S. Borsanyi *et al.*, Nature **539**, 69 (2016), 1606.07494.

[103] M. Schumann, J. Phys. G **46**, 103003 (2019), 1903.03026.

[104] R. Catena and P. Ullio, JCAP **08**, 004 (2010), 0907.0018.

[105] E. L. Fireman, B. T. Cleveland, and H. Uberall, Astrophys. J.**326**, 645 (1988).

[106] XENON Collaboration 7, E. Aprile *et al.*, Phys. Rev. Lett. **121**, 111302 (2018).

[107] PandaX-II Collaboration, X. Cui *et al.*, Phys. Rev. Lett. **119**, 181302 (2017).

[108] LUX Collaboration, D. S. Akerib *et al.*, Phys. Rev. Lett. **118**, 021303 (2017).

[109] GAMBIT, P. Athron *et al.*, Eur. Phys. J. C **77**, 879 (2017), 1705.07917.

[110] L. Miramonti, AIP Conf. Proc. **785**, 3 (2005), hep-ex/0503054.

[111] K. Freese, M. Lisanti, and C. Savage, Rev. Mod. Phys. **85**, 1561 (2013), 1209.3339.

[112] C. A. J. O'Hare, Phys. Rev. D **102**, 063024 (2020), 2002.07499.

[113] C. A. J. O'Hare, (2021), 2109.03116.

[114] Y. Zhang, M. L. Norman, P. Anninos, and T. Abel, Primordial star forming regions in a CDM universe, in *The Seventh Astrophysical Conference: Star formation, near and far*, edited by S. S. Holt and L. G. Mundy, , American Institute of Physics Conference Series Vol. 393, pp. 329–333, 1997, astro-ph/9611224.

[115] B. J. Carr, Astrophys. J.**201**, 1 (1975).

[116] S. Kováčik, (2021), 2102.06517.

[117] B. V. Lehmann and S. Profumo, (2021), 2105.01627.

[118] M. C. Lopresto, The Physics Teacher **41**, 299 (2003).

[119] R. Laha, Phys. Rev. Lett. **123**, 251101 (2019), 1906.09994.

[120] M. Boudaud and M. Cirelli, Phys. Rev. Lett. **122**, 041104 (2019), 1807.03075.

[121] S. Clark, B. Dutta, Y. Gao, L. E. Strigari, and S. Watson, Phys. Rev. D **95**, 083006 (2017), 1612.07738.

[122] R. Laha, J. B. Muñoz, and T. R. Slatyer, Phys. Rev. D **101**, 123514 (2020), 2004.00627.

[123] T. D. Brandt, Astrophys. J. Lett. **824**, L31 (2016), 1605.03665.

[124] B. J. Kavanagh, bradkav/pbhbounds: Release version, 2019.

[125] J. H. Christenson, J. W. Cronin, V. L. Fitch, and R. Turlay, Phys. Rev. Lett. **13**, 138 (1964).

[126] G. Raffelt, Space Science Reviews **100**, 153 (2002).

[127] J. Pendlebury *et al.*, Physical Review D **92** (2015).

[128] G. Raffelt and L. Stodolsky, Phys. Rev. D **37**, 1237 (1988).

[129] P. Svrcek and E. Witten, Journal Of High Energy Physics (2006).

[130] G. Grilli di Cortona, E. Hardy, J. Pardo Vega, and G. Villadoro, JHEP **01**, 034 (2016), 1511.02867.

[131] T. Kibble, Physics Reports **67**, 183 (1980).

[132] T. W. B. Kibble, Journal of Physics A: Mathematical and General **9**, 1387 (1976).

[133] L. Dai and M.-E. Jordi, Astron. J. **159**, 49 (2020), 1908.01773.

[134] W. H. Press, B. S. Ryden, and D. N. Spergel, Astrophys. J.**347**, 590 (1989).

[135] J. N. Moore, E. P. S. Shellard, and C. J. A. P. Martins, Phys. Rev. D **65**, 023503 (2001).

[136] A. Lewis, A. Challinor, and A. Lasenby, Astrophys. J. **538**, 473 (2000), astro-ph/9911177.

[137] P. Sikivie, Phys. Rev. Lett. **51**, 1415 (1983).

[138] M. Srednicki, Nuclear Physics B **260**, 689 (1985).

[139] E. Kolb and M. Turner, *The Early Universe*Frontiers in physics (Addison-Wesley, 1990).

[140] J. E. Kim, Phys. Rev. Lett. **43**, 103 (1979).

[141] M. Shifman, A. Vainshtein, and V. Zakharov, Nuclear Physics B **166**, 493 (1980).

[142] M. Dine, W. Fischler, and M. Srednicki, Physics Letters B **104**, 199 (1981).

[143] A. R. Zhitnitsky, Sov. J. Nucl. Phys. **31**, 260 (1980), [Yad. Fiz.31,497(1980)].

[144] V. Plakkot and S. Hoof, Phys. Rev. D **104**, 075017 (2021), 2107.12378.

[145] S. J. Asztalos *et al.*, Phys. Rev. Lett. **104**, 041301 (2010).

[146] I. Stern, PoS **ICHEP2016**, 198 (2016), 1612.08296.

[147] B. T. McAllister *et al.*, Phys. Dark Univ. **18**, 67 (2017), 1706.00209.

[148] J. Schütte-Engel *et al.*, JCAP **08**, 066 (2021), 2102.05366.

[149] S. Beurthey *et al.*, (2020), 2003.10894.

[150] I. G. Irastorza and J. Redondo, Prog. Part. Nucl. Phys. **102**, 89 (2018), 1801.08127.

[151] T. Dafni *et al.*, Nuclear and Particle Physics Proceedings **273-275**, 244 (2016).

[152] I. Shilon, A. Dudarev, H. Silva, and H. H. J. ten Kate, IEEE Transactions on Applied Superconductivity **23**, 4500604 (2013), 1212.4633.

[153] K. Ehret *et al.*, Physics Letters B **689**, 149 (2010).

[154] R. Bähre, Journal of Instrumentation **8**, T09001 (2013).

[155] A. Ayala, I. Domínguez, M. Giannotti, A. Mirizzi, and O. Straniero, Phys. Rev. Lett. **113**, 191302 (2014), 1406.6053.

[156] E. Masso and R. Toldra, Phys. Rev. D **52**, 1755 (1995), hep-ph/9503293.

[157] V. M. Mehta *et al.*, (2020), 2011.08693.

[158] W. H. Press and P. Schechter, Astrophys. J.**187**, 425 (1974).

[159] J. R. Bond, S. Cole, G. Efstathiou, and N. Kaiser, Astrophys. J.**379**, 440 (1991).

[160] S. Murray, C. Power, and A. Robotham, (2013), 1306.6721.

[161] R. K. Sheth, H. J. Mo, and G. Tormen, Monthly Notices of the Royal Astronomical Society **323**, 1 (2001), https://academic.oup.com/mnras/article-pdf/323/1/1/3204200/323-1-1.pdf.

[162] A. Eberhardt, A. Banerjee, M. Kopp, and T. Abel, Phys. Rev. D **101**, 043011 (2020), 2001.05791.

[163] M. Trenti and P. Hut, Scholarpedia **3**, 3930 (2008), revision #91544.

[164] J. Barnes and P. Hut, Nature (London)**324**, 446 (1986).

[165] V. Springel, R. Pakmor, O. Zier, and M. Reinecke, (2020), 2010.03567.

[166] V. Springel, S. D. M. White, G. Tormen, and G. Kauffmann, Monthly Notices of the Royal Astronomical Society **328**, 726 (2001), https://academic.oup.com/mnras/article-pdf/328/3/726/4068642/328-3-726.pdf.

[167] K. Dolag, S. Borgani, G. Murante, and V. Springel, Monthly Notices of the Royal Astronomical Society **399**, 497 (2009), https://academic.oup.com/mnras/article-pdf/399/2/497/3620682/mnras0399-0497.pdf.

[168] J. L. Bentley, Commun. ACM **18**, 509–517 (1975).

[169] J. F. Navarro, C. S. Frenk, and S. D. M. White, Astrophys. J. **462**, 563 (1996), astro-ph/9508025.

[170] J. F. Navarro, C. S. Frenk, and S. D. M. White, Astrophys. J. **490**, 493 (1997), astro-ph/9611107.

[171] J. F. Navarro, C. S. Frenk, and S. D. M. White, Monthly Notices of the Royal Astronomical Society **275**, 720 (1995), https://academic.oup.com/mnras/article-pdf/275/3/720/2805863/mnras275-0720.pdf.

[172] J. S. Bullock *et al.*, Mon. Not. Roy. Astron. Soc. **321**, 559 (2001), astro-ph/9908159.

[173] I. Gott, J. Richard, Astrophys. J.**201**, 296 (1975).

[174] E. Bertschinger, ApJS**58**, 39 (1985).

[175] K. M. Zurek, C. J. Hogan, and T. R. Quinn, Phys. Rev. D **75**, 043511 (2007), astro-ph/0607341.

[176] W. Hu, R. Barkana, and A. Gruzinov, Phys. Rev. Lett. **85**, 1158 (2000), astro-ph/0003365.

[177] H.-Y. Schive *et al.*, Phys. Rev. Lett. **113**, 261302 (2014), 1407.7762.

[178] J. C. Niemeyer, (2019), 1912.07064.

[179] A. A. Klypin, A. V. Kravtsov, O. Valenzuela, and F. Prada, Astrophys. J. **522**, 82 (1999), astro-ph/9901240.

[180] B. Moore *et al.*, Astrophys. J. Lett. **524**, L19 (1999), astro-ph/9907411.

[181] J. Dubinski and R. G. Carlberg, Astrophys. J. **378**, 496 (1991).

[182] B. Eggemeier and J. C. Niemeyer, (2019), 1906.01348.

[183] B. Eggemeier, In preparation.

[184] S. Dong *et al.*, Astrophys. J.**871**, 70 (2019), 1809.08243.

[185] K. Chang and S. Refsdal, Nature (London)**282**, 561 (1979).

[186] J. Schneider, The extrasolar planets encyclopaedia, `http://exoplanet.eu/catalog.php`.

[187] H. Niikura *et al.*, Nature Astron. **3**, 524 (2019), 1701.02151.

[188] S. Sugiyama, T. Kurita, and M. Takada, Mon. Not. Roy. Astron. Soc. **493**, 3632 (2020), 1905.06066.

[189] R. Narayan and M. Bartelmann, Lectures on gravitational lensing, in *13th Jerusalem Winter School in Theoretical Physics: Formation of Structure in the Universe*, 1996, astro-ph/9606001.

[190] K. Fujikura, M. P. Hertzberg, E. D. Schiappacasse, and M. Yamaguchi, (2021), 2109.04283.

[191] D. Croon, D. McKeen, N. Raj, and Z. Wang, Phys. Rev. D **102**, 083021 (2020), 2007.12697.

[192] D. Croon, D. McKeen, and N. Raj, Phys. Rev. D **101**, 083013 (2020), 2002.08962.